The University Of Sheffield.

Photoreceptor microsaccades in *Drosophila*: Three-dimensional characterisation

Joni Jaakko Tapani Kemppainen

A thesis submitted in partial fulfilment of the requirements for the degree of Doctor of Philosophy

The University of Sheffield
Faculty of Science
Department of Biomedical Science

September 2021

Acknowledgements

I am grateful for the motivation and support provided by my friends and relatives, colleagues and co-workers, during the last 4 years. For such a long journey, it is nearly impossible to credit all the people fairly but here we go!

First of all, I would like to thank my supervisor Professor Mikko Juusola, who supported and guided my research every day. His enthusiasm and passion for science and life in general keeps inspiring me still for a long time in the future. I would also like to thank my advisors Professor Marcello Rivolta and Dr. Andrew Lin, my best advisors, whose comments and support were invaluable for completing this project.

Thank you Professor Gregor Belušič and Dr. Anton Nikolaev for being by external and internal examiners, respectively. Your comments and criticism led to a substantial improvement of this thesis.

Many thanks to all the current and past Juusola research group members Ben, David, Diana, James, Jouni, Keivan, Narendra, Neveen and Zhuoyi for everyday peer-support and for being amazing friends. Equally, many thanks to the wonderful B-222 office members Alice, Anthi, Daniel, Emily, Hoger, Katie, and, Chun next door. Every Thursday 9:30am, we assembled for the joint Lin-Juusola meetings, to learn about vision, olfaction, genetics and neuroscience in general. Thanks to the project students (Andra, Callum, James, Tom) for your excellent work, motivation and software testing.

I also thank my second supervisor Professor James Marshall and the Brains on Board members, with whom I gained invaluable experience in scientific presentation during the biannual meetings. In addition, I acknowledge the University and the BMS administrative

and technical personnel for their continuous support. Special thanks to Chris for EM guidance and Matt and Bob for technical assistance. Also thanks to Neville for the extraordinary honeybee keeping.

I would like to thank all the ESRF and DESY beamline staff, administrative and technical personnel there for making the X-ray experiments possible. Equally many thanks to all our collaborators. Special thanks to Professor Becker for providing honeybees in Hamburg.

Furthermore, I was supported beyond the university walls. Many thanks to house mates Alex, Becky, Charlotte, Dimitar and Tom, who welcomed me to Sheffield. Cheers to the Sheffield Bears for university ice-hockey in their late night training. Equally, cheers to the Sheffield Greek School and its amazing teachers and the classmates I had there.

Greeting to friends made in Tübingen. Long time no see.

Greetings to my friends and relatives back in Finland, Oulu and elsewhere. From the small village of Hyrynsalmi, in the middle of the Kainuu region, it is easy to leap to the world, when you have the best parents (Pekka and Taina), grandparents (Jaakko, Kyllikki and Maija) and siblings (Aleksi and Iida) in the world.

Finally, thanks to my fiancée Anthi for sharing all these years with me.

Abstract

My thesis is about the fruit fly (*Drosophila melanogaster*) photoreceptor microsaccades. These are light-induced rapid micrometer-sized photoreceptor displacements caused by their photomechanically contracting microvilli. I used two imaging methods to investigate this phenomenon: synchrotron X-rays and the deep pseudopupil. I was motivated by our group's previous work, which showed that the microsaccades improve the *Drosophila* vision beyond the optical limits of a static eye. I desired to characterise the microsaccades in 3-dimensions.

First, our high-speed synchrotron X-ray experiments led to an unexpected discovery that the X-rays themselves activate phototransduction similar to visible light. The X-ray induced microsaccades were left-right mirror-symmetric and stronger where the two eyes' visual fields meet. In addition, the motion analysis along the receptor's side-profile suggested spatial specialisations. Second, I developed the first goniometric (angle-measuring) high-speed deep pseudopupil (GHS-DPP) system for mapping photoreceptor microsaccades across the left and right eyes. My results suggest that the microsaccades are tuned to the optic flow and are developmentally set by the R1-R8 rhabdomere orientations, which also follow the optic flow. Third, the localised GHS-DPP experiments using rhodopsin-specific rescues showed that all R1-R8 rhabdomeres contributed towards the microsaccades, irrespective how I immobilised the flies. Furthermore, light stimulation with sinusoidal and frequency sweeps showed that the microsaccades could follow temporal contrast changes up to 30 Hz (3 dB cut-off at 13 Hz), indicating that the microsaccades happen during light contrast changes in the natural environment.

Overall, my results suggest that the photoreceptor microsaccades improve vision,

accommodating the fly's behavioural needs. The insect eyes have evolved over hundreds of millions of years. My research helps to better understand some less obvious design choices, broadening our knowledge about how visual sensory systems work dynamically. The potential applications of this work range from man-made image sensors to stereo vision algorithms, autonomous drones, consumer electronics and improved medical implants, such as bionic eyes.

Contents

List of Abbreviations

BNC	Bayonet Neill–Concelman (a connector type)
Cq	Heterotrimeric G-protein
DAG	Diacylglycerol
DAQ	Data acquisition (system)
DESY	The Deutsches Elektronen-Synchrotron
DPP	Deep pseudopupil
DPP-MS	Deep pseudopupil microsaccades
ERG	Electroretinogram
ESRF	The European Synchrotron Radiation Facility
fps	Frames per second
GHS-DPP	Goniometric high-speed deep-pseudopupil (imaging system)
GWN	Gaussian white noise
ID16B	A beamline, ESRF
InsP3	Inositol 1,4,5 trisphosphate
IR	Infrared (light)
ISI	Inter stimulus interval

KB	Kirkpatrick-Baez (X-ray mirror arrangement)
LED	Light emitting diode
N	The number of animals tested
NA	Numerical aperture
P10	A beamline, DESY
PIP_2	Phosphatidyl-inositol 4,5 biphosphate
PLC	Phospholipase C
R1-R6	Outer receptors (or rhabdomeres)
R7-R8	Inner receptors (or rhabdomeres)
RF	Receptive field
ROI	Region of interest
TRP	Transient receptor potential (light-gated channel)
TRPL	Trpl-like (light-gated channel)
UV	Ultraviolet (light)
WT	Wild-type

List of Figures

1 General introduction

Active sensing systems probe their environment using self-generated energy, such as echolocation sounds created by marine mammals and bats (Schroeder et al., 2010). Vision, which samples incoming light quanta into neural signals, is traditionally considered passive but often fulfils the active sensing definition (probing with self-generated energy) and can be studied from the active viewpoint (Nelson & MacIver, 2006; Schroeder et al., 2010; Wachowiak, 2011).

In active vision, rhythmic scanning patterns, such as eye saccades and microsaccades in humans (Otero-Millan et al., 2008), reshape the light input that the visual sensory cells can perceive. The insect compounds eyes are part of the head's rigid exoskeleton and cannot move like ours. But the flies, for example, can translate and rotate their body with respect to their environment (body saccades: Geurten et al., 2014; Mongeau & Frye, 2017; Muijres et al., 2015), and turn their head (head saccades: Cellini & Mongeau, 2020; Cruz et al., 2021; A. J. Kim et al., 2017). In addition, the fly eyes have tiny muscles that can shift the retinal tissue, moving the photoreceptors' receptive fields relative to the outside world (Burtt & Patterson, 1970; Hengstenberg, 1972). Notably, all these mechanisms for active vision use muscles to move the receptors.

Using atomic force microscopy, Hardie and Franze (2012) found that the fruit fly (*Drosophila*) photoreceptors photomechanically contract *ex vivo* when exposed to light flashes. Soon after, high-speed optical imaging revealed that these contractions moved the photoreceptors *in vivo* with respect to the facet lenses, enhancing the flies' visual acuity (Juusola et al., 2017). These photoreceptor microsaccades allow the photoreceptors to adjust their receptive fields directly based on the light input they receive, without any eye muscle

activity.

In my thesis, I investigated the photoreceptor microsaccades in *Drosophila* using high-speed microscopy techniques with synchrotron X-rays and near-infrared visible light. My results are consistent with the earlier findings (Hardie & Franze, 2012; Juusola et al., 2017). However, for the first time, I characterise the microsaccades' 3-dimensional kinematics across the compound eyes. This work generated important new knowledge about the photoreceptor microsaccades, thus contributing to active vision research in compound eyes.

In this introduction, I first explain how the fruit fly compound eyes are structured and function. Then, I review the traditional view of how their spatial acuity is optically limited by their ommatidial tiling, suggesting coarse and pixelated vision. Finally, I examine the retinal micromovements that push the insect vision beyond the limits of sampling through static compound eye structures. Here, the focus is on the photoreceptor microsaccades.

1.1 The fly visual system

Flies have seven light-sensitive organs: two main compounds eye located on the sides of the head, three ocelli on the head's vertex in a triangle arrangement, and two Hofbauer-Buchner eyelets beneath the compound eyes' posterior margin (Helfrich-Förster et al., 2002). First, the eyelets function as a circadian photoreceptor (Rieger et al., 2003; Veleri et al., 2007). Based on their immunoreactivity, they possibly contain histamine and acetylcholine for synaptic transmission (Yasuyama & Meinertzhagen, 1999)

Second, the ocelli are three small lens-capped eyes on the head's vertex. In each ocellus, the 40 µm diameter lens lies above 90 likely histaminergic (Pollack & Hofbauer, 1991) photoreceptors. The photoreceptors synapse to interneurons projecting to the lateral protocerebrum thus bypassing the visual processing of the optic lobes (Hu et al., 1978).

Although the ocellar image is under-focused and blurred (Homann, 1924; Wehrhahn, 1984), the ocelli participate in visual orientation (Wehrhahn, 1984), ambient light level detection and phototaxis (Hu & Stark, 1980), circadian rhythm synchronisation (Rieger et al., 2003), and gaze and flight stabilisation (Krapp, 2009).

The main visual organs, however, are the two large red-tinted compound eyes that make up the most distinctive features of the fly's head (**Figure 1.1A**). Each *Drosophila* eye comprises 750-800 nearly identical lens-covered units called ommatidia (Montell, 2012) (**Figure 1.1B**, **C** and **D**). The angular difference between the adjacent ommatidia is know as the interommatidial angle and often denoted as $\Delta\phi$. In each ommatidium, eight rod-shaped photoreceptors, surrounded by the pigment and cone cells, point their light-sensing organelles called the rhabdomeres towards the ommatidial axis in a trapezoidal arrangement. Here, the outer R1-R6 rhabdomeres surround the inner R7-R8 rhabdomeres (Mishra & Knust, 2012). The R1-R6 receptors run along with the retina's full depth, whereas the R7-R8 receptors each occupy approximately a half of the retina's depth (Montell, 2012)

The rhabdomeres are made of densely packed microvilli, small plasma membrane protrusions 1.5 μm in length and 60 nm in width (Mishra & Knust, 2012). The microvilli have no internal organelles (Montell, 2012), allowing the outer R1-R6 rhabdomeres contain approximately 30 000 and the inner R7-R8 rhabdomeres 15 000 of them (Juusola et al., 2017). In the microvilli, a complex biochemical cascade called the phototransduction occurs (Hardie & Juusola, 2015).

The *Drosophila* has an open rhabdom eye, in which the rhabdomeres are separated from each other by the inter-rhabdomeric-space (Zelhof et al., 2006), making the R1-R6 receptors independent detectors (R7 shares its view with R8). Seven rhabdomeres from neighbouring ommatidia have optically arranged so that their receptive fields overlap. Six of them (R1-R6 from neighbouring ommatidia) project their axons to the same lamina cartridge, creating the so-called neural superposition (Agi et al., 2014; Langen et al., 2015). This evolutionarily recent (Osorio, 2007) neural superposition connectivity pattern offers high

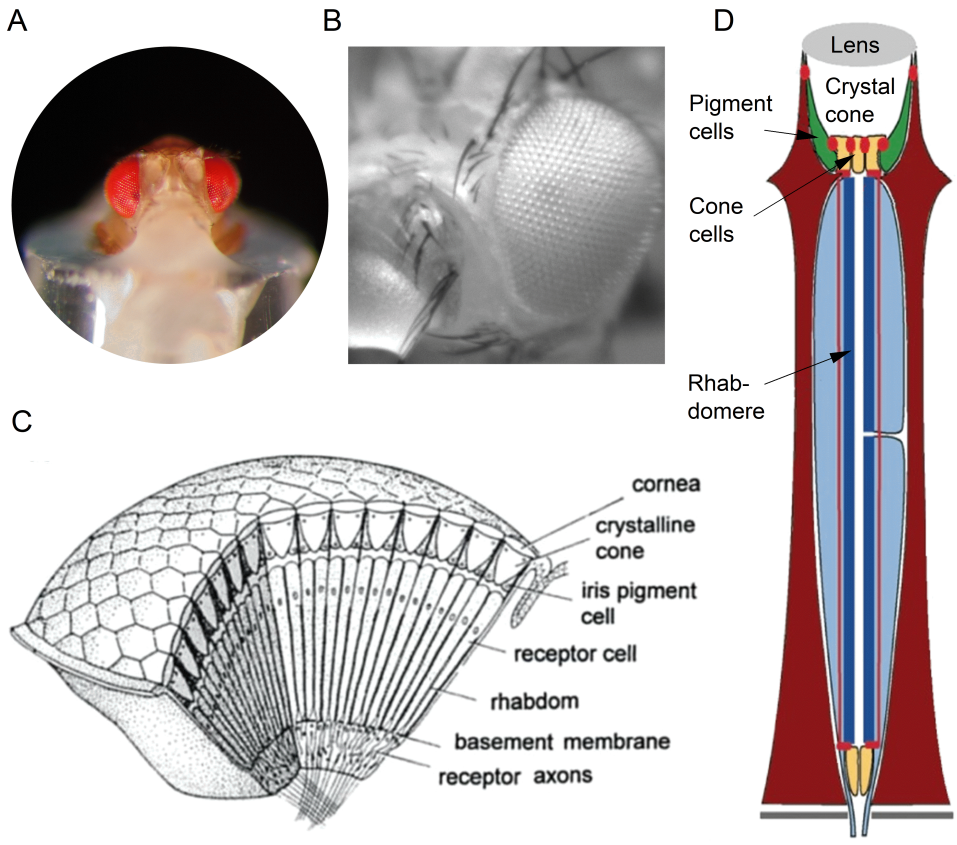

Figure 1.1: The fruit fly early visual system A) In the fruit fly, the left and right compound eyes (red-tinted) make up the most distinctive features of the fly's head. **B)** A grey-scale photo shows the hexagonally arranged facet lenses. **C)** The fly compound eye is tiled with repeated elongated units called ommatidia. **D)** The facet lens focuses light on the waveguide acting R1-R8 rhabdomeres that convert the light input into neural signals. The R1-R6 photoreceptor axons run from the retina through the basement membrane to the first visual ganglion, the lamina. The R7 and R8 bypass the lamina and synapse to the medulla. The C and D are from Juusola et al. (2017), D originally from Tepass and Harris (2007).

resolution combined with high sensitivity. This eye design contrasts with the apposition and the optic superposition eyes, which have *either* good resolution *or* sensitivity, respectively (Langen et al., 2015).

All the R1-R8 photoreceptors use histamine as their neurotransmitter (Buchner et al., 1993; Pollack & Hofbauer, 1991). In addition, 24 neurons in the adult brain likely use histamine based on their anti-histamine immunoreactivity (Pollack & Hofbauer, 1991). The vision circuitry is such that the photoreceptor-provided retinotopic image of the outside world is processed by the optic lobe neuropils (lamina medulla, lobula, lobula plate) and then transmitted to the central brain (as reviewed by Nériec & Desplan, 2016; Zhu, 2013). This circuitry, however, is not central to this study and thus not further reviewed here.

In many animals, the two eyes have overlapping receptive fields. This binocular vision has many benefits, and notably, it allows the animals to estimate depth using disparity cues created by the eyes' differing viewing angles (Read, 2021). So far, the only insect demonstrated to possess stereo vision is the mantis, whose striking behaviour can be controlled using prisms or 3D-glasses altering the disparity (Nityananda et al., 2018; Rossel, 1983). We showed that also *Drosophila* may see the world in stereo by cross-correlating phasic disparity signals created by the mirror-symmetric photoreceptor microsaccades in the contralateral eyes (Kemppainen, Scales, et al., 2021). This *dynamic* stereo vision algorithm encodes the spatial disparity in time, and therefore enables stereo vision in eyes where only few receptors (>=3) share overlapping receptive fields.

1.2 Phototransduction cascade

The phototransduction cascade is a chain of G protein-coupled biochemical reactions occurring in the microvillar rhabdomeres (**Figure 1.2**). In the phototransduction, visual light quanta (photons) are sampled (Song et al., 2016) and encoded into the photoreceptors'

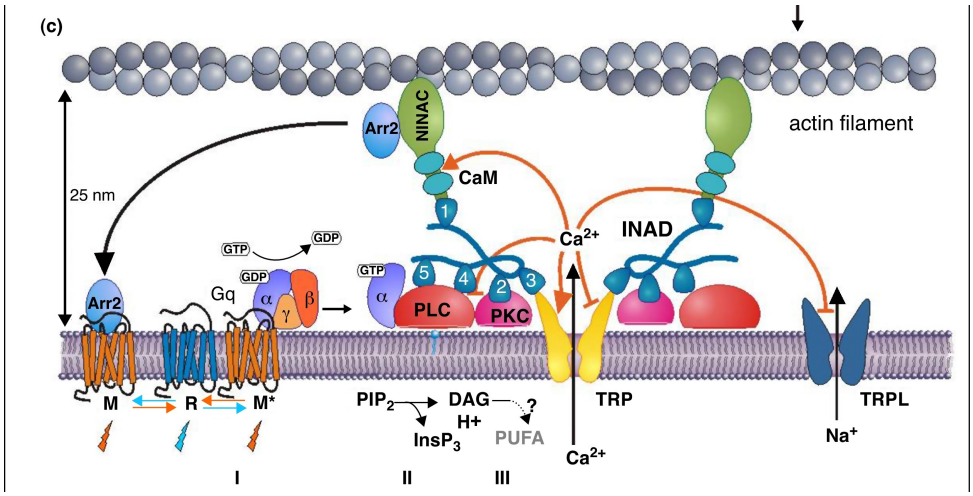

Figure 1.2: Phototransduction cascade. In the phototransduction cascade inside the microvilli, a photon activation converts rhodopsin into metarhodopsin, which activates the G-protein by GDP-GTP exchange. The Gqα subunit activates PLC that hydrolyses PIP_2. A yet unknown mechanism leads to the opening of TRP and TRPL channels and ion influx to the cell. From Hardie and Juusola (2015).

graded membrane potential responses.

The *Drosophila* phototransduction cascade starts when a photon is absorbed by the rhodopsin molecule, consisting of seven transmembrane opsin segments and a chromophore (Montell, 1999). All the outer R1-R6 receptors express rhodopsin-1 (Rh1). In contrast, the rhodopsin expression in the inner R7-R8 receptors is more complex: 30% of R7s express Rh3 and 70% Rh4, and 30% of R8s express Rh5 and 70% Rh6 (Montell, 2012). These ratios reflect the stochastic distribution of the pale (containing Rh3 and Rh5) and yellow (containing Rh4 and Rh6) ommatidia (Wernet et al., 2006). In addition to these compound eye rhodopsins, the ocelli express Rh2 (Montell, 2012), the circadian pacemaker cells within the brain express the light-sensitive cryptochrome protein (Emery et al., 1998; Rieger et al., 2003) and Rh7 (Ni et al., 2017), and the Hofbauer-Buchner eyelet express Rh6 (Senthilan et al., 2019; Yasuyama & Meinertzhagen, 1999)

Inside a single microvillus, a photon absorption causes the rhodopsin photoisomerisation

into metarhodopsin that then activates 5-10 heterotrimeric G-proteins (Cg) (Hardie & Juusola, 2015). The activated Cg protein releases its Gqα subunit activating the phospholipase C (PLC, encoded by *norpA* (Montell, 1999)). PLC hydrolyses phosphatidyl-inositol 4,5 biphosphate (PIP2) to create inositol 1,4,5 trisphosphate (InsP3), diacylglycerol (DAG) and a proton (Hardie & Juusola, 2015). How these hydrolysis end products then lead to opening of the "light gated" ion channels remains unresolved but is under active research (as recent examples, Delgado et al., 2019; J. Huang et al., 2010; Sokabe et al., 2021). Multiple models such as i) intracellular acidification, ii) activation by DAG or polyunsaturated fatty acids (PUFAs) that are formed from DAG and iii) InsP3 releasing Ca^{2+} from internal stores has been proposed (Hardie & Juusola, 2015; Montell, 2005). Intriguingly for this thesis, the photomechanical contraction of the microvilli (Hardie & Franze, 2012) may contribute in the channels' (mechanosensitive) activation (Hardie & Franze, 2012; Liu & Montell, 2015).

The opening of the "light-gated" transient receptor potential (TRP) and trp-like (TRPL) ion channels leads to Ca^{2+} and Na^{+} influx to the cell, respectively, creating a depolarising elementary response, a quantum bump (Hardie & Juusola, 2015). This elementary depolarisation contrasts the vertebrate phototransduction, where the light-induced reactions close the cGMP-gated channels and hyperpolarise the receptor cell (Montell, 1999). The increasing Ca^{2+} concentrations then quickly terminate the quantum bump by inhibiting the TRP and TRPL channels. As a result, the microvillus enters 100 ms refractory period, during which it cannot respond to photons (Hardie & Juusola, 2015; Juusola et al., 1994; Song & Juusola, 2014; Song et al., 2012). In addition, the Ca^{2+} influx through the TRP channels regulates the phototransduction for example by maintaining PIP_2 levels (Hardie & Juusola, 2015; Hardie et al., 2001).

After the photosensitive membrane creates a light-induced current (LIC), the photoreceptor's basal membrane reshapes, but does not limit (Juusola & Hardie, 2001) the voltage responses. This reshaping by voltage-gated K^{+} ion channels (Niven et al., 2003; Song et al., 2009) can be modelled by Hodgkin-Huxley dynamics. In addition, the synaptic feedbacks from the lamina further shape the receptors' output (Abou Tayoun et al., 2011;

Dau et al., 2016; Li et al., 2019; Nikolaev et al., 2009; Wardill et al., 2012; Zheng et al., 2006). Finally, the voltage signal propagates along the photoreceptor's axon, affecting the synaptic release of histamine from the photoreceptor in the lamina (R1-R6) and medulla (R7-R8).

1.3 The static compound eye acuity

In this thesis, spatial acuity or spatial resolution means the smallest grating that that eyes can resolve and distinguish from a similar flat-coloured object. This use of gratings to define resolvability emerges from Fourier's theorem stating that any 2-dimensional image is composed of countless simple gratings when their amplitudes and spatial wavelengths are carefully selected (Spencer, 1982, pg. 25). In the 1-dimensional case, Fourier's theorem becomes

$$f(x) = \sum_{m=0}^{m=\inf} (b_m \cos(mx) + a_m \sin mx) \tag{1.1}$$

It states that any function $f(x)$ can be expressed with an infinite series of sinusoidal functions (1-dimensional simple "gratings"). Therefore, to test the smallest resolvable features and quantify the limits of compound eyes' visual acuity, simple grating patterns have been used to find the smallest grating wavelengths that still yield behavioural or physiological responses (Catton, 1999; Horridge, 2003; Srinivasan & Lehrer, 1988).

In static compound eyes with stationary receptors, the interommatidial angle limits the resolvability, making a relatively low amount of ommatidia to view a vast visual space (Land, 1997). With its only 750-800 ommatidia (Montell, 2012), this pixelisation effect is especially profound in *Drosophila*. Its vision is considered to be replicable using a 26x26-pixel camera sensor with a fisheye lens or having as much visual acuity as a 14 diopters myopic person without glasses (Borst, 2009). The upper limit for spatial acuity can be considered in a

scenario where one ommatidium points to a grating's stripe and the adjacent ommatidium points the the grating's next stripe (Juusola et al., 2017). Then, it follows that

$$\nu_s = \frac{1}{2(\frac{\sqrt{3}}{2}\Delta\phi)} = \frac{1}{\sqrt{3}(\Delta\phi)} \tag{1.2}$$

Here, the ν_s is the maximum spatial frequency that the static compound eye can resolve and $\Delta\phi$ is the interommatidial angle. The factor $\frac{\sqrt{3}}{2}$ follows from the eye's hexagonal layout that decreases the effective interommatidial angle thus improving vision. In *Drosophila*, the interommatidial angle that varies from 4.5° to 5.5° (Currea et al., 2018), meaning that the *Drosophila* should not resolve higher spatial frequencies than 0.13 $(°)^{-1}$ or 0.10 $(°)^{-1}$, respectively.

1.4 Retinal micromovements

The visual acuity in stationary compound eyes is restricted by the interommatidial angle, making the *Drosophila*'s vision coarse compared to ours. However, the flies have 10 to 100 times better temporal resolution than the mammalian rods because of faster phototransduction (Hardie & Raghu, 2001), with information transfer rates peaking around 100 Hz for bursty light stimuli (Juusola et al., 2017). Furthermore, the emerging evidence indicates that the flies leverage their temporal resolution by creating retinal micromovements to improve their spatial resolution.

In human-made sensor systems, moving the image sensor to improve the image resolution beyond the sensor's pixel count set limits is known as microscanning (Fortin & Chevrette, 1996; Friedenberg, 1997; H. S. Kim et al., 2002). As an extreme example, early infrared scanning (thermography) used rotating or vibrating mirrors to create high-resolution images using a single point-wise detector (Leftwich, 1976),

In flies, the first discovered retinal micromovements were caused by the eye's orbito-tenorialis (MOT) muscles (Hengstenberg, 1972). The eye muscles pull the whole retina repeatedly with a rate modulated by changing light illumination, large striped patterns moving across the visual field or air-currents directed on the head (Burtt & Patterson, 1970). These retinal micromovements have led to bio-inspired visual scanning sensors that often use piezo actuators to achieve *hyperacuity* (as summarised by Viollet, 2014).

Recently, Juusola et al. (2017) discovered that the photomechanical photoreceptor contractions (Hardie & Franze, 2012) cause the receptors' micrometre-sized displacements *in vivo* with respect to the facet lenses. Together with the finding that the photoreceptors' refractory photon sampling (Song et al., 2016) is tuned to encode saccadic and bursty stimuli, the authors used biophysical modelling to explain how behaving flies and their receptors could resolve smaller than expected features (based on their interommatidial or acceptance angle, respectively). The fly vision was *hyperacute* (able to see better than what is predicted from the (static) optics alone).

The muscle-induced (Burtt & Patterson, 1970; Hengstenberg, 1972) and the photomechanical (Hardie & Franze, 2012; Juusola et al., 2017) retina micromovements are conceptually similar, both resembling microscanning in the man-made sensors. However, they have important differences. First, the photoreceptor microsaccades directly follow the light stimulus (Juusola et al., 2017), whereas the eye muscle saccades are periodic with light-dependent rate modulation (Burtt & Patterson, 1970). Second, the photoreceptor microsaccades are localised to the contracting receptors' vicinity (Kemppainen, Scales, et al., 2021). In contrast, the anchored muscles (Burtt & Patterson, 1970) likely pull and deform the retinal tissue as a whole. Finally, because the photoreceptor microsaccades are likely caused by PIP_2 cleavage in phototransduction (Hardie & Franze, 2012), they can react near-instantaneously to changes in light input. In contrast, the eye muscle's modulation is probably more delayed because of synaptic transmission and membrane potential propagation speeds. For these reasons, the eye muscles and the photoreceptor contractions could serve different purposes in the compound eyes.

There is no holistic view on how these retinal micromovements interplay with each other or with the head and body saccades. Notably, retinal movements of any source displace the receptors' receptive fields with respect to the environment, with self-generated energy, thus enabling active vision.

1.5 Photoreceptor microsaccades' components

The photoreceptor microsaccades have two components based on the rhabdomeres' movement direction with respect to the lenses: the lateral (sideways) and the axial (Juusola et al., 2017). Here, I examine what is known about these components.

The sideways component enhances the resolvability of moving features, giving the receptors more encoding time when their receptive fields move with the features (Juusola et al., 2017). The cornea neutralisation technique recordings (Juusola et al., 2017) show that the photomechanical contractions move the rhabdomeres up to 1.7 μm sideways, concerning the facet lenses, and importantly, back-to-front. Based on this direction (back-to-front), it was hypothesised that the photoreceptor microsaccades are aligned to the optic flow that a fly experiences during its forward locomotion (Juusola et al., 2017). However, the microsaccades directions across the eyes remain unmeasured.

The other important component of the microsaccades is the axial 0.5 μm movement towards and away from the facet lens (Juusola et al., 2017). Narrowing and widening the receptive fields, it likely contributes to the photoreceptors' ability to resolve hyperacute 2-dot stimulus together with the lateral contraction component (Juusola et al., 2017). The atomic force microscopy recordings on the excised retinae (Hardie & Franze, 2012) possibly captured some axial components. However, because the cornea neutralisation technique views the rhabdomeres head-on, the axial component remains unrecorded *in vivo*.

1.6 Aims and objectives

My thesis focuses on the photomechanical photoreceptor microsaccades, especially on their directions and kinematics using the fruit fly *Drosophila* as a model organism.

My aim is to characterise the unknown factors regarding the photoreceptor microsaccades: Their 3-dimensional kinematics across the left and right eyes, their emergence from the contracting R1-R8 rhabdomeres, their dependence on the immobilisation technique and their frequency-response characteristics.

To meet my aims, I formulated the following objectives

1. Measure microsaccades
   (a) along with the receptor side profile
   (b) across the left and right eyes
2. Test if the microsaccade directions follow any pattern related to
   (a) fly's behavioural needs
   (b) developmentally set structures
3. Investigate how the individual R1-R8 rhabdomeres contribute towards the microsaccades by using rhodopsin-specific blind rescue flies
4. Examine how the immobilisation technique affect the microsaccades
5. Measure frequency response function to sinusoidal sweep stimulus

1.7 Outline of the thesis

To fulfil my objectives, I used two new imaging methods: synchrotron X-rays and the deep pseudopupil (DPP). The results have been divided into three main chapters based on the experimental technique used.

In chapter 2, I analysed the high-speed synchrotron X-ray imaging data that we obtained at the ESRF and DESY beamlines. Unexpectedly, X-rays alone activated the photoreceptors causing photomechanical photoreceptor contractions that were left-right mirror-symmetric and back-to-front directed. In addition, the motion analysis along the receptor side profile suggests three spatial specialisations in the microsaccades.

In chapter 3, I developed and built a goniometric high-speed deep pseudopupil (GHS-DPP) imaging system to record photoreceptor microsaccades across the left and right eyes. The data from these global recordings suggest that the microsaccade directions are tuned to the optic flow and developmentally set by the rhabdomere orientations, which also seem to follow the optic flow.

In chapter 4, I used the local GHS-DPP experiments to test three hypotheses regarding the photoreceptor microsaccades. First, all the tested R1-R8 receptor combinations contributed towards the microsaccades, moving the rhabdomeres inside an ommatidium as a unit. Second, the pipette tip immobilisation technique was found not to affect the microsaccades. Third, sinusoidal sweep stimuli and their variations showed that the microsaccades follow temporal contrast changes up to 30 Hz (3 dB cut-off at 13 Hz), strongly indicating that the microsaccades are relevant to fly vision outside the laboratory settings.

Most of the content presented in this thesis has been included in two pre-printed paper manuscripts currently under consideration in PNAS (Kemppainen, Scales, et al., 2021) and Communications Biology (Kemppainen, Mansour, et al., 2021). In addition, free and open-source (GPLv3) software tools to record (Kemppainen, 2020b) and analyse (Kemppainen,

2020a) the photoreceptor microsaccades have been made openly available.

2 X-ray imaging photoreceptor microsaccades

2.1 Introduction

The photoreceptor microsaccades have been recorded using the cornea neutralisation technique (Juusola et al., 2017) that shows the receptors' micrometre-sized sideways movement with respect to the facet lenses. R1-R8 photoreceptors of dissociated contract 0.5 μm axially and 1.7 μm sideways (laterally). Both the axial and lateral contraction components are likely to contribute to the photoreceptors' ability to resolve hyperacute 2-dot stimulus (Juusola et al., 2017). The atomic force microscopy on the excised retinae (Hardie & Franze, 2012) possibly captured some of the axial component. Still, it has not been directly imaged in living flies as the cornea neutralisation technique views the rhabdomeres head-on. A new approach allowing to view the rhabdomeres along their side profile is, therefore, needed.

Following their discovery in 1895, X-rays have been used in various imaging applications such as shoe-fitting fluoroscopes (Duffin & Hayter, 2000). Nowadays, the best X-rays are produced at large scale facilities called synchrotrons, where *brilliance* measures the X-rays' quality by describing the smallest volume that the X-rays can be focused in (Willmott, 2019, pg. 50). High brilliance often implies high coherence that allows the phase-contrast imaging technique, where constructive and destructive interactions with phase-shifted X-rays at the image plane create the image contrast, superior for soft tissue samples (Lengeler, 2001). In addition, the use of high-energy synchrotron X-rays has pushed X-ray imaging to the nanoscale (Baruchel et al., 2008), which was previously only achievable to techniques such as electron microscopy. Compared to electron microscopy, however, X-ray phase-contrast

imaging does not require tedious sample slicing or additional staining, making it possible to image live specimens. In the case of insects, synchrotron X-ray phase-contrast imaging has been used to study dynamic processes, for example, insect respiration (Socha et al., 2010), the kinematics of cockroach's mouth-parts (Betz et al., 2008), and the blowfly's flight motor system (Mokso et al., 2015). These studies indicate that the technique could be suitable for imaging photoreceptor microsaccades as well.

We were granted beamtime in the DESY and ESRF synchrotrons to image photoreceptors microsaccades in fruit fly (*Drosophila*) eyes. The flies were placed on the synchrotron beamline and X-ray phase-contrast imaged for 300 ms with a high-speed camera running 100 fps, revealing for the first time how the photoreceptor microsaccades occur inside the eye in 2D radiographic projections. Unexpectedly, however, we discovered that the X-rays alone activated the photoreceptors, leading photoreceptor contractions with kinematics (sigmoidal) and directions (back-to-front) consistent with the literature (Hardie & Franze, 2012; Juusola et al., 2017). In addition, these X-ray induced microsaccades were mirror-symmetric between the left and the right eyes, suggesting binocular interactions for the contralateral forward-facing receptive fields (RFs). The speed and displacement analysis suggest that the microsaccades' movement profiles may be specialised for the fly's behavioural needs.

2.2 Methods

2.2.1 Flies and preparation

In this study, wild-type (Berlin) flies and three blind mutant flies: hdc^{JK910} , $norpA^{P24}$ and *trp/trpl* were tested. The hdc^{JK910} flies have unfunctional histidine decarboxylase molecules preventing the neurotransmitter histamine synthesis in photoreceptors. Thus,

Table 2.1: Fly food formula (Drosophila Facility, Sheffield)

Ingredient	**Amount**	**Manufacturer**	**Supplier**
Cold tap water	1 l		
Medium cornmeal	80 g	Triple Lion	Lembas / Easton Enterprises
Dried yeast	18 g	Kerry Ingredients	BTP Drewitt
Soya flour	10 g	Lembas Wholefoods	Lembas
Malt extract	80 g	Rayner's Essentials	Lembas
Molasses	40 g	Rayner's Essentials	Lembas
Agar	8 g		BTP Drewitt
10% nipagin in absolute ethanol	25 ml	Clariant UK Ltd; Fisher	Chemolink Specialities Ltd; Fisher
Propionic acid	4 ml	Fisher	Fisher

the photoreceptors have functional phototransduction cascades but transfer no information downstream, rendering them blind. The $norpA^{P24}$ flies have a null mutation of the phospholipase C protein (PLC), required in the phototransduction cascade to hydrolyse the phosphatidyl-inositol 4,5 biphosphate (PIP_2) (Hardie & Franze, 2012), making the photoreceptors incapable of light-activation and the flies blind. Importantly, the subsequent lack of PIP_2 cleavage prevents the photoreceptor contractions. Finally, the *trp/trpl* null-mutant flies lack the "light-gated" transient receptor potential (trp) and trp-like (trpl) ion channels required in generating the light-induced electrical responses, making the flies blind. However, their receptors can contract because the PIP_2 cleaving by PLC remains unaffected.

The flies were raised at 25°C under 12:12h light-dark cycle and fed with standard fly food (**Table 2.1**). They were then taken from our Sheffield fly-stock to the synchrotron beamlines in Grenoble, France (ESRF), and Hamburg, Germany (DESY), where they were kept in ambient light conditions and room temperature until prepared as described below.

A healthy *Drosophila* was inserted into a plastic pipette tip (1000 µl) by puffing air with a 500 ml syringe and keeping the head and a part of the upper thorax above the tip line. Next, the fly head was immobilised into the pipette tip from the dorsal thorax and ventral mouth parts using melted beeswax. In some preparations, the antennae were fixed with beeswax to minimise muscle activity and avoid the antennae shadowing the eye in the X-ray images. Once the fly was adequately immobilised, the pipette tip was super-glued on a brass metal pin, which was then inserted on the rotation stage system of the beamline.

2.2.2 Synchrotron X-ray imaging

The synchrotron X-ray microscopy was performed at two third-generation synchrotron sources: At the European Synchrotron Radiation Facility (ESRF), beamline ID16B, and the Deutsches Elektronen-Synchrotron (DESY), beamline P10.

In these facilities, accelerated electrons were kept circulating in the magnetic field of the large storage ring; 844 m circumference for ESRF and 2300 m for DESY. The electron beam, exiting the storage ring, travelled through undulators that made the electrons oscillate and subsequently release their kinetic energy as X-ray radiation. This X-ray beam was further monochromatised so that all the X-ray photons had the same energy. On the ID16B beamline X-ray photon energy was set to 17.5 keV and at the P10 beamline to 10.0 keV or 13.8 keV. Photon's energy E is directly proportional to its frequency ν and frequency ν, in general, is inversely proportional to wavelength λ, leading to the relation

$$\lambda = \frac{c}{\nu} = \frac{hc}{E} \tag{2.1}$$

where c is the propagation speed ($3 \times 10^8\,\mathrm{m\,s^{-1}}$ in vacuum) and h is the Planck constant ($4.14 \times 10^{-15}\,\mathrm{eVHz^{-1}}$). Therefore, the corresponding ID16B X-ray photon wavelength was 0.071 nm and 0.12 nm and 0.090 nm for P10's lower and higher energy settings, respectively.

Notably, these wavelengths are more than a thousand times smaller than visible light wavelengths ranging from 380 nm to 700 nm.

The monochromatic X-ray beam was next focused into a tiny focal spot (≤ 100 nm) using two mirrors in Kirkpatrick-Baez (KB) arrangement: One of the KB mirrors was set to be vertical and the another horizontal. The prepared fly was inserted in the designated holder on the rotation stage system, and placed slightly downstream from the focused X-ray spot. The camera was placed few meters downstream from the focal spot. This arrangement allowed the geometrical magnification M as

$$M = \frac{z_s + z_d}{z_s} \tag{2.2}$$

where z_s is sample's distance from the focal plane and z_d is the detector's distance from the sample (Mokso et al., 2007). The magnification was adjusted by changing the sample's distance z_s to make either one of the eyes or the whole head fully visible in the X-ray images. The automated rotation stage system allowed to remotely control the fly's rotation and position with respect to the X-ray beam and the detector to select the best viewing angles.

During the experiments, the X-rays onset and offset was controlled by the fast shutter located upstream from the sample. Usually, the X-rays were set on for 200 ms or 300 ms while simultaneously X-ray images were acquired with the optical camera running at 100 Hz (BNC hardware triggering). A scintillator in the front of the camera transformed the X-rays into visible light photons, and the effective pixel size was 70 nm at ID16B and 167 nm at P10, respectively.

Finally, upstream from the sample, various silica and aluminium attenuators were combined to control the X-ray beam intensity. This arrangement enabled us to record photoreceptor contraction responses over varying X-ray intensity and control the fly's radiation dose.

2.2.3 Simultaneous ERG-recordings

To test whether the X-rays activate photoreceptors, we adapted the electroretinogram (ERG) recording method for the synchrotron beamline. This method uses extracellular glass microelectrodes to measure the photoreceptors' and visual interneurons' global electrical responses to the X-ray pulses. The ERG responses presented in this thesis were recorded at the DESY P10 beamline.

A custom ERG-frame was assembled from T-slotted aluminium profiles (MakerBeam, MakerBeam B.V., Netherlands) having adjustable copper coated fabric curtains (Nickel/Copper Polyester Nonwoven PET Fabric, Saint-Gobain Performance Plastics, France/USA). The ERG-frame was the mount point for two micromanipulators (uMp, Sensapex, Finland) and the ERG amplifier headstage (EXT-02, NPI Electronics, Germany). Together with the curtains, it further created a Faraday cage, ideally eliminating any electrical interference originating from the environment.

The recording and reference electrodes were fabricated the same way. We used a laser micropipette puller (P-2000, Shutter Instrument, USA) to create blunt, low-resistance electrodes from borosilicate glass capillaries (inner and outer diameters of 0.5 mm and 1.0 mm). At the synchrotron, these electrodes were backfilled by a ringer solution, using a thin plastic needle and a laboratory syringe. The ringer solution contained 120 mM NaCl, 5 mM KCl, 10 mM TES ($C_6H_{15}NO_6S$), 1.5 mM $CaCl_2$, 4 mM $MgCl_2$ and 30 mM sucrose (Juusola et al., 2016). They were then attached to polycarbonate electrode holders with chlorinated silver wire, allowing artefact-free bidirectional current flow between the metal circuitry and the ringer solutions (Sherman-Gold, 1993). Before securing the holders to the amplifier's headstage, the electrodes sharp tip was gently broken with a piece of paper to improve the electrical connection and prevent piercing the fly.

During the X-ray ERG experiments, the fly's position was first adjusted to make the recorded eye visible in the X-ray images. Then, the ERG electrodes were brought to contact with the fly

using the motorised micromanipulators. The recording electrode was touching the eye and the reference electrode the shoulder. First, ERG responses with expected waveforms were confirmed to a bright LED test flash. Then, ERG responses were recorded to 300 ms X-ray flashes over a range of X-ray intensities. Finally, after the X-ray experiments, we recorded an ERG response to the visible LED test flash as a control to confirm that the fly was still alive.

2.2.4 Data analysis

First, the raw X-ray images were preprocessed using a custom script that cropped out any unused sensor area and excluded those images where the fast shutter was closed. Next, the images were flat-field corrected by dividing each image by the corresponding flat image, an image taken without the fly (**Figure 2.1A**). This correspondence was based on the specimen and on the used X-ray attenuator settings. The flat-field correction removed most non-sample features, such as scintillator dust, from the final images. Importantly, each flat image averaged 20 to 200 subsequent X-ray frames, making the non-sample feature estimates more precise despite the photon shot noise and small image fluctuations. Finally, to improve image quality with higher attenuators, all flat-field corrected images were Gaussian blurred using spatial and temporal kernels of 4 pixels, respectively.

In these preprocessed images, the global photoreceptor activation was seen as faintly twisting rhabdomeres against a stationary background, comprised of lenses, trachea tubes and air sacs. To improve the rhabdomere motion detection, I tested further preprocessing steps of band-pass filtering for the DESY data set. Here, the images were transformed to Fourier space where the spatial wavelengths outside the range 0.03 to 0.1 were set to zero, resulting in images with a seemingly random mesh of strong-featured edges that visually moved in the same way as the rhabdomeres in the unfiltered X-ray images (**Figure 2.1B**). These filtered images seemed like a better target for the motion analysis. However, this came with the expense of somewhat reduced spatial specificity and required a scaling factor due

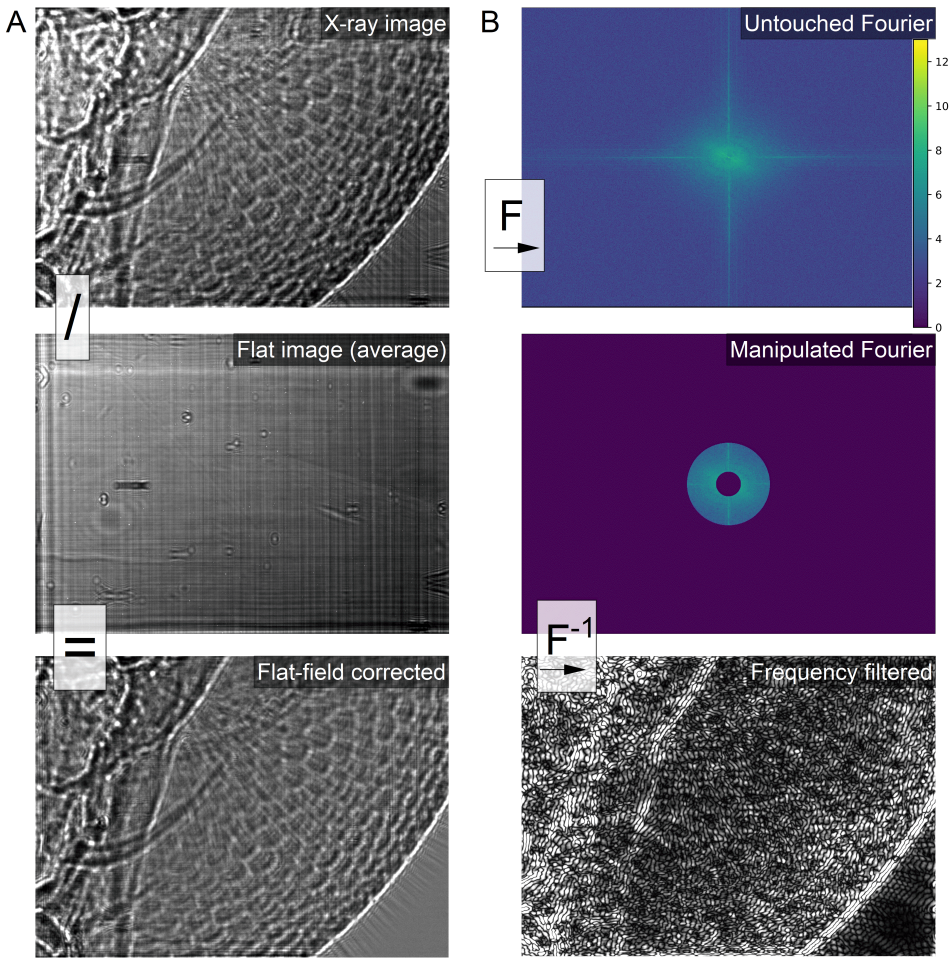

Figure 2.1: X-ray image preprocessing. **A)** The flat-field correction was performed as a pixel-wise division between the X-ray images (top) and the corresponding flat images (middle). This procedure removed most of the image artefacts from the final images (bottom). **B)** In the band-pass filtering, the flat-field corrected images were transformed to Fourier space (top), where normalised frequencies outside the range 0.03 to 0.1 were set to zero (middle). This procedure resulted in a mesh of randomly oriented edges whose motion corresponded to faintly visible rhabdomere motions in the unfiltered images.

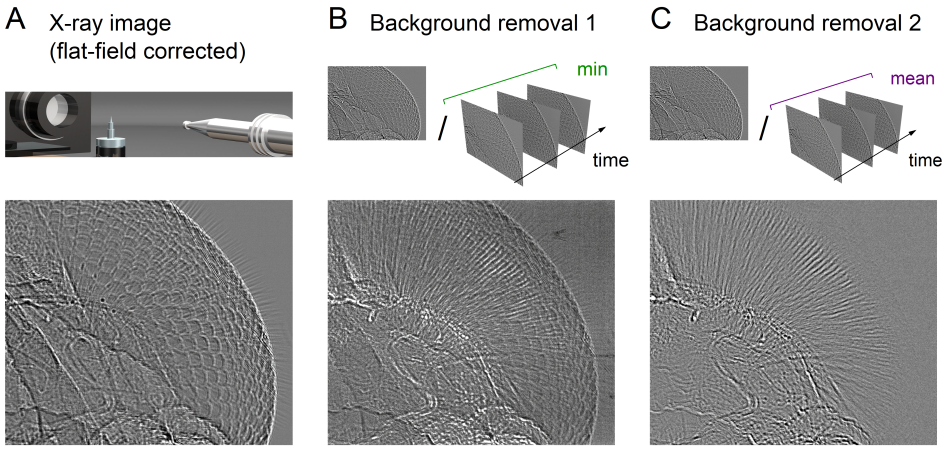

Figure 2.2: Background removal techniques. **A)** Flat-field corrected fly eye X-ray image from the ID16B beamline. **B)** In partial background subtraction, the X-ray images are divided by the recording's pixel-wise *minimum* frame, highlighting the moving features. **C)** In full background subtraction, the X-ray images are divided by the recording's pixel-wise *mean* frame, fully removing the stationary image features.

to the created stationary edges that were parallel to the motion.

As an alternative to frequency filtering, the ESRF X-ray images (**Figure 2.2A**) were further enhanced by a background removal technique. All frames were divided either by (i) the pixel-wise minimum-value frame over the corresponding X-ray flash imaging data to partially remove the stationary background (**Figure 2.2B**) or (ii) the pixel-wise mean-value frame to full removal (**Figure 2.2C**). Overall, the minimum frame subtraction gave better motion analysis estimates and was preferred; despite the mean-value division resulting in less noisy images. However, the background subtraction methods performed poorly when the images contained no moving features to begin with (for example, $norpA^{P24}$ and dead wild-type flies). In these cases, no background subtraction was used.

Once the X-ray images were preprocessed, the rhabdomeric motion was quantified using a custom computer script to perform template matching provided by the open-source computer vision library *OpenCV* (Bradski & Kaehler, 2000). The script uses the

`cv2.matchTemplate` function to calculate the following normalised cross-correlation R between source and template images

$$R(x,y) = \frac{\sum_{x',y'}(T'(x',y')) \cdot I'(x+x',y+y'))}{\sqrt{(\sum_{x',y'}(T'(x',y'))^2 \cdot \sum_{x',y'} I'(x+x',y+y')^2)}} \tag{2.3}$$

$$T'(x',y') = T(x',y') - 1/(w \cdot h) \cdot \sum_{x'',y''} T(x'',y'') \tag{2.4}$$

$$I'(x+x',y+y') = I(x+x',y+y') - 1/(w \cdot h) \cdot \sum_{x'',y''} T(x+x'',y+y'') \tag{2.5}$$

Here, R is the 2-dimensional cross-correlation result image and $R(x,y)$ are its pixel-wise values at some x, y coordinates. x', x" and y', y" are summation indices, limited by the cross-correlation window width w and height h within the ranges $[0,1,2\ldots,w-1]$ and $[0,1,2,...,h-1]$. T is the template image, and I is the source image. In the analysis, a frame k is used as the source image and the subsequent frame $k+1$ cropped by the cross-correlation window is used as a template image. Here, k denotes the image frame index from 0 to $N-1$, where N is the count of frames acquired during an X-ray flash. The $R(x,y)$ pixel values measure how well the template image matches the source image at any (x, y) location. Therefore, the inter-frame displacement can be calculated by taking the R's maximum (x, y) location for each frame pair using the *argmax* operation and taking the cumulative sum of the resulting array. The inter-frame displacement was limited to 10 pixels in maximum to avoid false matches with unphysical frame-to-frame displacements.

The cross-correlation window width w and height h were both set to 32 pixels. The user selected a region of interest (ROI) that was then filled with cross-correlation windows every 32 pixels in x and y. The ROIs were set where rhabdomeric motion was visually apparent and non-rhabdomeric movement sources, such as the antennae or the tracheal tubes, were

avoided. If the rhabdomeric motion was absent, as it was for some of the blind mutants, ROIs similar to the wild type flies were used.

The motion analysis results reported in this thesis are the geometric average calculated from all the windows within an ROI, and therefore the ROI's average motion. The movements are reported as directionless mean square root displacements that calculated from the respective x and y components using the Pythagorean theorem:

$$D = \sqrt{(X^2 + Y^2)} \tag{2.6}$$

Here, D, X, and Y are arrays holding the displacement values, each having a length of $N-1$, where N is the number of frames captured during an X-ray flash. The D movement traces were transformed from the camera pixel units into micrometres, using the pixel size unique for each detector and beamline configuration.

2.3 Results

2.3.1 Phase-contrast imaging reaches good image contrast in staining-free eyes

We performed high-speed synchrotron X-ray phase-contrast imaging at the ESRF ID16B and DESY P10 beamlines to investigate photoreceptor contractions inside the compound eye. First, however, we tested if unfixed and staining-free fruit fly compound eyes lead to sufficient image contrast.

The wild-type fly preparation was attached in the beamline facing towards the X-ray beam (**Figure 2.3A**). Once the beamline optics were configured and calibrated, the eyes appeared

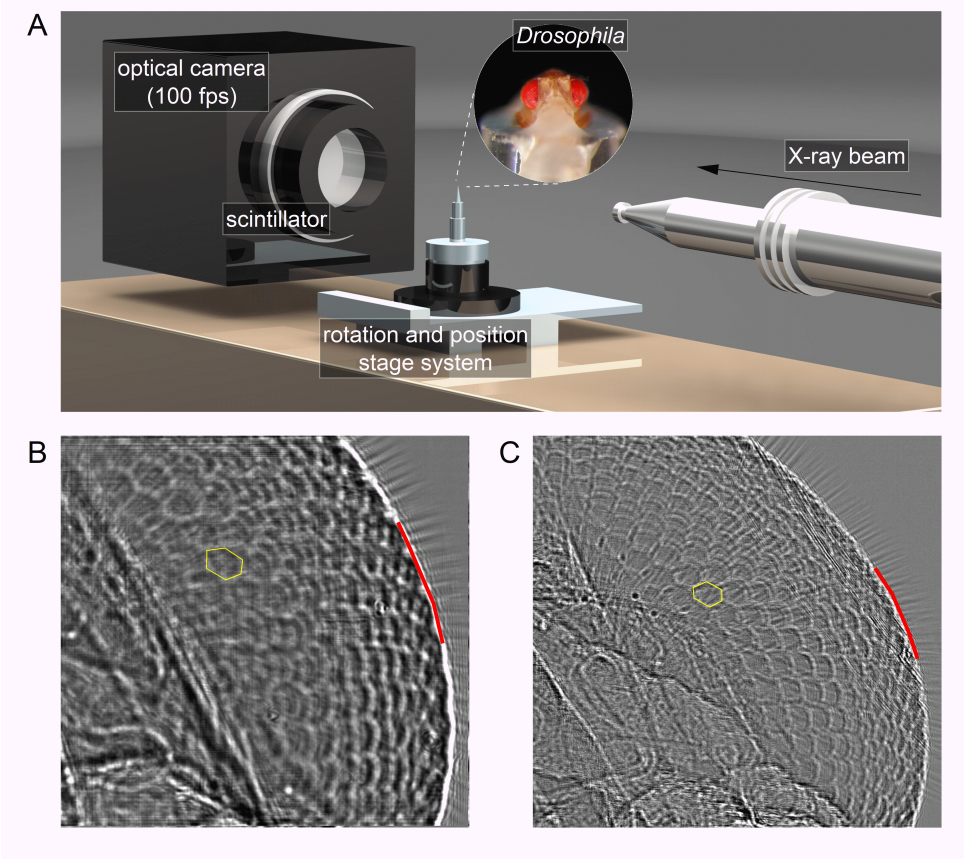

Figure 2.3: Synchrotron X-ray imaging produces good contrast in staining-free compound eyes. A) In phase-contrast imaging, coherent X-rays propagated through the eye and showing refractive index dependent phase-shifts. At the image plane, the X-ray waves interfered, creating a geometrically magnified shadow image of the sample. The scintillator converted the X-rays to visible light that the high-speed camera captured. **B)** X-ray phase-contrast image from the DESY P10 beamline. The facet lenses (yellow) and the eye-air border (red) are clearly visible. **C)** X-ray phase-contrast image from the ESRF ID16B beamline.

in the X-ray images well contrasted (**Figure 2.3B** and **C**) showing the eye-air interface, facet lenses and hair, and some internal head structures such as air sacs. In addition, the spatial image resolution was sufficient to resolve sub-micrometre sized features such as rhabdomeres if they were to move. However, because the images were a shadow created by all the tissue on the X-ray beam's way, it was hard to perceive how the image features were located in depth. Similarly, it was impossible to conclude from the still images alone if the radial lines on the eye (**Figure 2.3C**) were rhabdomeres or hairs.

These still-image experiments show that the synchrotron X-ray phase contrast imaging gives a good image contrast in living fruit fly eyes even without additional staining. Likewise, the image resolution is sufficient to detect features as thin as rhabdomeres.

2.3.2 X-rays induce photoreceptor microsaccades

Although rhabdomeres were not unambiguously visible in the still X-ray images, we reasoned that their movement would make them apparent. Therefore, a bright white LED was positioned above the fly and turned on simultaneously to the fast X-ray shutter (**Figure 2.4A**). Unexpectedly, however, we discovered that turning the X-ray radiation on (and off) itself makes the rhabdomeres displace from back to front (**Figure 2.4B** and **C**) repeatedly in most of the tested flies. Thus, the white LED was not only unnecessary, but its effects on the rhabdomere motion were undetectable, indicating that the X-ray induced movements masked it.

Cross-correlation motion analysis showed that the rhabdomeric motion's speed peaked at 60 ms to over 10 µm/s (**Figure 2.4D**), resulting in sigmoidal displacement[1] kinematics (**Figure 2.4E**). These kinematics were nearly identical to the atomic force microscopy (Hardie & Franze, 2012) and the cornea neutralisation (Juusola et al., 2017) imaging of

[1]Throughout this thesis, the term displacement is used in place of the displacement magnitude that is a scalar quantity. Strictly however, displacement is actually a vector quantity.

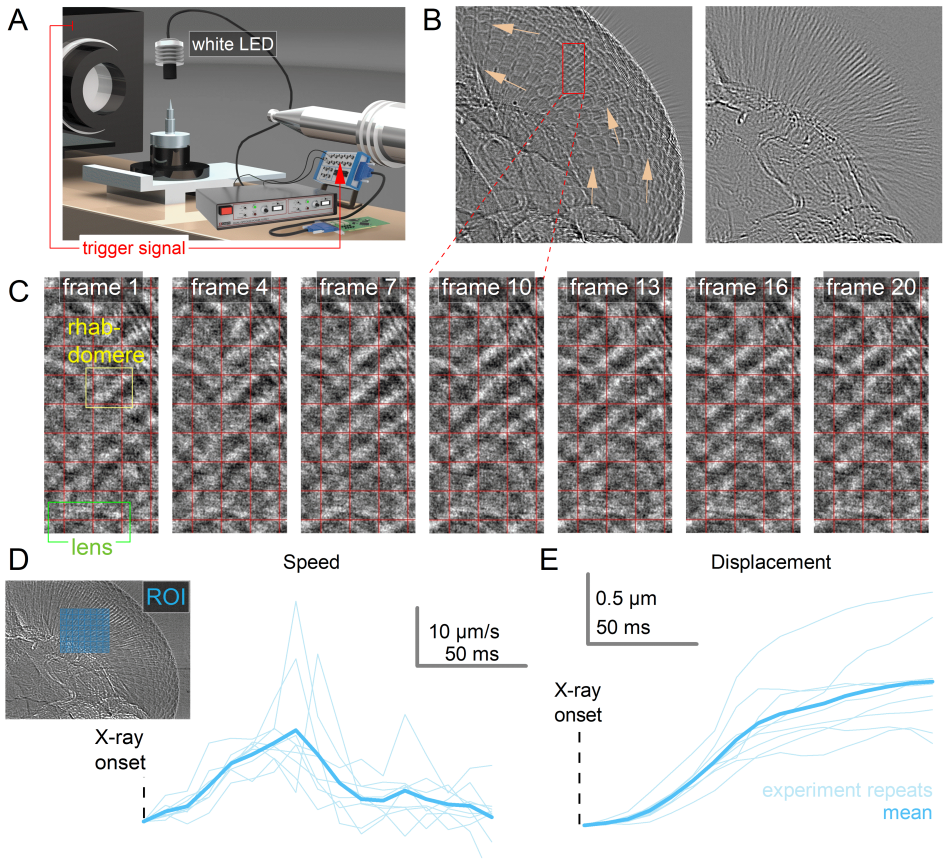

Figure 2.4: X-ray flashes lead to rhabdomere displacements. **A)** A white LED was initially added above the fly, but it turned out unnecessary: The X-rays alone made the rhabdomeres move. **B)** Stationary features were removed from the X-ray images (left) by the mean-frame-division (right), where the rhabdomeres appear as radial line segments. **C)** The lenses stayed stationary, whereas the rhabdomeres were displaced almost by their diameter. **D)** Cross-correlation motion analysis of the rhabdomeric eye region shows that the rhabdomere's speed reaches its maximum at 60 ms. **E)** The displacement follows a sigmoidal curve.

the photoreceptor microsaccades, indicating that the X-rays induced photomechanical photoreceptor contractions.

As a control, we also tested recently deceased or frozen and defrosted flies (N=4). These dead flies showed no microsaccades to X-rays, strongly indicating that the photoreceptor microsaccades were not caused by X-ray mediated tissue heating or swelling.

Overall, the X-ray imaging results show that the X-rays cause displacements of the rhabdomeres in living flies that match the photoreceptor microsaccades' kinematics, suggesting that X-rays alone can activate the phototransduction cascade.

2.3.3 X-rays activate phototransduction

Photomechanical photoreceptor contractions are likely caused by PIP_2 cleavage from the rhabdomeres' microvillar plasma membrane during the light-activation of the phototransduction cascade (Hardie & Franze, 2012). Therefore, if the X-rays activate the photoreceptors, we should be able to measure their electrical activation to X-rays using the electroretinogram (ERG) technique.

At DESY P10 beamline, ERG recording electrodes were connected to the fly's eye and torso and a bright white LED was positioned above the eye (**Figure 2.5A**). First, ERG-responses were recorded to 300 ms visible light flashes showing the characteristic, rowing boat like ERG-shape (**Figure 2.5B**). Here, at the light onset, a sharp on-transient is followed by fast activation phase that ends in saturation. At the light offset, a sharp off-transient leads to the return to the baseline. After the visible light flashes, ERG-responses were recorded to 300 ms X-ray flashes over a varied X-ray intensity range (**Figure 2.5C**) showing that the X-rays caused similar electrical activation as the visible light. At the brightest X-ray intensities, the responses were larger than the visible light responses, possibly because the X-rays activated all the imaged receptors. In contrast, the visible light flashes activated

receptors mostly facing towards the LED. This localisation follows from the ommatidia's optic isolation by the screening pigments, making the photoreceptors to accept incident light from a relatively narrow spatial angle (known as the acceptance angle). Finally, after the X-ray experiments, we re-recorded ERG-responses using the white LED to show that the photoreceptors remained functional after experiencing the X-rays (**Figure 2.5D**). These X-ray ERG experiments in wild-type flies show that the X-ray flashes cause electrical activation comparable to the visible light, suggesting that the X-rays activate photoreceptors.

To test whether X-rays activated the phototransduction, we next tested electrical activation in hdc^{JK910} , $norpA^{P24}$ and *trp/trpl* mutant flies. First, the hdc^{JK910} flies, which cannot synthesise the neurotransmitter histamine, had similar X-ray induced ERGs to the wild-type (**Figure 2.6A**), demonstrating that the X-ray ERGs required no synaptic transmission downstream from the photoreceptors. The hdc^{JK910} ERG-responses, as expected, did not show on and off transients that in the wild-type are attributed to histaminergic synaptic transmission in the lamina (Belusic, 2011; Coombe, 1986). Second, the $norpA^{P24}$ flies, in which unfunctional PLC halts the phototransduction before cleaving the PIP_2, showed no ERG responses to X-rays (**Figure 2.6B**), demonstrating that functional phototransduction is required for X-ray induced ERG-responses. These findings strongly indicate that X-rays activate phototransduction. Nonetheless, the $norpA^{P24}$ X-ray ERG responses contained electrode charging artefacts, yet these were similar to the dead wild-type control fly (**Figure 2.6C**). Finally, the *trp/trpl* flies that have no transient receptor potential (trp) or trp-like (trpl) ion channels (needed for generating the electrical light responses), showed no ERG-activation (**Figure 2.6D**), further supporting the $norpA^{P24}$ results. Together these results show that functional phototransduction is required for X-ray ERG responses, strongly suggesting that the X-rays activate the phototransduction.

In addition, I quantified the rhabdomeric movement responses in wild-type, hdc^{JK910} , $norpA^{P24}$ and *trp/trpl* flies used in the previous experiment to test if their movements were consistent with their ERG-responses. First, in wild-type flies, the movements showed X-ray intensity-dependent modulation (**Figure 2.7A**) similar to the ESRF ID16B results (**Figure**

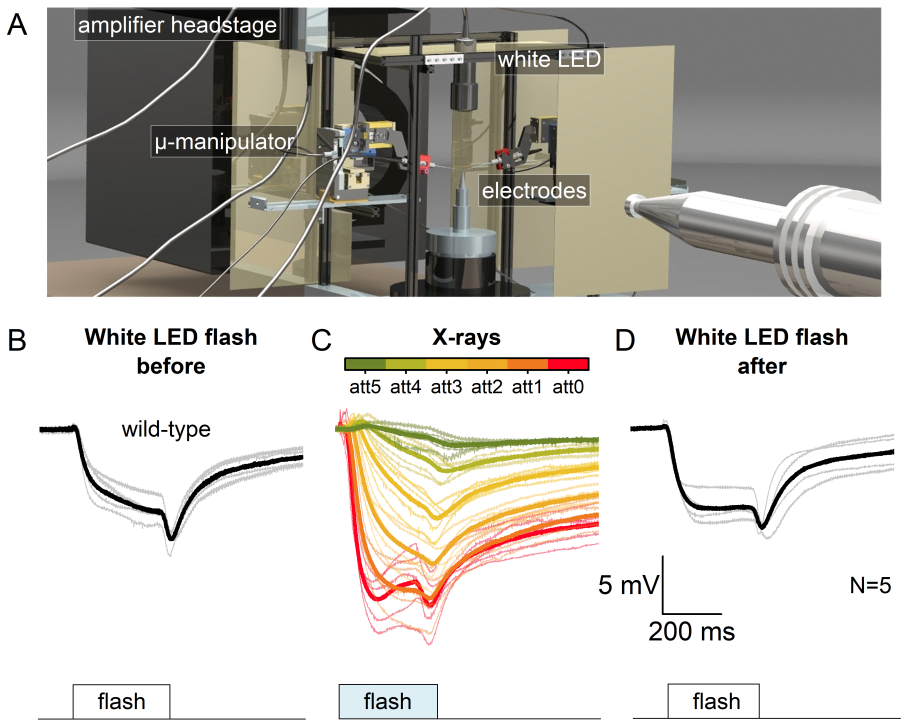

Figure 2.5: X-rays cause electrical activation in the wild-type. **A)** Micromanipulator positioned ERG-electrodes touched the fly on its shoulder and the eye, and the grounded aluminium frame with movable copper fabric curtains provided shielding against electrical noise. **B)** ERG-responses of wild-type flies to a white LED flash before the X-ray experiments show a typical boat-like shape (N=4). **C)** Wild-type ERG-responses to X-rays over a range of intensities show similar characteristics to the visible light flashes (N=5). **D)** The visible light ERG-responses after the X-ray stimulation show that the flies remained alive (N=4).

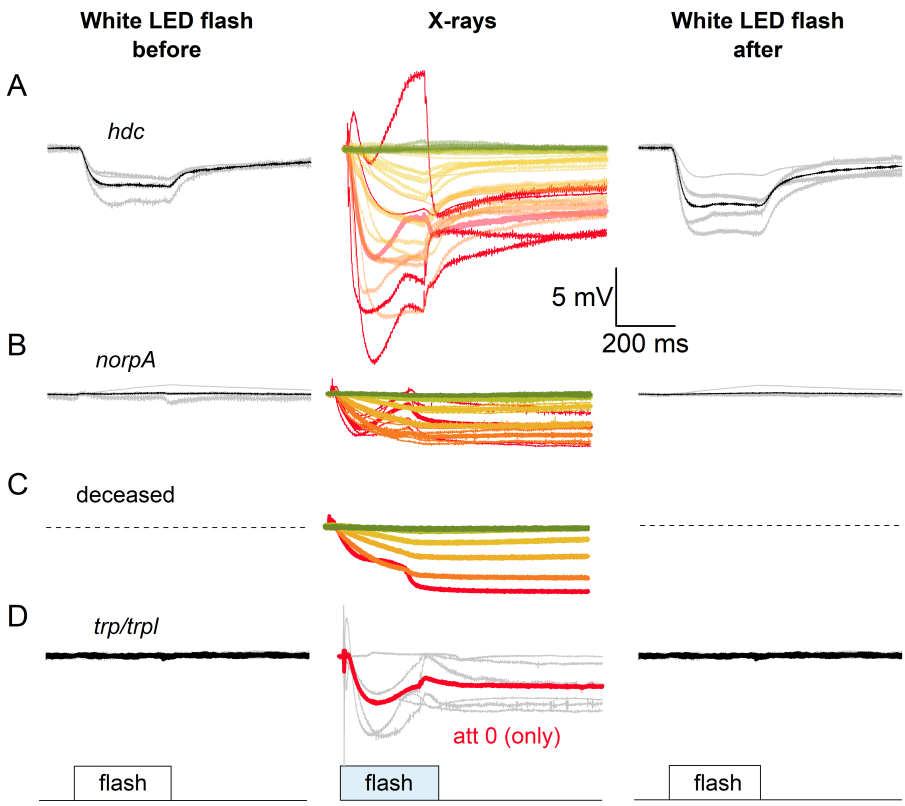

Figure 2.6: Blind mutants show that X-rays activate phototransduction. A) The hdc^{JK910} flies show electrical activation to X-rays and visible light but lack the on and off transients (N=4). Electrode charging artefacts are more prominent in the higher X-ray intensities. **B)** The $norpA^{P24}$ flies do not respond to visible light nor X-rays but show the electrode charging artefacts similar to the dead fly (N=5). **C)** A freshly killed fly shows the electrode charging artefacts that depend on the X-rays intensity (N=1). **D)** The *trp/trpl* flies show no ERG-responses to visible light nor X-rays but produce electrode charging artefacts similar to $norpA^{P24}$ and the dead fly (N=6).

2.4E). However, they were noisier, possibly because of the frequency filter preprocessing technique used in the data analysis. Second, the hdc^{JK910} expectedly showed movements (**Figure 2.7B**) consistent with the idea that the synaptic transmission downstream of the photoreceptors is not required for photoreceptor microsaccades. In addition, the hdc^{JK910} movement responses were smaller than in the wild-type, as reported before (Juusola et al., 2017). Third, the $norpA^{P24}$ flies showed no movement to X-rays (**Figure 2.7C**), demonstrating that the functional PLC molecule is needed for the receptor contractions to occur. Fourth, the *trp/trpl* flies also showed the contractions (**Figure 2.7D**) as expected because in *trp/trpl* the PIP_2 cleavage by PLC is unaltered. Finally, the *trp/trpl* responses were oscillatory following the previously reported dynamics (Juusola et al., 2017). Overall, the X-ray movement experiments support the hypothesis that the X-rays activate the phototransduction cascade leading to receptor contractions.

Taken together, the ERG experiments and the X-ray movement analysis in the wild-type *Drosophila* hdc^{JK910} , $norpA^{P24}$ and *trp/trpl* mutants univocally show that the X-rays activate the phototransduction cascade, leading to photomechanical photoreceptor contractions.

2.3.4 Microsaccades are mirror-symmetric

In some flies, the X-ray induced microsaccades occurred out-of-plane, almost as if twisting. This phenomenon likely resulted from the head's angle regarding the X-ray beam. Increasing the angle between the imaging plane and the microsaccades sinusoidally decreases the movement size. Therefore, only the two most representative flies are analysed here (two out of 14).

At ESRF ID16B, we moved the fly away from the X-ray focal spot to decrease the image magnification (**Equation 2.2**) until both eyes became fully visible (**Figure 2.8A**). Here, the X-rays were turned on for 200 ms while simultaneously imaging at 100 fps. These recordings revealed mirror-symmetric photoreceptor contractions between the left and right eyes

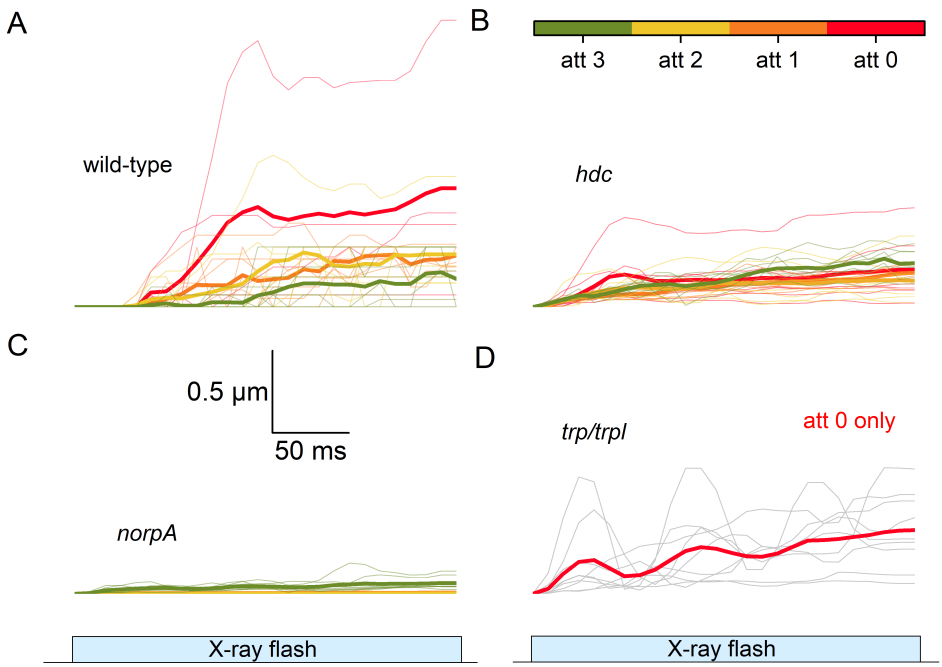

Figure 2.7: X-ray induced microsaccades in the ERG-recorded flies A) X-ray induced microsaccades in the ERG-recorded wild-type flies at DESY P10 (N=9). Preprocessing by the frequency filter. **B)** The hdc^{JK910} flies show microsaccades (N=7), but they are smaller than in the wild-type. **C)** The $norpA^{P24}$ flies show no microsaccades (N=9). **D)** The *trp/trpl* flies show oscillating movement responses (N=9).

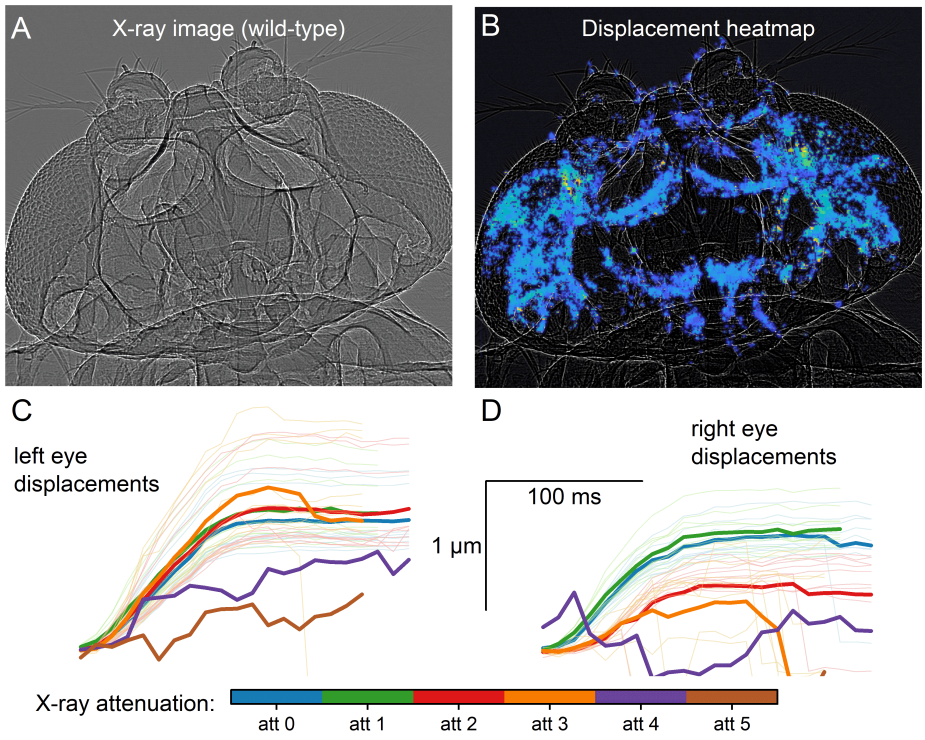

Figure 2.8: Left and right eye microsaccades are mirror-symmetric A) An X-ray image of a wild-type fly left and right eyes. **B)** In the displacement heat map, the blue, green and yellow colours reveal the displacements from the smallest to the largest, in this order. **C)** Displacements of the left eye quantified from the photoreceptor region show dependence in X-ray intensity. **D)** The right eye displacements appear similar to the left eye, supporting mirror-symmetry.

where the front-facing receptors moved the most (**Figure 2.8**). Interestingly, some structures inside the head also move during the X-ray flash, possibly reflecting the pull-force of the contracting photoreceptors. Laterally quantified contraction kinematics appeared similar in the left and right eyes (**Figure 2.8C** and **D**), showing that the left and right eye receptors activated simultaneously.

These lower-magnification experiments demonstrate that the X-ray induced photoreceptor microsaccades were mirror-symmetric.

2.3.5 Microsaccades may have spatial specialisations

Next, I analysed the microsaccades' displacement sizes and speeds along the receptor side profile to see if they followed any recognisable patterns. The analysis was performed using the representative ESRF wild-type fly, where the rhabdomere motion occurred along the image plane.

First, the cross-correlation motion analysis along the eye depth shows that the photoreceptors' proximal ends near the basement membrane moved more than their distal ends (**Figure 2.9A**), pulling the basement membrane. The motion was also registered deeper in the lamina, but here, unfortunately, the neural ultrastructures are smaller and their movements possibly underestimated. Finally, the speed and displacement profiles were similarly shaped, and the lenses remained nearly still, as expected.

Next, the cross-correlation analysis along the top-bottom axis shows that the front-facing receptors located medially moved the most (**Figure 2.9B**), which possibly is a dynamic stereo vision (Kemppainen, Scales, et al., 2021) specialisation on the binocular overlap area. The receptive field (RF) displacements here would have been large, as already a 1 µm rhabdomere shift causes a 3.56° shift of the RFs (Juusola et al., 2017). Interestingly, whilst the displacement profile decreases near monotonically with increasing rotation from the top, the speed profile has a bump between the 20° and 60° rotations. This bump may represent local tuning to the optic flow, because, during forward flight, objects on the sides of the fly would appear to move faster.

Overall, the motion analysis along the receptor side profile suggests that microsaccades may be tuned to pull the basement membrane, move more and faster on the binocular overlap area, and move faster where the optic flow is faster.

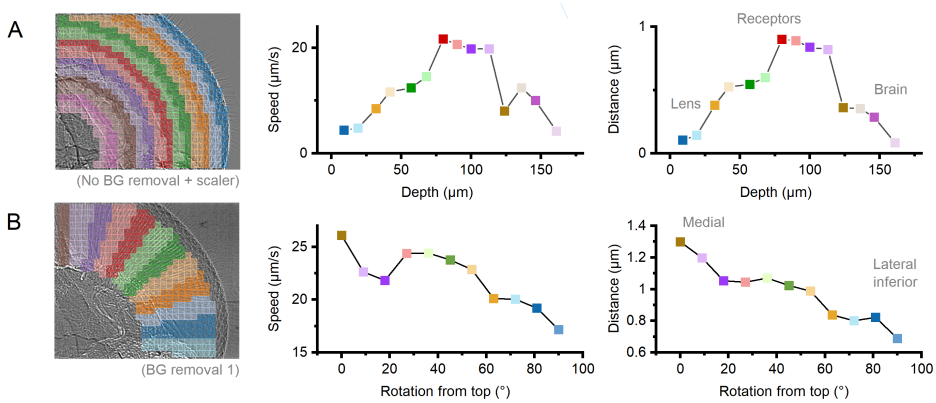

Figure 2.9: Spatial analysis of X-ray microsaccades suggests specialisations. **A)** X-ray induced microsaccades were analysed radially (left inset), revealing the speed (middle) and displacement (right) kinematics. The analyses show that the proximal receptor ends move the most. **B)** Similar analyses along the top-bottom axis show that the frontal receptors move the most, revealing speed specialisation to the optic flow.

2.4 Discussion

The objectives in this study were to image photoreceptor microsaccades, along with the side profile (in semi-sagittal or semi-coronal planes) using high-speed synchrotron X-ray imaging at DESY P10 and ESRF ID16B beamlines, and to better resolve the photoreceptor's axial contraction. Overall, these objectives were met. These results are further discussed below.

2.4.1 Phototransduction activation by X-rays

Our finding that the X-rays activated the receptors' phototransduction was unexpected. The synchrotron X-rays had more than a thousand times smaller wavelengths than the photoreceptors are tuned to detect (Stark et al., 1976).

X-ray induced photoreceptor activation has been previously reported in frogs (Lipetz, 1955a). Similarly, the X-rays cause visual sensations in humans. Irradiation of the entire human eye leads to homogeneous luminous glow, described as yellow-green or blue, depending on the X-ray generator's voltage (Lipetz, 1955b). In addition, olfactory bulb neurons in cats, rabbits, and frogs have been shown to respond to X-rays (Cooper & Kimeldorf, 1967). Still, these experiments were performed by exposing the whole animal to the X-rays and not identifying the X-ray detecting cells or anatomical regions. Overall, there are good evidence that X-rays can lead to visual sensation.

Our X-ray and simultaneous ERG experiments indicated that the X-rays lead to phototransduction activation. But how exactly this happens remains unclear. One explanation is that the X-ray photons directly activate rhodopsin, leading to its isomerisation to metarhodopsin. It is also possible that the X-rays break down the Cg, releasing its CGα subunit that activates PLC. Another explanation could be that the X-rays interacting with the tissue create secondary particles such as visible light photons that commonly activate phototransduction. These visible-light photons can be created in the Compton scattering (Als-Nielsen & McMorrow, 2011, pg. 16) or by secondary electrons released in the photoelectric absorption or the Auger emission (Als-Nielsen & McMorrow, 2011, pg. 19). However, in the case of the frog, no secondary photons were observed, leading to the conclusion that the X-rays directly activated the receptors (Lipetz, 1955a). In our synchrotron experiments, much higher energies (hard X-rays) were used than those with the frog (soft X-rays), making the secondary photons still a plausible source of the transduction activation.

Overall, it seems that flies and other animals can sense X-ray radiation. However, they cannot use it to form images because the lenses do not refract the X-rays. It also remains unknown if they can distinguish X-rays from visible light. More research is needed to determine whether the photoreceptor X-ray activation is evolved or an unavoidable or unexpected (random) consequence of X-ray matter interaction.

2.4.2 X-ray imaging technique

The high-speed synchrotron X-ray phase-contrast imaging experiments in alive *Drosophila* eyes were made possible thanks to our collaborators, the beamline and synchrotron staff and organisations, and my lab colleagues. The most significant advantages of the X-ray imaging technique was its ability to see inside the eye with adequate contrast without any external contrasting agents in living flies. Any other approach would likely not achieve these results with the spatial and temporal resolution that the X-ray imaging provided.

However, the X-ray imaging method had a major technical disadvantage. Because X-rays were both used to activate photoreceptors and form the image of the eye, the stimulation and illumination were therefore hard-coupled to each other. This coupling prevented us from imaging the microsaccades' slower relaxation phase after the X-rays were shut down or the photoreceptors' motion before the X-ray flash. Likewise, the intensity series experiments were negatively impacted by the reduced image quality in the lower X-ray intensities because lowering the X-ray intensity meant lower signal-to-noise ratio.

The ERG recordings served as an independent technique to record photoreceptors' electrical activation and correlate it to the used X-ray intensity. In addition, the hdc^{JK910} , $norpA^{P24}$ and *trp*/*trpl* mutants enabled establishing that the X-rays activate the phototransduction. However, the ERG recordings were negatively impacted by the X-ray induced electrode charging artefacts (**Figure 2.6**), which are likely a result of X-ray induced ionic currents (Schön et al., 2017). To avoid these artefacts, it may be necessary to shield the electrodes from the X-rays with lead or similar metals or avoid placing them on the X-rays path.

Interestingly, not all the tested wild-type flies responded (~20% showed no microsaccades). This may be caused by preparation damage as the flies were squeezed through the plastic pipette tip. A more speculative explanation is in the flies' circadian rhythm; One time, between 9pm and 2am, unusually many tested flies (~80%) showed no the microsaccades. Hypothetically, it may be beneficial for the fly suppress the photoreceptors' activity and

contractions when they are not needed, if it yields energetic savings. This anecdotal finding can be tested by recording the microsaccades in different light cycle times in a controlled manner.

In the future, it may be interesting to add an optical microscope using cornea neutralisation (Juusola et al., 2017) or deep pseudopupil (**Chapter 3**) technique to view the microsaccades independently from the X-rays. These combined methods would allow quantifying the X-ray induced microsaccades in much lower X-ray intensities and testing whether the X-rays generate any measurable visible light photons inside the eyes that activate the phototransduction.

2.4.3 Preprocessing for motion analysis

Quantifying rhabdomeres' motion from the X-ray image series is challenging because the images also contain stationary objects and represent 2-dimensional shadows, created by all the tissue on the X-ray beam's path. I tested two preprocessing techniques to remove the stationary features: frequency filtering and background subtraction. First, the frequency filtering technique creates a mesh of randomly oriented edges (**Figure 2.1B**) that move with similar kinematics to the unprocessed images. These edges were a strong feature that the cross-correlation stuck well onto. Still, the disadvantages were that some of the edges were parallel to the motion, leading to underestimated motion, the loss of spatial specificity and the edge motion not being purely translational.

The second technique, background subtraction, divided each X-ray image by the pixel-wise minimum or mean frame of the recording, respectively, resulting in a partial or full background subtraction (**Figure 2.2**). This technique worked better when there was a movement to analyse but failed in the absence of motion. Overall, the partial background subtraction gave better results, but more research is needed to make this decisive.

2.4.4 Specializations and mirror-symmetry

The photoreceptor side-profile motion analysis (**Figure 2.9**) suggested that there may be at least three different spatial specialisations in the microsaccades. First, the rhabdomere proximal ends move the most (**Figure 2.9A**), likely pulling and deforming the receptors and the lamina neurons. Motion artefacts reported in fly brain calcium imaging (Mann et al., 2017; Seelig et al., 2010) can be at least partially caused by contracting photoreceptors.

Second, the photoreceptors within the binocular overlap range moved more and faster than those located more medially (**Figure 2.9B**). Based on our recent publication about dynamic stereo vision theory, where mirror-symmetric photoreceptor microsaccades allow flies to correlate phase differences (Kemppainen, Scales, et al., 2021), frontal photoreceptors' larger movement appears to be a specialisation to perceive depth better by moving the RFs more.

Finally, it seemed that the more lateral photoreceptors, experiencing the fastest optic flow, moved faster than expected from their movement size (**Figure 2.9B**). On the other hand, the most lateral receptors, located 60° or more from the top, move however less and slower, although the optic flow experienced by them is even faster.

The motion analysis results behind the other putative specialisations were, however, quantified from the 2-dimensional X-ray-projections that essentially are the collective shadow created by all the tissue within the X-ray beams path. Conclusive results would likely require tomographic 3D reconstructions, but these have not been yet successful for our data set.

3 DPP-microsaccades across the eyes

3.1 Introduction

In chapter 2, the synchrotron X-ray experiments revealed how the mirror-symmetric photoreceptor microsaccades occur in 2D radiographic projections under simultaneous and global X-rays stimulation. However, these semi-coronal or semi-sagittal projections themselves did not offer adequate 3-dimensional information about the microsaccades unless 3D reconstructed. Our collaborators' (lead by Prof. Rajmund Mokso) computer tomography (CT) reconstructions have been so far unsuccessful, possibly challenged by X-ray damage, limited contrast or animal movements during the CT scans. The corneal neutralisation technique that has been previously used to image photoreceptor microsaccades (Juusola et al., 2017) could be adapted to rotate the fly in a controlled manner using goniometric devices and obtain data in three dimensions. However, this procedure is impractical because the immersion fluid must be applied between the fly eye and the microscope objective to neutralise the facet lenses.

The deep pseudopupil (DPP) is a superimposed, magnified virtual image of the rhabdomere tips created by the compound eye lens system (Franceschini, 1972). Under antidromic illumination (illumination coming from behind the fly), it appears nearly identical to the ommatidium's trapezoidal R1-R7/8 arrangement with seven bright spots. Observing the DPP requires a microscope with a sufficiently narrow depth-of-field that is focused approximately 200 µm underneath the lenses, to the intersection point of ommatidial axes. Here, the virtual images created by the individual lenses and ommatidia align and superimpose near perfectly, but the exact amount of ommatidia participating in DPP image

formation depends on the interommatidial angle and the numerical aperture (NA) of the used microscope (Kemppainen, Mansour, et al., 2021): Smaller the interommatidial angle or higher the NA, higher the amount of DPP pooled ommatidia.

The DPP method is a an efficient technique to extract various information about the retinal tissue non-invasively in living flies. First, because a sharp and clear DPP pattern requires precisely organised rhabdomeres across the neighboring ommatidia, the DPP method has been used to study retinal degeneration where this organisation is lost (Y. Huang et al., 2015; Kurada & O'Tousa, 1995; Zelhof et al., 2003). Second, because the rhabdomeres forming the observed DPP image are those that face towards the microscope's entrance pupil, the DPP method can be used to measure the binocular overlap, the amount of visual space shared and seen together by the left and right eyes (Seidl & Kaiser, 1981). Third, because the DPP in the *Dipteran* eye is a superimposed image created by many ommatidia, it can be used to find the equator that divides the eye into dorsal and ventral mirror-image fields based on the R1-R7/8 rhabdomere arrangement (Beersma et al., 1977). In summary, the DPP method views the retina non-invasively in living flies. It benefits from the free 10x magnification (Franceschini, 1972) provided by the fly's lens system.

To investigate photoreceptor microsaccades across the left and right compound eyes, I built and prototyped a goniometric high-speed deep pseudopupil (GHS-DPP) microscopy system and the related acquisition and data analysis software packages. Goniometric here means that the system is able to measure angles and rotate the fly to a precise angular position. Similar computer-assisted or automated goniometric systems with optical microscopy have been developed earlier to extract compound eye parameter distributions (often optical axes or lens diameters) by observing the corneal pseudopupil across the eyes, sometimes together with the DPP (Arias et al., 2021; Dahmen, 1991; Douglass & Wehling, 2016; Krapp & Gabbiani, 2005; Petrowitz et al., 2000; Smolka & Hemmi, 2009). However, the GHS-DPP microscopy differs from these previous imaging systems by high-speed DPP imaging (>100 Hz) and time-accurate (<1 ms) bright light stimulation through the microscope itself to image dynamic retinal micro-movements across the eyes. To avoid confusion, in this

study, the DPP viewed microsaccades are referred to as DPP-microsaccades to reflect the fact that the DPP is a 10 times magnified image of the rhabdomere tips. Hence, the measured displacements are proportionally larger.

The DPP-microsaccade data I obtained using the GHS-DPP system reveals how the microsaccades occur across the compound eyes in the fly's frame-of-reference. My results are overall consistent with those of the atomic force microscopy (Hardie & Franze, 2012), the cornea neutralisation technique (Juusola et al., 2017) and the synchrotron X-ray imaging (**Chapter 2**) but reveal new nuances about the microsaccades such as their curved motion paths. In addition, I simulated the optic flow of a forward flying fly, and quantified the receptive field (RF) movement phases. The comparison between the optic flow and the RF phases suggests that the RF fast-phase is overall better aligned to the optic flow in typical flight positions, and that the pitch, roll and yaw rotations have distinct roles in the alignment. I also quantified the R1-R7/8 rhabdomere pattern orientation across the eyes and compared it to the DPP-microsaccades. I found that the rhabdomeres mostly moved along the R1-R3 axis, indicating that the rhabdomere orientations may developmentally set the microsaccade directions. Interestingly, there is also a similar alignment between the rhabdomere orientations and the optic flow, indicating that the rhabdomere orientations themselves may be aligned to the optic flow.

3.2 Methods

3.2.1 Flies and preparation

Alive wild-type (Berlin), hdc^{JK910} and $norpA^{P24}$ flies were used to investigate photoreceptor microsaccades across compound eyes. The hdc^{JK910} flies have unfunctional histidine decarboxylase molecules preventing the neurotransmitter histamine synthesis in

photoreceptors. Consequently, these flies have functional phototransduction but no synaptic information transfer from photoreceptors to downstream neurons rendering the flies blind. The *norpA*^{P24} flies have a null-mutation of the phospholipase C protein (PLC) that is required in the phototransduction cascade to hydrolyse the phosphatidyl-inositol 4,5 biphosphate (PIP_2) (Hardie & Franze, 2012) As a result, their photoreceptors cannot respond to light, and these flies are blind, showing no measurable electrical activity. The flies were maintained in an incubator set at 25°C under a 12:12h light-dark cycle and fed with standard brown (molasses) fly food (Table 2.1). The plastic vials that the flies were grown in were plastic cylinders with their open end sealed using a cotton plug.

Healthy 3 to 25 days old male and female flies, able to climb up the vial, were selected for the experiments and their genotype, sex and age were registered. Very young flies (<3 days) were not used for the experiments because their heads were not yet rigid but could deform without external stimulation, presumably due to spontaneous eye muscle activity. The flies were prepared for the experiments using the plastic pipette tips/beeswax protocol (**Figure 3.1A**).

First, a 1,000 µl plastic pipette tip was attached to a funnel piece connected to a vial with flies (**Figure 3.1B**). Driven by their innate antigravitaxis behaviour, the flies moved automatically upwards, which allowed easily luring one fly at a time into the pipette tip. Flies were, therefore, immobilised without using carbon dioxide (CO2) or ice-cooling, which can potentially affect the microsaccades during the experiments. Next, the pipette tip was viewed under a stereo microscope (Olympus SZX-9, Japan) and the fly was gently pushed towards the tip's small end by puffing air from a hand-held syringe until the head and part of the upper thorax came above the tip line (**Figure 3.1C**). If needed, the pipette tip's opening was enlarged using a razor blade to ensure that the fly head passed through without significant deformation, minimising structural damage to the eyes. After the fly was ideally positioned, it was quickly immobilised in the pipette tip by applying melted beeswax first on its thorax (**Figure 3.1D**), head and proboscis (**Figure 3.1E**). In the ideal position, the pipette would not shadow the infrared illumination during the experiments. Finally, the pipette tip

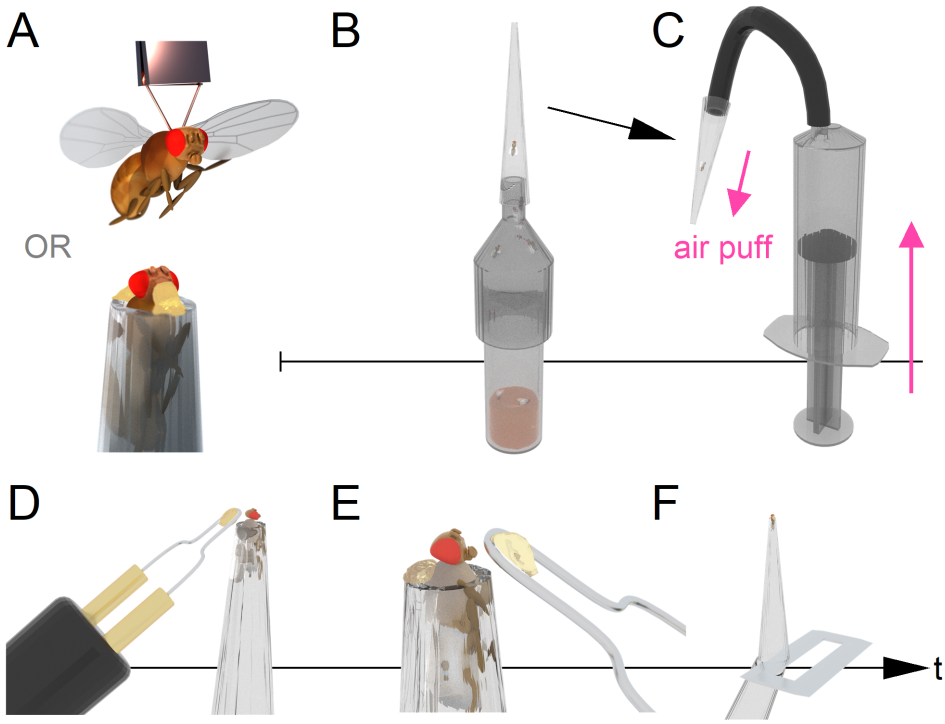

Figure 3.1: The pipette tip preparation technique. **A)** Flies can be tethered on a copper hook with UV-cured glue or immobilised on a plastic pipette tip with beeswax. **B)** A fly was taken from a vial full of flies using a funnel piece. **C)** A syringe generated air puffs pushing the fly towards the pipette tip's small end. **D)** Beeswax was applied on the fly's dorsal thorax to immobilise the body. **E)** More beeswax was applied on near the proboscis to immobilise the head. **F)** Any excess pipette tip was cut off with a razor blade and then the preparation was inserted into the GHS-DPP system.

was cut to a correct length (about 4 cm) with a razor blade (**Figure 3.1F**), and the prepared fly was mounted in the GHS-DPP setup.

In the waxing procedure (**Figure 3.1D** and **E**), few additional steps were briefly tested but omitted. For example, when preparing *Drosophila* for intracellular electrophysiology, the proboscis is often pulled out and waxed on the pipette or the antennae are fixed with beeswax to immobilise the fly better. However, these procedures made no apparent difference in the observed microsaccades, but they would have prolonged the preparation making, potentially increasing structural damage to the eyes. Conversely, some wax was routinely applied on the dorsal side of the head, just under the ocelli, to further secure the head's position.

3.2.2 GHS-DPP imaging system

The goniometric high-speed deep pseudopupil (GHS-DPP) imaging system was the main instrument used in this study. It consisted of two main components: the rotation stage system and a sideways mounted stereo microscope (**Figure 3.2A**). The rotation system allowed precise control over the rotation of the fly by using two perpendicularly mounted rotation stages (Thorlabs PR01/M, USA), one being the horizontal and the other the vertical rotation stage. The vertical stage controlled the pitch rotation of the fly and the horizontal stage rotated the fly along an axis perpendicular to the pitch rotation axis and to the horizon. A small 3-axis micromanipulator was connected to the vertical stage to allow positioning the fly with respect to the rotation stages. The horizontal rotation stage rested on a 2-axis micromanipulator so that the intersection point of the two rotation stage axes could be correctly centred at the microscope's field of view. The rotation stage positions were acquired digitally, using two 1024-step rotation encoders (YUMO E6B2-CW23E, China) and an Arduino board (Arduino Uno, Italy) running a custom program (**Figure 3.2B**). In addition, the rotation stages were fitted with stepper motors for fully automated experiments. In

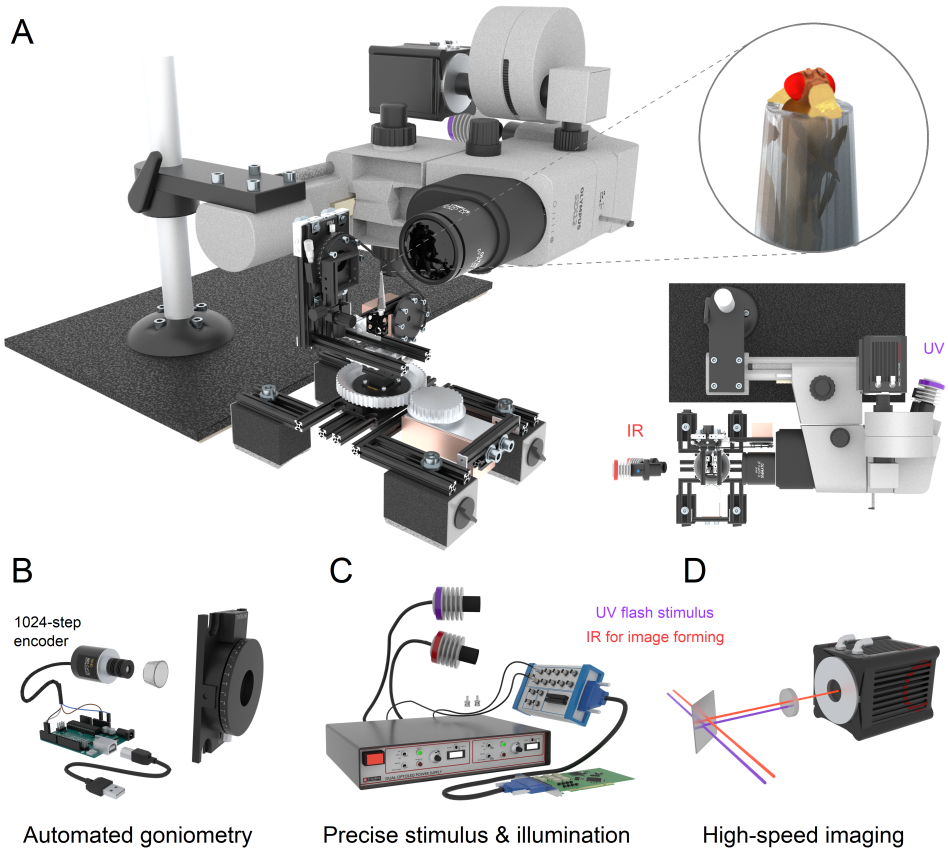

Figure 3.2: Goniometric high-speed deep pseudopupil (GHS-DPP) imaging setup. **A)** Sideways mounted stereo microscope with high-speed camera viewed the preparation mounted on a goniometric rotation stage system. The antidromic illumination settings were created with two infrared (IR) LEDs, and photoreceptor microsaccades were induced by ultraviolet (UV) LED flashes through the microscope's ocular slot system. **B)** The horizontal and vertical stage rotations were read using two 1024-step rotary encoders and an Arduino microcontroller over a USB serial connection. **C)** The illumination and stimulus LEDs were controlled using the data acquisition (DAQ) system over the BNC interface. **D)** To uncouple the UV stimulus from the imaging pathway, an IR passing but UV blocking optical filter was inserted in the front of the camera sensor.

this thesis however, the stages were rotated by hand since the fully automated experiments would require additional control software to maintain the focus on the DPP.

The stereo microscope was mounted sideways to make the microscope move in great circles (orthodromes) from the fly's point of view when rotating the stages. A bright ultraviolet LED (UV-OptoLED, Cairn Research, UK) was inserted in the microscope's ocular slot, enabling light stimulation of those photoreceptors rhabdomeres that were forming the DPP image. Two 850 nm infrared LEDs (IR-OptoLED, Cairn Research, UK) provided antidromic illumination (Franceschini, 1972) that the flies could not see. All LEDs were connected to their separate driver unit (Dual OptoLED Power Supply, Cairn Research, UK), which was controlled over the BNC interface using a computer connected data acquisition (DAQ) system (PCI-6221 with BNC-2090A and PCI-6733 with BNC-100, National Instruments, USA) (**Figure 3.2C**). The two infrared LEDs were mounted apart from each other at different angles to prevent the pipette tip or the fly body from blocking the infrared illumination at specific fly rotations. The infrared LEDs were inserted in their holders that had a convex lens with adjustable lens-to-LED distance, enabling infrared focus on the head capsule. The second critical unit mounted to the microscope was the high-speed optical camera (Orca Flash 4.0 C13440, Hamamatsu, Japan), which sent trigger signals over the BNC interface to the DAQ for precise stimulus timing. The camera had a full-frame resolution of 2,048 x 2,048 pixels which it could operate at 100 frames-per-second (fps). However, to improve the images' signal-to-noise ratio and reduce the generated data, it was 2x2 binned to 1024x1024 pixels running still at 100 fps. The camera had an infrared transparent but opaque ultraviolet filter on its pathway that ideally stopped any UV stimulation light from entering the camera sensor (**Figure 3.2D**). In addition, the microscope had a beam-splitter (SZX-BS, Olympus, Japan), a photo adapter piece (SZ-PHA, Olympus, Japan) and a magnification changer (U-TVCAC, Olympus, Japan).

The setup was mounted on a vibration decoupling air table, which prevented any building vibrations from affecting imaging results. The rotation stage system was connected to the table using magnetic clamps (Magnetic Stand, World Precision Instruments). In contrast,

the microscope rested on a thick steel pole attached to a steel base plate, heavy enough to stay in place without fixation. The whole setup was enclosed in a black-painted metal cubicle with an open side, where black curtains allowed performing experiments in controlled, dark conditions. The Arduino board's surface-mounted LEDs were covered with electrical insulation tape to eliminate their light scatter.

3.2.3 Data acquisition and imaging

To efficiently image DPP-microsaccades from over 200 locations across the eyes, I created a recording software named *GonioImsoft* using the Python programming language. It interfaced with the open-source microscopy software *MicroManager* to control the high-speed camera, used the NI-DAQmx module (NI-DAQmx, National Instruments, USA) to control the data acquisition system and the *PySerial* module to communicate with the Arduino microcontroller for rotary encoder readout. The *GonioImsoft* software ran on the Windows platform (Windows 10 Education, Microsoft, USA).

In the experimental preparations, the microscope was fitted with a 1x objective (DF-PLAPO 1X, Olympus, Japan), the microscope's continuous zoom was maxed out and the magnification changer was set to a 2x-position. With these settings, an average sized head fitted the camera sensor, completely filling the field of view without getting cropped. The microscope's beam-splitter was set to its mid-state to divide 20% of the collected light to the eyepieces and 80% to the camera, allowing simultaneously to activate receptors with a UV flash through the ocular slot while imaging. The infrared illumination LEDs were directed and focused on the fly head so that the perceptual image quality and the image brightness were maximised. The 2-axis micromanipulator that hosted the rotation stages and the 3-axis micromanipulator hosting the fly were trial-and-error adjusted so that the fly remained in the field of view in all possible rotations. However, the microscope's focus remained only approximately correct since the fly head is not perfectly round and therefore refocusing was

needed to maintain a DPP image during the experiments. This slow procedure of adjusting the infrared illumination and the 2-axis manipulator had to be done for the setup only once, and the future experiments were performed significantly faster.

In the beginning of the experiments, the microscope was first focused on making facet lenses appear sharp and clear. Then, using the two rotation stages, the fly was rotated to 0° horizontal (both eyes equally visible) and the zero vertical rotation set so that the left and right eye DPPs aligned with the antenna pedicels. At this zero rotation, a still image was taken to document the fly's appearance. Next, the focus was adjusted deeper into the eye until the DPP pattern emerged and the fly was rotated to fully show the frontal DPP pattern in the left or right eye.

The DPP-microsaccades were induced with a 200 ms UV flash while recording the DPP with the high-speed camera running at 100 fps, capturing in a total of 20 frames-per-flash. The camera and LED onsets were synced using a trigger signal coming from the camera to the data acquisition system (DAQ). If the DPP-microsaccades were observable in the first captured images, the fly was then imaged fully by rotating it in 10° steps from -60° to +40° in the horizontal rotation (limited by vertical rotation stage covering the illumination LEDs or colliding with the objective) and in 10° steps from -110° to +110° in the vertical rotation. At each rotation, the DPP-microsaccades were recorded using the 200 ms flash protocol, giving approximately 200 distinct locations on the left and right fly eyes. Reorienting the fly and refocusing at the DPP took approximately 10 s, during which the fly was in darkness recovering from the previous flash (inter-stimulus-interval, ISI).

3.2.4 Data analysis

To analyse the DPP movement data and quantify the 3-dimensional rhabdomere movement fields, I prototyped a data analysis software named *GonioAnalysis* using the Python programming language. This software allows selecting regions of interest (ROIs) around the

DPP, performing motion analysis and translating the motion analysis results from the 2D camera image coordinates to the 3D coordinates in the fly's frame-of-reference, using the digitally read rotary encoder values.

In the motion analysis, the rectangular ROIs were first drawn by hand for the first frame of each imaging location by selecting the DPP from the images. These ROI-cropped DPP images were then used as template images for cross-correlation based motion analysis. The *matchTemplate* function from the open-source vision library *OpenCV* (Bradski & Kaehler, 2000) was used cross-correlate the template and source images, already presented in **Equations 2.3**, **2.4** and **2.5**. This cross-correlation (**Figure 3.3A**) gave result images, each denoted by R, where higher pixel values indicate higher similarity between the template and source images at that particular location (**Figure 3.3B**). Taking the peak value locations of the resulting R image set (ie. argmax operation) and subtracting the $t = 0$ location from the resulting array, the displacements of the DPP were quantified. (**Figure 3.3C**). To shorten the time it takes to run the motion analysis and to avoid false matches, source images were also cropped to the vicinity of the DPP using 30-pixel padding that was shifted according to the earlier-frame motion analysis result. This padding was confirmed to be large enough not to truncate the DPP responses.

After the motion analysis, the DPP-microsaccades were in the camera sensor coordinate system as x and y image coordinates. These were translated to the 3D space in the fly's frame of reference using the digitally read vertical v and horizontal h rotation stage values (**Figure 3.3D**). First, the following set of equations

$$\begin{cases} y = \cos(h)\cos(v) \\ z = y\tan(v) \\ \|x\| = \sqrt{1 - y^2 - z^2} \end{cases} \tag{3.1}$$

were used to calculate the microscope's (x, y, z) location as seen by the fly. The camera x unit

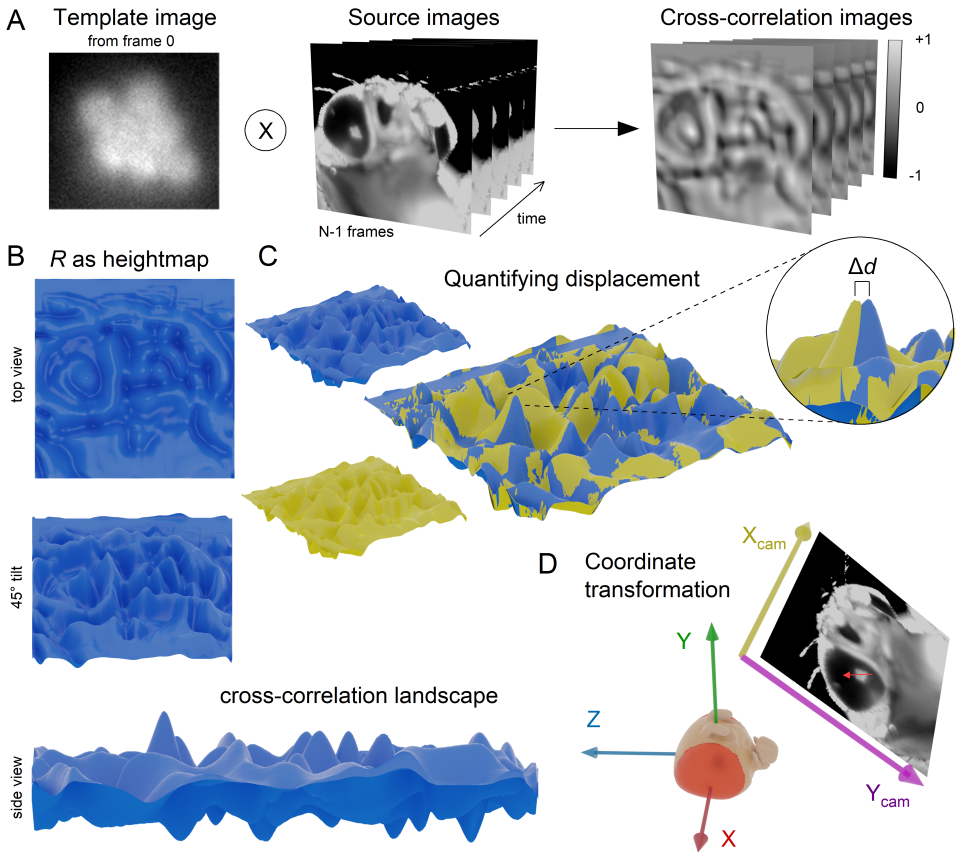

Figure 3.3: Motion analysis by cross-correlation based template matching. **A)** Manually cropped DPP of the first frame (t=0) was used as the template image and its locations were searched among the 19 source images by cross-correlation. This procedure produced result images R, where the brightest pixel reveals the location of the template. **B)** Alternatively, R can be presented as a height-map, giving a better view of the cross-correlation landscape. **C)** Two superimposed R heightmaps from different time points reveal a slight shift in the peak locations, Δd. This difference is the displacement of the DPP between those frames. **D)** The motion analysis results were transformed from the camera image coordinate system to the fly head coordinate system using the rotation stage values.

vector was calculated using the same equation set, shortly denoted by $P(h, v) \rightarrow (x, y, z)$, as the vector from the point $P(h, v)$ to a slightly displaced point $P(h + \Delta h, v)$, which can be denoted as

$$\hat{i}_{cam}(h, v) = \overrightarrow{P(h, v)P(h + \Delta h, v)} \tag{3.2}$$

where Δh is ideally as small as possible but large enough not to cause an error due to the limited floating-point precision of computer arithmetics. For the camera y unit vector $\hat{j}_{cam}$, a simple polynomial formula was used because $\hat{j}_{cam}$ only depends on the vertical rotation and its x-component is conveniently always zero. From the fly's point of view, $\hat{j}_{cam}$ is always perpendicular to the great circle that the microscope travels along when rotating the horizontal stage, at any vertical rotation

$$\hat{j}_{cam}(v) = -sin(v)\hat{j} + cos(v)\hat{k} \tag{3.3}$$

Finally, using the calculated camera unit vectors, the 3-dimensional movement vectors in the fly's frame of reference were calculated as

$$\vec{v}(m_x, m_y, h, v) = m_x \hat{j}_{cam}(v) + m_y \hat{j}_{cam}(v) \tag{3.4}$$

where m_x and m_y are the camera image x- and y-movement values produced by the cross-correlation motion analysis. All these vectors and their locations (**Equation 3.1**) form DPP-microsaccade vector map that shows the DPP movement directions across the left and right eyes at the recorded locations. To reveal these movement direction trends more clearly, the vectors maps of many flies were averaged together using a simple N-nearest neighbour interpolation as follows. For each interpolation point, for each of the N flies, the nearest vector was selected if the angular distance of the vector was not larger than 2-times the

angular interpolation step of 5°. These equal or less than N vectors were averaged together only if there were $N/2$ or more of them or otherwise the interpolation point was left blank, without a vector. Finally, the visual vector maps graphs were generated using the Matplotlib module (Hunter, 2007), and the figures were arranged using the OriginPro graphing software (OriginPro 2020b, OriginLab, USA).

Rhabdomere orientation fields across the eyes were analysed from the already captured DPP-microsaccade imaging data using the first frames only. In the analysis procedure, a line was drawn from the R3 to the R6 DPP-rhabdomere at each imaging location. This R3-to-R6 long axis of the DPP pattern was easily and accurately identified across the images, even for less well-focused or noisy recordings. At the equator, where the DPP is a fused image of the ventral and dorsal rhabdomere patterns, two lines were drawn: One from the ventral R3 to the corresponding R6 and one from the dorsal R3 to the corresponding R6. These 2D line segments in the camera image coordinates were then converted to 3D vectors in the fly's frame-of-reference using **Equation 3.1** and **Equation 3.4** to calculate the vector's position and the vector itself, respectively. Finally, the resulting rhabdomere orientation maps were averaged together similar to the DPP-microsaccade averaging algorithm and their graphs were generated.

3.3 Statistical methods

The DPP-microsaccades' response amplitudes were compared between the wild-type, hdc^{JK910} and $norpA^{P24}$ flies (**Figure 3.7.**) Statistical hypothesis testing was performed using the *scipy* (v1.7.3) and *statsmodels* (v0.13.1) Python libraries as described below.

First, it was confirmed by a normality test (`scipy.stats.normaltest`) that the data followed a normal distribution Hence, next, a two-sided Welch's t-test (`scipy.stats.ttest_ind`) was used to test whether any of the three groups had statistically

different means (α=0.05). The Welch's t-test was used because it is more robust under unequal variances and sample sizes than the Student's t-test (West, 2021) Finally, the p-values were Holm-Šidák adjusted (`statsmodels.stats.multitest.multipletests`) to control the family-wise error rate (the probability of finding false positives).

3.3.1 Optic flow simulations and field error

The directions of the optic flow field as experienced by a forward flying fly were calculated using a simple sphere-tangent algorithm. The flow directions depend on the rotation of the head with respect to the locomotion direction and this rotation can be unambiguously expressed using three axes of rotation (yaw, pitch, roll) when any two axes have been fixed by some rules. For the head of the fly, the pitch axis is naturally set by the left-right symmetry. The roll axis is defined here through the zero rotation (0°, 0°, 0°) to match with the GHS-DPP coordinate system. At zero rotation, the antennae point towards the positive y-axis so that an observer located on the positive y-axis would see the DPP aligning with the antenna pedicels. Then the yaw axis is simply perpendicular to the two other axes.

In the sphere-tangent algorithm used for the optic flow simulation, a vector $-\hat{j}$, pointing towards the negative y-axis, was forced to a sphere's tangent plane in all of the DPP-microsaccade data interpolation points by

$$\vec{v}_{flow} = \frac{-\hat{j}}{\|\overrightarrow{OP} - \hat{j}\|} \tag{3.5}$$

where $\overrightarrow{OP}$ is the vector from the origin (sphere centre) to a point P on the sphere's surface and $\hat{j}$ is the cartesian unit vector in the direction of the y-axis. After normalising the vectors to unit length, these vectors gave the optic flow field directions at (0°, 0°, 0°) head rotation, assuming that the fly is flying towards the positive y-axis. Optic flow at other fly rotations

was calculated by simply rotating the optic flow along the pitch, yaw and roll axes using a matrix multiplication with the appropriate rotation matrices.

The optic flow field at different head rotations, the rhabdomere orientations, and the DPP microsaccade directions were compared against each other in a three-way comparison. The difference between any two of these unit vector fields, here referred as A and B, was calculated point-wise as

$$e(\vec{v}_A, \vec{v}_B) = \frac{1}{\pi} \arccos\left(\frac{\vec{v}_A \cdot \vec{v}_B}{\|\vec{v}_A\| \|\vec{v}_B\|}\right) \tag{3.6}$$

where $\vec{v}_A$ and $\vec{v}_B$ are vectors located on the same point and the operators $\cdot$ and $\|\|$ denote the inner product and the vector norm (length), respectively. The e error is directly proportional to the angle between the two vectors and its values are limited on the closed interval $[0,1]$. Here $e = 0$ means that the vectors are parallel (no error), $e = 0.5$ means that they are perpendicular (50% error) and $e = 1$ means that the vectors are antiparallel (maximal error). The error fields were plotted using the data visualisation library Matplotlib (Hunter, 2007). Finally, the average mean error between the fields was calculated as the geometric mean of individual vector errors.

The receptive field (RF) fast movement phase was calculated as an inverted DPP microsaccade vector. This procedure was done because the convex lens system inverts the image on the retina, making the receptive fields move in the opposite direction compared to the rhabdomeres. However, as a virtual image (Franceschini, 1972) the DPP is non-inverted and moves in the same direction as the rhabdomeres. Finally, the RF slow-phase was calculated as the inverse of the RF fast-phase. This assumption was needed since the much slower (seconds long) relaxation phase of the DPP microsaccades was not imaged during the experiments.

3.4 Results

3.4.1 GHS-DPP can view DPP across the eyes

To investigate photoreceptor microsaccades across the left and right eyes, I performed GHS-DPP microscopy on wild-type fruit flies. I first established that the GHS-DPP system correctly views the deep pseudopupil (DPP): In perceptual darkness under the antidromic infrared illumination, a *Drosophila*'s head appeared bright against the dark background with the pipette tip being the most luminous object. Then, the microscope's focus was brought from the eye's frontal surface to behind it, revealing the corneal facet lenses on the eye surface and the DPP approximately 200 µm inside the eye (**Figure 3.4**). These imaging results were expected based on the optical DPP theory (Franceschini, 1972), predicting that the properly aligned DPP image forms at the ommatidial axes' convergence point.

Next, the microscope's focus was kept at the DPP, and the fly was rotated using the horizontal or vertical rotation stages (**Figure 3.5A**). It was observed that the DPP follows the stage rotation seamlessly, and the DPP always formed on a position where the eye surface was approximately parallel to the microscope's plane of focus. It was also evident that the DPP's shape changed fundamentally when crossing the borderline of any of the six regions: Right dorsal, right anterior, right frontal, left dorsal, left anterior or left ventral. First, on the dorsal side of the right eye, the DPP appeared as a trapezoidal arrangement of seven bright spots (**Figure 3.5B**). Second, on the anterior part of the eye, on a narrow equator area, the DPP was observed as a convex isosceles trapezoid of nine bright spots (**Figure 3.5C**). Third, on the ventral side the DPP was essentially a mirror image of the dorsal DPP, although often slightly larger (**Figure 3.5D**). The three other regions are similarly located on the left eye since its DPP's mirror of the right eye's respective regions. This equator division to ventral and dorsal hemispheres and the midline superposition DPP are well known in the literature (Beersma et al., 1977)

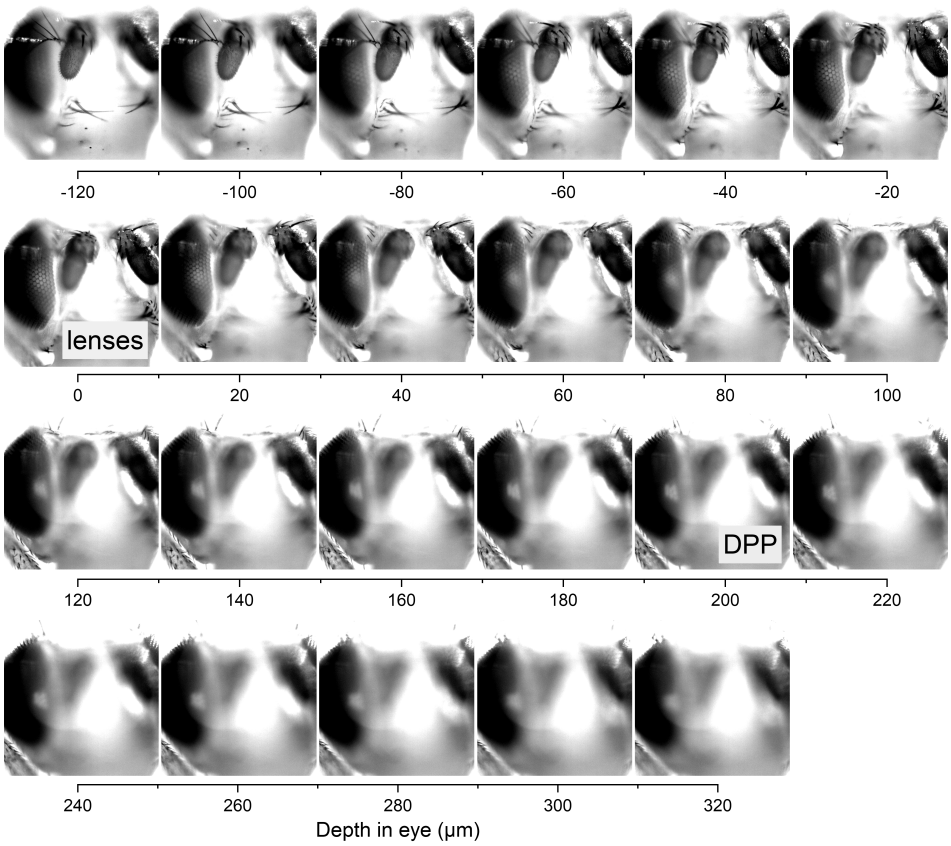

Figure 3.4: A focus sweep of the fly eye under antidromic infrared (IR) illumination. Starting from the antennae (top left), the microscope's focus was moved towards the eye until the facet lenses became clear. Deeper in the eye, the deep pseudopupil (DPP) could be seen as seven bright spots with a diameter of 15 µm. The focus depth axis is approximated from the microscope optomechanical readout. The large faint circular is an artefact due to lens flare.

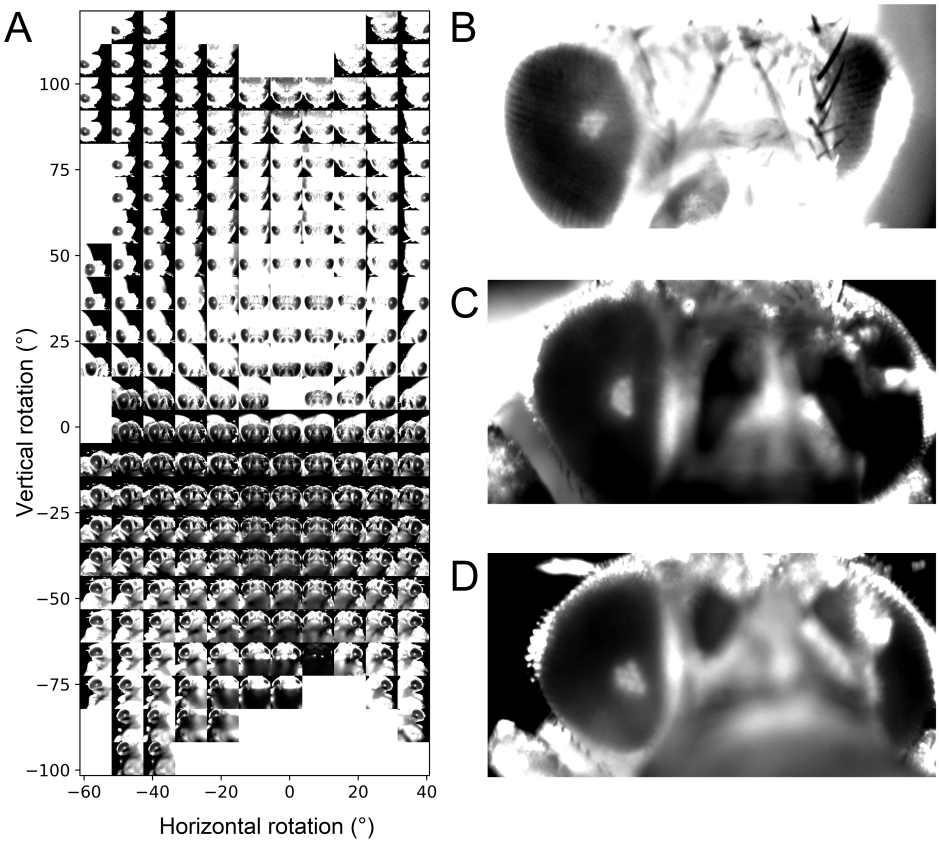

Figure 3.5: Deep pseudopupil (DPP) across the eyes as presented by still images. A) As the fly was rotated, the DPP followed accordingly, continuously without a seam. Per each fly, over 200 rotations (eye locations) were photographed. **B)** The dorsal DPP appeared as seven bright spots with its sharp edge (R3) pointed towards the ocelli. **C)** In the equator, the DPP appeared as nine bright spots, and its long edge (R3 to R3) was parallel with the seam of the eye. **D)** The ventral DPP pattern was a mirror image of the ventral DPP with its sharp edge points towards the fly's mouth parts.

Collectively, these results confirm that the microscope and the used illumination system are sufficient to view the DPP. Likewise, the rotation stage system allows coordinated rotation of the fly. It can operate over a wide range of horizontal and vertical rotations, imaging the eyes fully, except the most lateral regions pointing left and right.

3.4.2 Light flashes induce DPP-microsaccades

I tested how the DPP reacts when a 200 ms bright UV flash is delivered through the microscope. According to the light reversibility principle (known from geometrical optics), the UV flash should activate the same photoreceptors that are viewed as DPP under the infrared illumination. However, wavelength-specific differences between the IR and UV light in refraction, scattering and absorption at various points along the light path make this principle only a useful approximation. Simultaneously to the 200 ms UV flash, the DPP was filmed using the high-speed camera running at 100 fps. The flash expectedly caused the rapid displacement of the DPP (**Figure 3.6A**), repeatably and in nearly all of the tested wild-type flies (13/14). Based on the literature (Hardie & Franze, 2012; Juusola et al., 2017) and the synchrotron X-ray experiments in chapter 2, the light flash likely activated the phototransduction causing the receptors to contract and show fast the side-ways movement of the rhabdomeres. In this study, I refer to these photoreceptor microsaccades as DPP-microsaccades to acknowledge that they are viewed using the DPP. The critical difference between photoreceptor microsaccades and DPP-microsaccades is that the DPP-microsaccades are 10-times larger than the actual displacements of the rhabdomeres because the DPP is a 10-times-magnified image of the rhabdomere tips (Franceschini, 1972).

These DPP-microsaccades were visualised by the pixel-wise division analysis (**Figure 3.6B**). The analysis indicates that the DPP is stationary during the first 30 ms (frame 1 to frame 4). In the next 60 ms (frames 4 to 10), it moves vigorously right-to-left and bottom-to-top. During the final 100 ms (frames 10 to 20), DPP is somewhat stationary. These observations

are confirmed by the cross-correlation based motion analysis (**Figure 3.6C**), showing that the DPP moves mainly between the time points 30 ms and 90 ms (frames 4 to 10).

Interestingly, the motion analysis shows that the DPP motion path was curved or S-shaped: First, the DPP moved towards $+y$, then towards $-x$ and $+y$, and finally, it moved again towards $+y$. Repeated experiments with this fly and the mean responses of the other tested flies (**Figure 3.6E**) show that this was not a one-off but that the curved motion paths were persistent features of the DPP-microsaccades. In fewer cases, the motion path was I-shaped, almost a straight line segment. Interestingly, the motion paths varied considerably between the tested flies and from flash to flash (**Figure 3.6E**).

Next, the kinematics of the DPP-microsaccades were examined in time by placing time on the x-axis and the displacement (instantaneous vector magnitude from the start) or direction (instantaneous vector direction from the start) on the y-axis (**Figure 3.6E** and **D**). The displacement graph (**Figure 3.6E**) show that the DPP-microsaccades approximately followed a sigmoidal activation curve, where a short latency period of 30 ms was followed by a rapid activation phase from 30 ms to 100 ms that saturated after 100 ms. The mean overall displacement was approximately 10 µm, with individual fly means ranging from 5 µm to 15 µm. Since the DPP is a 10-times magnified virtual image of the rhabdomere tips (Franceschini, 1972), these values correspond to 1 µm, 0.5 µm and 1.5 µm physical rhabdomere displacements. Second, the direction graph (**Figure 3.6D**) reflects the curved motion trajectories, showing that the instantaneous direction measured from the DPP start position does not remain constant but first increases (30 ms to 80 ms) and then decreases (70 ms to 200 ms). In early time points of ≤ 30 ms, the DPP is nearly stationary making the direction estimation unreliable, and hence that data are here omitted.

Overall, these kinematics closely match those of the atomic force microscopy (Hardie & Franze, 2012), the corneal neutralisation recordings (Juusola et al., 2017) and the X-ray experiments in chapter 2, indicating that the GHS-DPP system was able to record DPP microsaccades accurately.

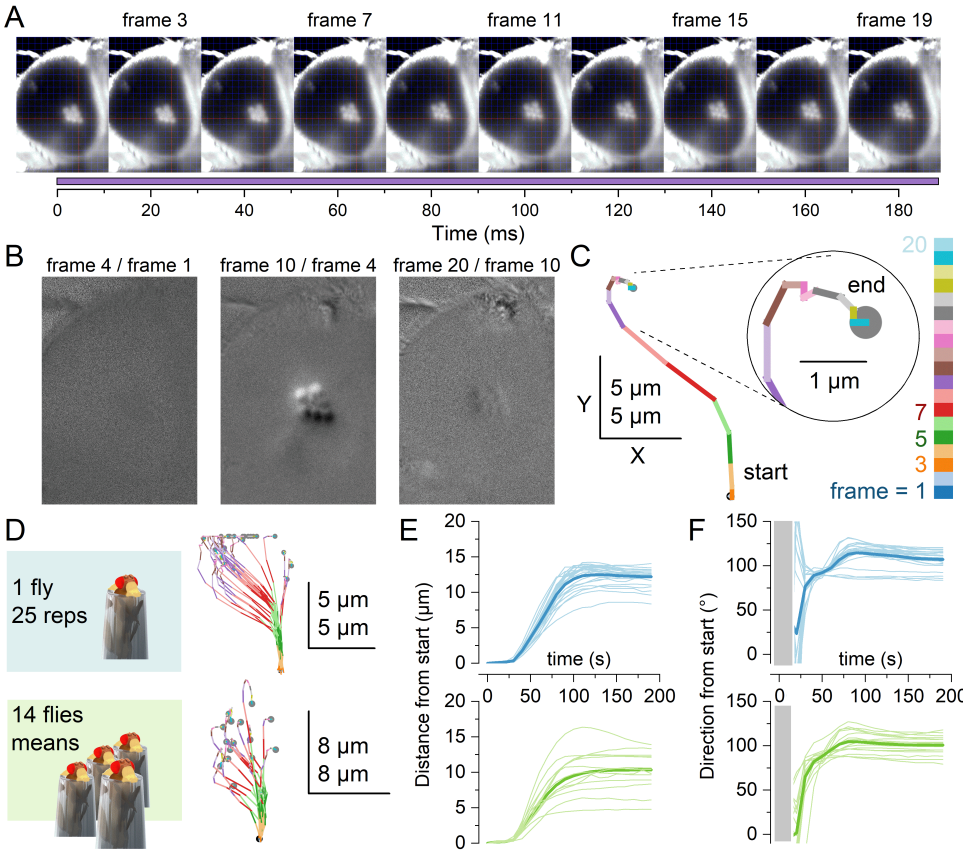

Figure 3.6: Light stimulus induces DPP microsaccades. **A)** An image series (every 2nd image shown) acquired during 200 ms UV flash (purple) reveals the DPP microsaccades (photoreceptor microsaccades). **B)** Pixel-wise division between the 4th and 1st, the 10th and 4th, and the 20th and 10th frames show that most movement occurs between the 10th and 20th frames. **C)** Motion analysis shows the S-shaped motion path of the DPP in the camera image x and y coordinates. **D)** The DPP-microsaccade motion paths of a single fly 25 times repeated (upper), and the mean motion paths of 14 flies (lower) show considerable variability at the individual and population levels. Many motion paths are curved, some almost straight. **E)** Quantified displacement of the DPP (vector magnitude, not distance travelled) over time shows a sigmoidal shape. **F)** Quantified direction of the DPP from the start point to the instantaneous location of the DPP. The rotation is measured from the positive x-axis counterclockwise. Early values ($t \leq 20$) are unreliable and hence here omitted (grey).

3.4.3 DPP-microsaccades are not caused by muscle contraction

The DPP-microsaccades had nearly identical kinematics to those previously described in the literature (Hardie & Franze, 2012; Juusola et al., 2017) and in the X-ray experiments (chapter 2). However, I still wanted to confirm that the DPP-microsaccades were not caused by muscle activation or some photoreceptor independent mechanism by GHS-DPP imaging the microsaccades in hdc^{JK910} and $norpA^{P24}$ flies.

The hdc^{JK910} flies cannot synthesise the neurotransmitter histamine. Hence, there is no synaptic transmission from the photoreceptors to the downstream neurons, making these flies blind irrespective of their functional phototransduction cascade. These hdc^{JK910} files showed near-identical but smaller DPP-microsaccades than the wild-type flies (**Figure 3.7A**, **B** and **D**), indicating that the DPP-microsaccades do not require information transfer from the photoreceptors downstream. These results make it extremely unlikely eye muscle contractions caused the DPP-microsaccades in any flies. However, not all hdc^{JK910} flies responded, possibly reflecting their higher sensitivity to the structural damage inflicted during the preparation (Kemppainen, Scales, et al., 2021). In addition, their smaller response size compared to the wild-type may be explained by their lack of synaptic feedback modulation from the lamina (Dau et al., 2016; Juusola et al., 2017) or by the hdc^{JK910} photoreceptors being physically slightly smaller (Juusola et al., 2017).

I next tested the $norpA^{P24}$ flies, in which unfunctional PLC halts the phototransduction from cleaving PIP_2 from the plasma membrane, thus rendering the flies blind with their photoreceptors unable to contract or activate. The $norpA^{P24}$ flies showed no DPP-microsaccades (**Figure 3.7C** and **D**), indicating that the DPP-microsaccades do require functional PLC. This result makes it extremely unlikely that some photoreceptor independent mechanism caused the DPP-microsaccades.

These control experiments strongly suggest that the DPP microsaccades observed in this study resulted from photomechanical receptor contraction described in the previous studies

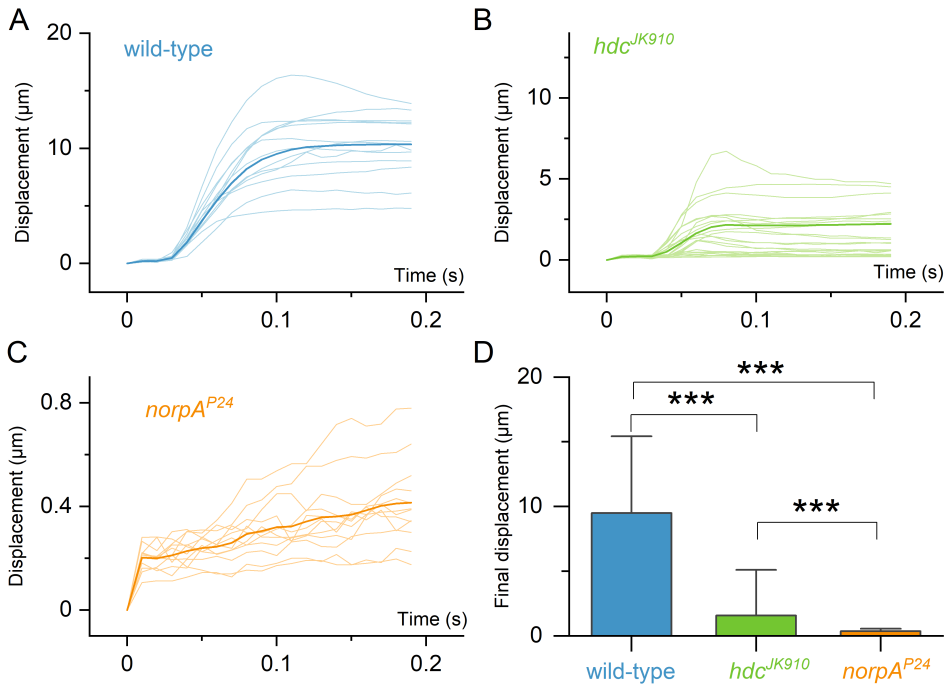

Figure 3.7: DPP-microsaccades are present in *hdc*^{JK910} but not in *norpA*^{P24} **A)** The average displacement responses (instantaneous vector magnitude) in the wild-type flies (N=14 eyes). **B)** The average displacement responses in the *hdc*^{JK910} flies (N=22 eyes) are smaller than in the wild-type, and not all flies or eyes responded. **C)** The *norpA*^{P24} flies do not show any DPP-microsaccades (N=12 eyes). The creep-up is caused by random photon shot noise (1 µm = 1.22 camera detector pixels). **D)** Quantification of the final displacement. T-test, Holm-Sidak adjusted, p-values = $9.2 \cdot 10^{-4}$, $4.4 \cdot 10^{-6}$, $2.3 \cdot 10^{-6}$, from bottom to top.

(Hardie & Franze, 2012; Juusola et al., 2017).

3.4.4 Microsaccades across the eyes are well organised

After successfully recording DPP-microsaccades on a fixed position on the compound eye, I next recorded DPP-microsaccades across the left and right eyes taking advantage of the rotation stage system. The 200 ms UV flash protocol (**Figure 3.8A**) was repeated in approximately 200 distinct locations on the fly eyes by rotating the horizontal and vertical rotation stages in 10° steps. The resulting vertical (from -100° to +120°) and the horizontal range (from -60° to +40°) covered most of the fly eyes, except for their most medial parts pointing left and right.

The DPP-microsaccade direction fields for a single fly and for the population mean (N=5) are presented in **Figure 3.8B** and **C**, respectively. In these two dimensional plots, the grey crosses mark the recording location of the connected vector, and the vector's direction shows the movement direction in the camera image coordinates. These data show that the microsaccades were not randomly directed across the left and right eyes but were well-organized to some pattern (**Figure 3.8C**). This stereotypical directionality was present in all of the tested flies.

In addition, I translated the imaged DPP-microsaccades from the camera image coordinates system to the cartesian 3D coordinate in the fly's frame-of-reference (**Figure 3.8D**). On the dorsal side of the eyes, it appears that the DPP-microsaccades eyes moved towards the contralateral eye, making the very dorsal and medial parts of the eyes a sink point of the DPP-microsaccade field. Interestingly, this dorsal-anterior area seems to best match the back-to-front rhabdomere movement direction described in the literature (Juusola et al., 2017). On the other hand, on the anterior side, near the antennae, the DPP microsaccades had much less lateral-to-medial component, directing the microsaccades more along ventral-to-dorsal axes (**Figure 3.8E**). Thus, the eyes' ventral can be described as a DPP-microsaccade field

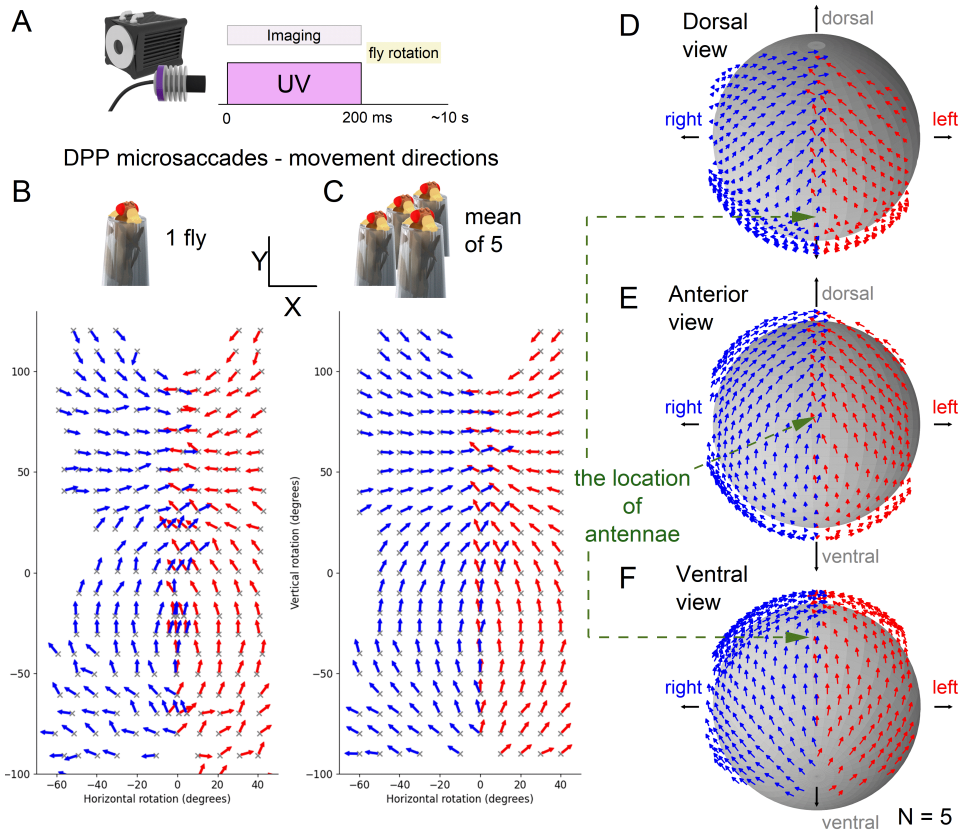

Figure 3.8: DPP-microsaccade movement directions across the left and right eyes. **A)** DPP-microsaccades were recorded during the 200 ms UV flash using a high speed (100 fps) camera. **B)** DPP-microsaccade direction field of a single fly. The grey crosses indicate recording the locations using horizontal and vertical rotations and the arrows point the movement direction in the camera image coordinates (left here is left in the images etc.). **C)** Averaged and interpolated DPP-microsaccade direction field of 5 flies shows a clear, noise-free trend. **D)** On the dorsal side of the head, the DPP moves towards the ocelli. **E)** On the anterior parts of the eye, the DPP moves ventral-to-dorsal, with a small component of lateral-to-medial movement. **F)** On the ventral side, the DPP moves away from the proboscis (fly mouth parts).

source point with DPP-microsaccades moving away from the fly mouth parts during the imaging duration (**Figure 3.8F**).

Overall, these results confirm that the DPP microsaccades are not randomly directed across the left and right eyes but move in an organised manner as described in the literature (Juusola et al., 2017). The trend behind movement directions is best described as a motion from the proboscis (fly mouth parts) towards the ocelli, making the DPP-microsaccade field continuous and borderless across the eyes.

3.4.5 Microsaccades appear tuned to optic flow

Juusola et al. (2017) hypothesised that the photoreceptor microsaccades are aligned according to the optic flow field that a fly experiences during its forward locomotion. This is way, the microsaccades could enhance the resolvability of moving features. When photoreceptors' receptive fields (RFs) move with the features, the photoreceptors would have more time to encode them. Having quantified the DPP-microsaccade directions across the eyes, I wanted to test if the DPP-microsaccades indeed follow the optic flow.

The flow directions depend on the head (pitch, yaw, roll) rotation, concerning the locomotion direction in the fly's frame of reference. First, I simulated the optic flow of a forward flying fly using a typical head rotation as commonly seen in wildlife photographs (pitch = 10°, yaw = 0°, roll = 0°) (**Figure 3.9A**). Here, it can be noted that the point that the fly approaches is the optic flow source point and the point that the fly moves away from is the optic flow sink point. Next, the RF fast-phase was calculated by reverting the DPP-microsaccade direction vectors (**Figure 3.9B**) because the convex facet lenses reverse the image they create. When the rhabdomeres (underneath the lenses) move towards a specific direction, the RF traced light-paths (above the lenses) move in the opposite direction. The slower RF movement phase that occurs during contrast decrements (relaxation from bright to dark) was not imaged here but we have tested elsewhere that the slow-phase moves in the

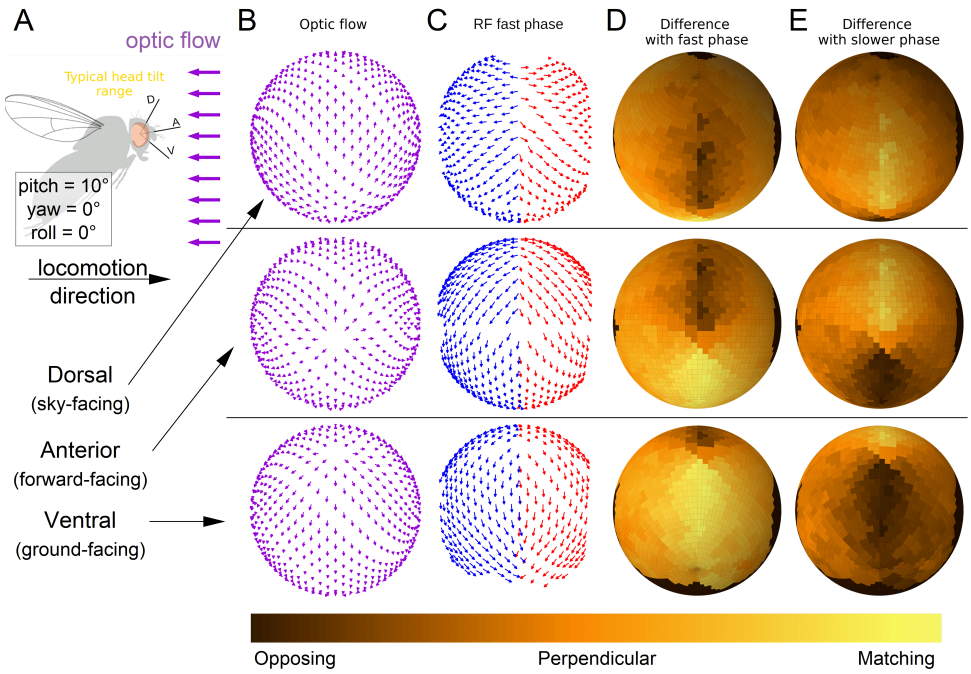

Figure 3.9: The slow and the fast receptive field (RF) movement phases complement each other to match the dorsal (sky facing) and the ventral (ground facing) optic flows. **A)** Illustration of the fly at the estimated (10°, 0°, 0°) flight rotation. **B)** Simulated optic flow at the (10°, 0°, 0°) rotation. **C)** The RF fast-phase that is the opposite of the DPP-microsaccades fast-phase because the lens reverses the directions. **D)** The RF fast-phase aligns well with the ventral (ground) facing side but opposes on the dorsal (sky) side. **E)** The RF slow-phase (DPP-MS fast-phase) aligns well with the optic on the dorsal (sky facing) side but opposes on the ventral (ground facing) side. In the lateral parts the RF movement vectors appear mostly perpendicular to the optic flow.

in the opposite direction than the RF fast-phase. After these calculations, the aligning of the fast and slow RF phases were compared to the optic flow (**Figure 3.9D** and **E**) showing that when the RF fast-phase aligns well with the optic flow, the slow-phase does not, and *vice versa.*

Interestingly, the RF fast-phase aligns well with the ground generated optic flow and the RF slow-phase with the sky generated optic flow. The medial parts, however, are primarily perpendicular with the optic flow. Overall, these results indicate that the dorsal and ventral

parts of the eyes use the different RF phases to improve the resolvability of moving features.

Next, I tested how changing the rotation of the fly while maintaining the locomotion direction (towards the positive y-axis) affects the difference between the RF movement phases and the optic flow. The difference was quantified as the arithmetic mean of all vector errors (**Figure 3.10A**, **C** and **E**). First, the pitch was varied over the whole range (from -180° to +180°) while keeping the other rotations (yaw and roll) at zero (**Figure 3.10A**), showing that in the flight rotation, the RF fast-phase has a lower mean error than the RF slow-phase. Interestingly, neither the fast nor the RF slow movement phases are in their maxima or minima but near the linearly changing mid-error area, where changing pitch changes the mean error strongly. For example, at (-70°, 0°, 0°) fly rotation, the RF fast-phase is nearly perfectly aligned with the optic flow across all the recorded eyes. In contrast, the RF slow-phase is opposing (**Figure 3.10B**).

I also investigated how changing yaw affects the mean error (**Figure 3.10C**). At the flight rotation, the RF fast-phase has a smaller error than the RF slow-phase and it also happens to be in its error minimum, while the RF slow-phase is in its error maximum. Thus yaw has a much smaller effect on the mean error than pitch. However, spatial difference plots reveal that yaw can break the left-right mirror symmetry and change how well the contralateral eyes are aligned with the optic flow (**Figure 3.10D**).

Finally, the roll was varied. (**Figure 3.10E**). Here, the RF fast-phase had a smaller error at the flight rotation, and over the whole range, it had a smaller error than the RF slow-phase. Unlike in the case of yaw, however, the RF fast-phase is in its mean error maximum at the flight rotation. Thus, pitch has only a subtle effect on the spatial difference pattern (**Figure 3.10F**).

Overall, these results show that the RF fast-phase is better aligned with the optic flow at the normal flight position and suggest that the different rotations (pitch, yaw, roll) have distinct roles in shaping the microsaccades' alignment to the optic flow.

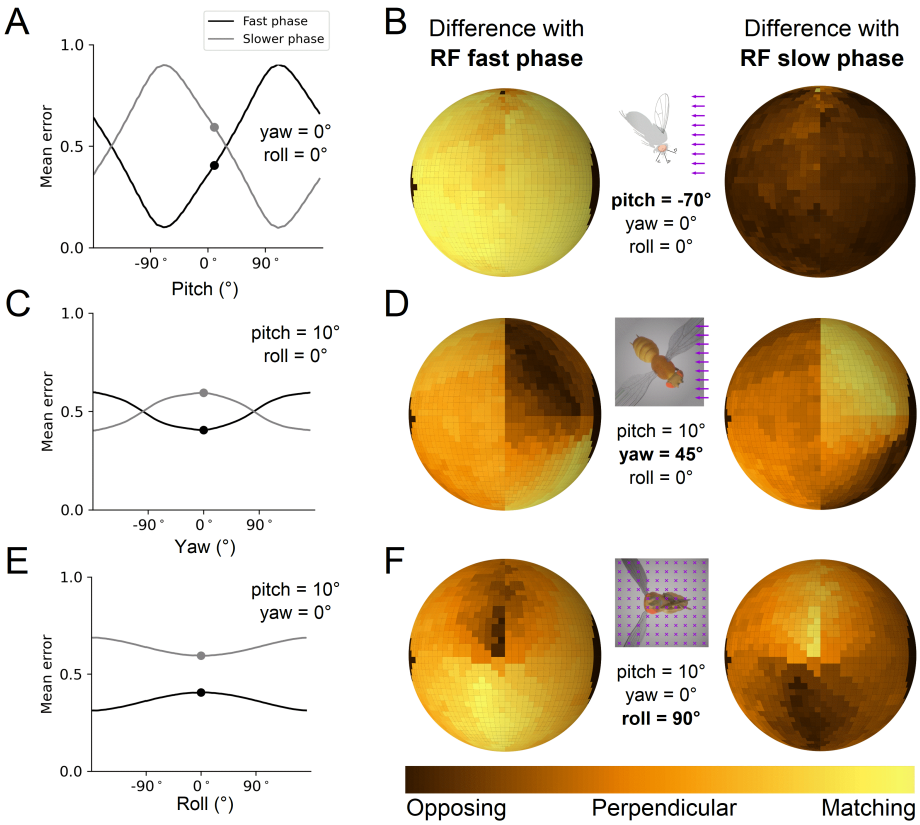

Figure 3.10: The RF fast-phase aligns better with the flight rotation optic flow than the RF-slow phase. **A)** Varying pitch while keeping yaw and roll constant shows that the mean errors (between the RF movement phases and the optic flow) reach their maxima and minima at -80° and 100° pitch. In the estimated flight rotation (10°, 0°, 0°), indicated by the dots, the fast RF phase (black) is better aligned to the optic flow field. **B)** Anterior (top) view on the difference between the optic flow and the RF movement phases at (-70°, 0°, 0°) fly rotation shows that pitch has a profound effect on the mean error. **C)** In the flight rotation, the fast RF movement phase has a local error minimum with respect to yaw and has a smaller overall error than the slow RF phase. **D)** Yaw has a strong effect on the spatial flow difference, breaking the left-right symmetry. **E)** The fast RF movement phase always has a smaller mean error in roll, but the RF slow-phase is in its error minimum. **F)** The roll rotation has only a subtle effect on the spatial flow difference.

3.4.6 Microsaccades follow rhabdomere orientation

In addition to the optic flow, another feature that the DPP-microsaccades could follow is the rhabdomere orientation caused by the trapezoidal R1-R7/8 arrangement pattern in the fly. The rhabdomere orientation is not rotationally symmetric along the ommatidial axis. Conveniently, the DPP data set captures the rhabdomere orientations across the eyes (**Figure 3.5**).

Using the DPP-microsaccades data set, I quantified the rhabdomere orientations across the left and right eyes. This procedure was done by drawing line segments along the rhabdomere pattern's R3-R6 long axis and transforming those segments into the 3D space in the fly's frame-of-reference. This data set is visualised in **Figure 3.11** by drawing these R1-R3 and R3-R5 directions, revealing the concentrically expanding diamond pattern.

Next, I searched for an axis across the rhabdomere pattern that aligns well with the DPP-microsaccades (**Figure 3.12A**) across the whole eye. Here, testing the collinearity was more meaningful since the direction of the selected rhabdomere axis can be chosen freely. For example, the R1-to-R7 and R7-to-R1 axes are equally valid choices. The found minimum-mean-error axis aligned qualitatively almost perfectly with the DPP-microsaccade field (**Figure 3.12B**). This axis was 24.1° rotated from the R3-R6 line, and when specified using the rhabdomeres, is best approximated by the R1-R3 axis or by the R4-R6 axis (**Figure 3.12C**). Using the minimum error axis, the mean error between the fields was approximately 25% (**Figure 3.12D**). The spatial difference plots likewise indicate that this axis matches the flow well and evenly across the eyes except for the eyes' equators (**Figure 3.12E**).

Overall, these results show an axis across the rhabdomere pattern that aligns well with the DPP-microsaccades. This finding indicates that the R1-R7/8 rhabdomere arrangement developmentally sets the microsaccade directions.

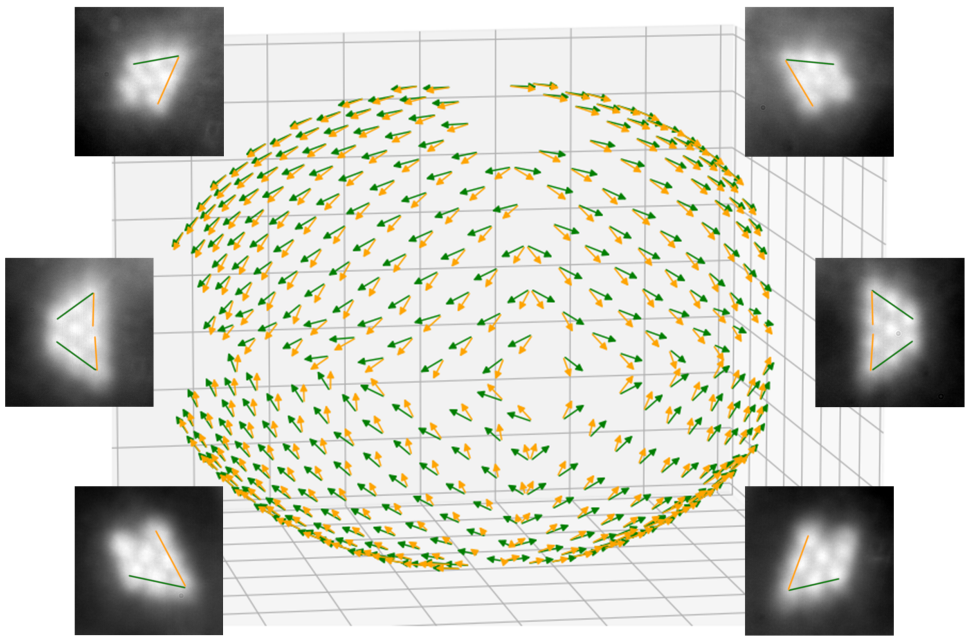

Figure 3.11: Rhabdomere orientations across the eyes, quantified from the DPP images. The green arrows show rhabdomere orientation unit vectors spanned by the R3-to-R5 axis and the orange arrows show the unit vectors spanned by the R3-to-R1 axis. On the dorsal head side (the higher image half), the vectors point away from the ocelli, on the ventral side (the lower image half), away from the proboscis. Wild-type (N=5).

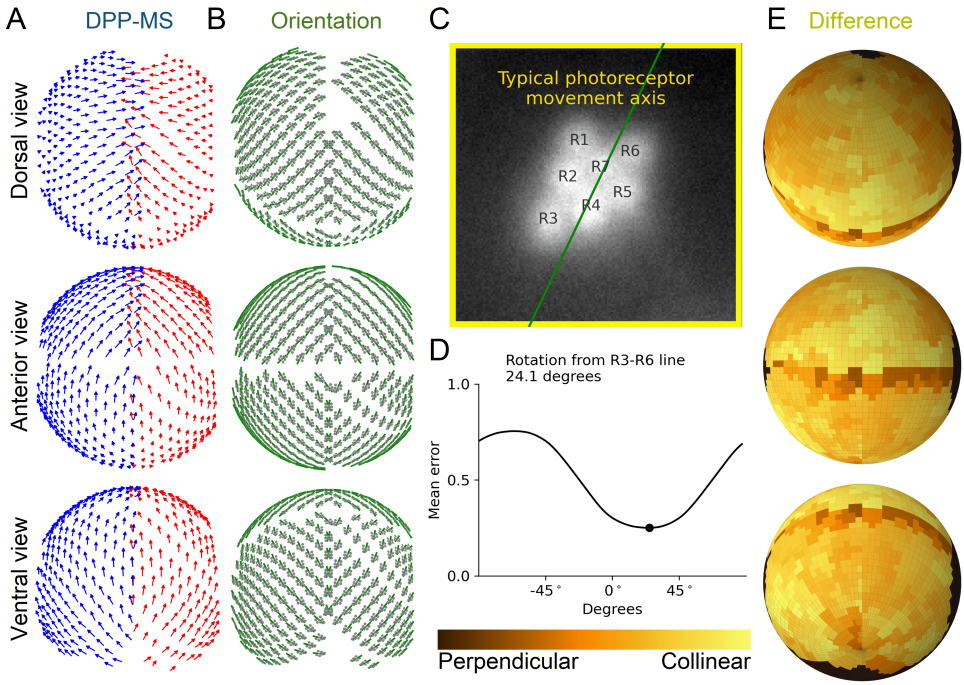

Figure 3.12: DPP-microsaccades occur along the R1-R3 axis. **A)** DPP-microsaccade fast-phase. **B)** Rhabdomere orientation patterns (grey) are plotted with the axis that gives the smallest mean difference with the microsaccade field. **C)** The R1 to R3 axis approximates the smallest error axis most closely (green). Another equally good match is the R4 to R6 axis. **D)** The mean error between the DPP-MS and orientation fields as a function of the selected axis rotation shows that 24.1° rotation from the R3-R6 axis results in the best match. **E)** Difference between the DPP-MS and rhabdomere orientations using the smallest error axis shows that the vectors are mostly collinear with the orientation axes.

3.4.7 Rhabdomeres are aligned to optic flow

So far, my results have provided preliminary evidence that the DPP-microsaccades show a high degree of tuning to the optic flow field and are likely developmentally set by the rhabdomere orientations. To better understand these relationships among DPP-microsaccades, optic flow and rhabdomere orientations, I performed a comparison to test whether the rhabdomeres are oriented according to the optic flow during the forward locomotion (**Figure 3.13A**). Similar to the microsaccades-vs-flow comparison, I calculated the axis across the rhabdomere pattern that minimised the error between the optic flow and the line segment field, drawn across the rhabdomere orientations (**Figure 3.13B**). Using the rhabdomere pattern coordinates, this axis was best described by the line drawn from R2-to-R5 or R1-to-R5 (**Figure 3.13C**) and the mean analysis indicates that this axis was a good match (**Figure 3.13D**). Interestingly, when inspected spatially, a cross-shaped pattern can be seen on the eyes where the vectors are mostly perpendicular (**Figure 3.13E**), which may be caused by the 10° sampling resolution in the vertical rotation.

These results indicate that the optic flow of a forward flying fly well matches the rhabdomere pattern orientation across the left and right eyes, suggesting that the rhabdomeres are oriented according to the optic flow.

3.5 Discussion

The objectives of this study were to record microsaccades across the left and right eyes using the GHS-DPP setup and test whether the microsaccades followed any behaviorally or structurally relevant pattern. These objectives were met, and the study produced important new scientific knowledge about the photomechanical photoreceptor microsaccades. These results are further discussed below.

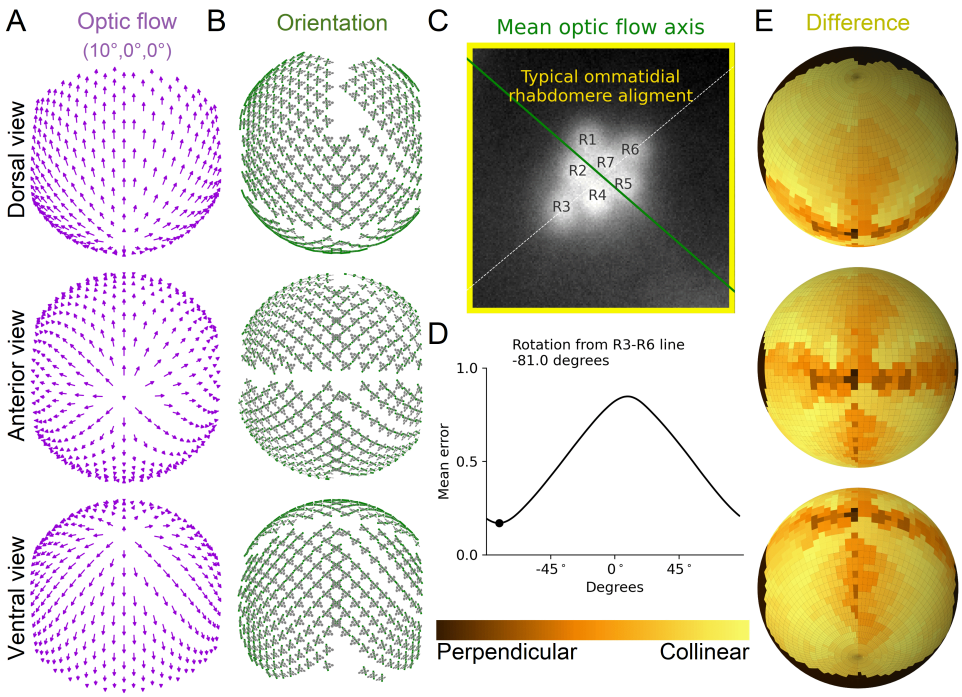

Figure 3.13: Optic flow at the flight rotation follows the R2-R5 axis A) Optic flow at the estimated flight rotation. **B)** Rhabdomere orientation patterns (grey) plotted with the axis that gave the smallest mean difference with the microsaccade field. **C)** The R2 to R5 axis approximates the smallest error axis most closely (green). Another equally good match is the R1 to R5 axis. **D)** The mean error between the optic flow and orientation fields as a function of the selected axis rotation shows that -81.0°rotation from the R3-R6 reference axis yields the best match. **E)** Difference between the optic flow and rhabdomere orientations using the smallest error axis shows that the flow and orientations are well aligned.

3.5.1 DPP-microsaccades and recording techniques

The earlier recordings of the photoreceptor microsaccades were performed using atomic force microscopy (Hardie & Franze, 2012) and the cornea neutralisation technique (Juusola et al., 2017). When photoreceptors were activated by visible light, these recordings show a sigmoidal-like microsaccade activation phase that saturates during the first 100 ms followed by a several seconds long relaxation phase, during which the rhabdomeres return towards the initial starting position.

My deep pseudopupil (DPP) results are consistent with these earlier recordings (**Figure 3.6E**). However, the DPP movement sizes were 10-times larger than the actual rhabdomeric displacement because the DPP is a 10-times magnified virtual image of the rhabdomere tips (Franceschini, 1972). Therefore, these microsaccades are here referred to as DPP-microsaccades to avoid confusion. However, accounting for this 10-time magnification, DPP-microsaccades and microsaccades filmed using the cornea neutralisation method have a similar size of just over 1 μm on average. On the other hand, the *ex vivo* atomic force microscopy recordings (from one dissected eye; Hardie & Franze, 2012) seem to underestimate the lateral (sideways) microsaccade displacement size (being 0.3 μm on average).

One interesting variable that was not taken into account is the gravity's effect on the microsaccades. In the GHS-DPP system, the microscope remains stationary while the fly is rotated. When imaging the ventral eye regions, the fly's antennae point upwards. On the anterior they point towards the horizon and on the dorsal regions they point towards the ground. One piece of anecdotal evidence suggests that that the gravity may have an effect on the microsaccades' directions: In an early prototype, we had the rotation stages rotated 90° (the fly's right eye pointing down and the left eye up), , which created asymmetry between the left and right eye microsaccades. For practical reasons (rigidity) the stages were brought to their current rotation and the finding result from another factors (worse image

quality for example). Some gravitational tuning may be beneficial to the fly if it can adjust the microsaccades to the fly's flight maneuvers. This can be tested in future experiments for example by rotating the microscope instead of the fly.

The GHS-DPP microscopy technique that I set up for this study is well suited for recording microsaccades across the left and right eyes and locally, without rotating the fly. The most significant advantage of using the DPP over the cornea neutralisation technique is the absence of the immersion fluid between the fly eye and the microscope objective, making it impractical to reorient the fly. In addition, the lack of objective fluid makes it possible to use illumination sources further in the infrared spectrum due to reduced absorption, diminishing any illumination causing phototransduction activation. In my opinion, future development efforts are best directed on making the setup smaller and more affordable by using additive manufacturing techniques such as 3D printing or inexpensive consumer-grade electronics for the lightning or the camera. This development would allow vastly parallel data acquisition making the technique ideal for screening any mutations affecting the microsaccades.

3.5.2 DPP motion paths and modulation

In closer inspection, the local DPP-microsaccade motion paths appeared to have a distinctive S-shaped pattern (**Figure 3.6D**). To my knowledge, this has not been previously reported in the literature.

Interestingly, some of the flies had more I-shaped than S-shaped motion paths, and this variability was also seen between the repeated stimulation of one fly (**Figure 3.6D**). Such variability in microsaccades' size and phase (**Figure 3.6D** and **E**) supports a theory where synaptic feedback signals to photoreceptors from deeper regions in the brain modulate the microsaccades; for example, by lamina feedback regulation (Dau et al., 2016). This hypothesis is (at least) partially supported by the hdc^{JK910} flies' smaller DPP-MS responses

(**Figure 3.7B** and **D**). The mechanism would likely have to somehow affect the PIP_2 cleavage during the phototransduction or alter the plasma membrane's or the surrounding retinal tissue's mechanical properties. Yet another possibility is mechanical feedback through the eye muscles that exert forces on the retinal tissue (Hengstenberg, 1972). This suggestion seems reasonable, since all of the tested flies, including the blind $norpA^{P24}$ flies, had a noticeable and apparently random shift of the DPP during the ISI period, presumably due to eye muscle activity. The muscle exerted forces on the tissue could then suppress or enlarge the microsaccades. To test this hypothesis, future studies can use electronic or optogenetic eye motoneurone (muscle) activation to test whether the activity state of the eye muscles also affects the microsaccades.

3.5.3 Microsaccades and optic flow

Juusola et al. (2017) hypothesised that the photoreceptor microsaccades follow the optic flow, giving fly photoreceptors more time to encode moving features as their receptive fields (RFs) follow them. However, this hypothesis is complicated because the microsaccades, and therefore RFs, have a fast activation phase and a seconds-long relaxation phase (Juusola et al., 2017). At the estimated flight rotation, my results revealed that the RF fast-phase was better aligned with the optic flow experienced by ground-facing receptors (**Figure 3.9D**). The RF slow-phase was better aligned with the optic flow experience sky-facing receptors (**Figure 3.9E**). This finding was expected because the optic flow experienced by the ground-facing receptors can reach very high velocities.

In contrast, the sky-facing receptors experience optic flow from features far away, such as clouds or tree branches, creating slower velocities. Such realisations reveal a limitation of the optic flow analysis, as the optic flow velocities were not accounted for in the present study. Future studies can simulate optic flow velocities created by naturalistic environments and compare these to the calculated RF phase velocities across the eyes for more profound

insight.

Perturbations from the estimated flight rotation showed that, in general, the RF fast-phase appears to match the optic flow better (**Figure 3.10A**, **C** and **E**). Still, nearly a perfect match with the RF fast-phase can be obtained by rotating the fly at -70° pitch (**Figure 3.10B**). The latter suggests that the RF fast-phase is not optimally aligned to the optic flow at the flight rotation, meaning that the microsaccades would not follow the optic flow. However, it may be that the previously discussed ground-facing and sky-facing labour division between the RF fast and slow phases is more important to the fly than fully optimising only one of the components.

My results also showed that the pitch, yaw and roll rotations affect the alignment between the RF phases in different ways. For example, the pitch has the largest effect on the mean error (**Figure 3.10B**), yaw breaks the left-right symmetry (**Figure 3.10D**), and roll changes the spatial difference only slightly (**Figure 3.10F**). However, the analysis here is oversimplified. With the three independent rotation variables, the optimisation space is actually 3-dimensional. Therefore, it can not be fully explored by varying the rotation variables from the flight rotation alone. Instead, all possible (pitch, yaw, roll) rotation combinations would have to be tested one-by-one to find the true global error minimum between the RF phases and the optic flow and to characterise the role of each rotation thoroughly.

3.5.4 Mechanisms behind the microsaccades

Photoreceptor contractions are caused by PIP_2 cleavage from the microvillar plasma membrane during the phototransduction cascade (Hardie & Franze, 2012). However, it is unknown how these photomechanical receptor contractions are translated into the coordinated movement towards a specific direction. Meaning, it is not apparent how the previously reported back-to-front photoreceptor movement directions (Juusola et al.,

2017) or the DPP-microsaccade directions across the eyes (**Figure 3.8**) arise. Dissociated ommatidia also show bending along their long axis (Juusola et al., 2017), but it is unclear if this can solely lead to the observed motion directions.

I quantified the rhabdomere orientations (**Figure 3.11**) using the DPP-microsaccade data set. To my knowledge, this is the first time when the rhabdomere orientations have been reported to this extent, although the general structure is well known (Beersma et al., 1977) and other systems have been built before that would have been capable of achieving the same (for example, Arias et al., 2021; Douglass & Wehling, 2016). For the first time, I showed that microsaccades across the eyes mostly occur along the R1-R3 axis to the degree that can predict the DPP-microsaccade directions (**Figure 3.12**). This correlation suggests that the rhabdomere orientations may developmentally set the microsaccade directions to move mainly along the R1-R3 axis. This hypothesis is promising and could be tested by altering or randomising the rhabdomere orientations by *Drosophila* genetics recording whether the microsaccades are affected accordingly.

4 Local DPP-microsaccade recordings

4.1 Introduction

The global DPP-microsaccade experiments in chapter 3 revealed how the photoreceptor microsaccades are directed across the left and right eyes. However, three important features of the microsaccades remained unexplored: First, how much the individual R1-R8 rhabdomeres contribute towards the microsaccades. Second, how the immobilisation affects the microsaccades. Third, how large microsaccades the sinusoidal stimuli evoke in light adapted photoreceptors. In the following paragraphs, I explore these questions and briefly explain why they are important.

Hypothesis 1: All the R1-R8 rhabdomeres contribute towards the microsaccades. The cornea neutralisation (Juusola et al., 2017) and the GHS-DPP recordings (**Chapter 3**) show that the rhabdomeres inside an ommatidium move as a unit, maintaining their trapezoidal R1-R7/8 arrangement. However, it is unknown whether all the R1-R8 rhabdomeres contribute equally towards the microsaccades. Since the photoreceptor contractions are likely caused by the PIP_2 cleavage from the microvillar plasma membrane (Hardie & Franze, 2012), it seems plausible that the outer R1-R6 rhabdomeres with more microvilli (Juusola et al., 2017) may contribute more towards the microsaccades than the inner R7-R8 rhabdomeres with fewer microvilli. Similarly, the R1-R6 rhabdomeres outnumber the R7-R8 rhabdomeres in a 3-to-1 ratio. In *Drosophila*, genetic tools on the blind $norpA^{36}$ flies allow selective rescuing of with rhodopsin-specific photoreceptors, making it possible to stimulate a selected subset of the receptors alone. I tested DPP-microsaccades in these $norpA^{36}$ rescues to green and UV flight flashes while recording their ERG responses. Overall,

my results support the hypothesis, suggesting that all the R1-R8 rhabdomeres contribute towards the microsaccades. The R1-R6 typically contribute the most, but this depends on the used stimulation wavelength.

Hypothesis 2: Immobilisation method affects the microsaccades. For all previously presented GHS-DPP experiments in this thesis, the flies were prepared using the pipette tip immobilisation technique, in which the beeswax-immobilised head protrudes from the plastic pipette tip. However, this immobilisation could have a restricting or passivating effect on the fly. Thus, we hypothesised that the copper-hook tethering technique, restricting the fly less, may lead to altered microsaccades, possibly via the hypothetical contraction feedback modulation from the brain, as discussed in chapter 3. To test this hypothesis, I recorded DPP-microsaccades and ERG-responses to UV and green light flashes in wild-type and R1-R6 defect-flies using both immobilisation techniques. The results suggest that the immobilisation techniques are generally interchangeable, somewhat rebutting the initial hypothesis.

Hypothesis 3: Grating stimuli with behaviourally relevant frequencies causes observable microsaccades. In previous studies (Hardie & Franze, 2012; Juusola et al., 2017) and this thesis (**Chapters 2** and **3**), the photoreceptor microsaccades have been mainly studied using the flash stimulus, often in dark adapted photoreceptors. The flash stimulus has the benefits of causing larger displacements making the movement analysis more reliable and the videos visually apparent. In nature however, the receptors experience stimuli that, at the reduced viewpoint, are mathematically representable as the sum of sinusoids (**Equation 1.1**). Therefore, to investigate photoreceptor microsaccades to more naturalistic dynamics stimuli I recorded DPP-microsaccades in light-adapted wild-type eyes to sinusoidal sweep stimuli and its two variations. The results show that the photoreceptor microsaccades can follow temporal changes up to 30 Hz with 13 Hz cut-off (3 dB) frequency, strongly indicating that photoreceptor microsaccades are relevant outside the laboratory settings.

4.2 Methods

4.2.1 Fly stocks

In this study, wild-type (Berlin) flies and visual mutants with selectively functional R1-R8 receptors were tested. First, in the *norpA*^{36} rhodopsin-specific rescue flies, the PLC enzyme has been rescued using a P-element plus cDNA technique (Wang et al., 2008; Wardill et al., 2012). Rh1-*norpA*^{36} had only the outer R1-R6 photoreceptors functional. Rh3-*norpA*^{36} and Rh4-*norpA*^{36} had only 30% and 70% of the R7 receptors functional, respectively. And, Rh5-*norpA*^{36} and Rh6-*norpA*^{36} had only 30% and 70% of the R8 receptors functional, respectively. These ratios reflect the stochastic distribution of the pale (containing Rh3 and Rh5) and yellow (containing Rh4 and Rh6) receptors (Wernet et al., 2006). The Rh3-6-*norpA*^{36} rescue flies (`CS,norpA;Rh3-norpA/Rh5,Rh6-norpA;Rh4-norpA/+`), in which all the R7-R8 receptors were functional, were created by crossing `CS,norpA;Rh5,Rh6-norpA/CyO;+/Tm2` with `CS,norpA;Rh3-norpA;Rh4-norpA`. Second, in the *ninaE*^{8} flies (ninaEP334), the mutated Rh1 (*ninaE*) nearly completely abolishes the Rh1 expression (Washburn & O'Tousa, 1989), rendering the outer R1-R6 receptors unfunctional.

These visual mutants and transgenic flies are summarised in Table 4.1. They were maintained in an incubator set at 25°C under a 12:12h light-dark cycle and fed with standard brown (molasses) fly food (Table 2.1).

4.2.2 Fly preparation techniques

Most flies were prepared using the pipette tip preparation technique presented in chapter 3 (**Figure 3.1**). Shortly, the flies were pushed halfway through a plastic pipette tip's small

Table 4.1: Flies used in the local DPP-MS recordings

Genotype	**Alteration outcome**
Berlin wild-type	(no alteration)
norpA^{36}	R1-R8 unfunctional
Rh1-*norpA*^{36} rescue	All R1-R6 rescued
Rh3-*norpA*^{36} rescue	30% of R7 rescued
Rh4-*norpA*^{36} rescue	70% of R7 rescued
Rh5-*norpA*^{36} rescue	30% of R8 rescued
Rh6-*norpA*^{36} rescue	70% of R8 rescued
ninaE^{8}	Abolished Rh1 expression, only R7-R8 functional
Rh3-6-*norpA*^{36} rescue	Rhodopsins 3,4,5 and 6 rescued, all R7-R8 functional

opening by puffing air using a hand-held syringe. Then the fly was immobilised using melted beeswax, keeping the fly's head and a small part of the upper thorax sticking out the pipette tip. Finally, the preparation was inserted in the GHS-DPP system.

In this study, the copper-hook tethering technique was used as an alternative technique to test **Hypothesis 2** and see whether the preparation technique affected the microsaccades. In the copper-hook preparation (performed by Ben Scales, a fellow PGR), the ice-cooled fly was first placed on a Peltier-element-cooled aluminium plate with a small fly sized cavity in it. Next, a small copper-wire hook was attached to the fly's dorsal thorax, near the neck, using UV-cured glue. Notably, the head was also glued on the body to remain immobile during the DPP-MS recordings. Finally, the prepared fly was inserted in the GHS-DPP setup for experiments.

4.2.3 GHS-DPP microscopy

Details of the GHS-DPP system and its operation are given in chapter 3. Here, the local DPP-microsaccade recordings are explained in detail.

In the local recordings, to avoid variability arising from many recording locations, only one fixed location per eye was recorded. At ±28° horizontal and -37° vertical rotation. Here, the eye was nearly ideally back-illuminated by the upper infrared LED. At this position, the observed eye view was not obstructed by the pipette tip, beeswax or the fly body, allowing the DPP to be fully visible as seven bright spots in the trapezoidal arrangement. In addition, this recording location possibly had behavioural importance because its photoreceptors face approximately forwards and towards the ground during the normal forward flight and may participate in visually-guided object interactions.

The UV or green light stimulus LED was flashed through the microscope for 200 ms at the recording location while simultaneously acquiring images with the high-speed camera running at 100 fps. After each flash, an inter-stimulus-interval (ISI) of 2 to 10 s was given for the receptors to recover. This flash protocol was repeated 25 times for additional statistics about the microsaccades' variability. Then the same was performed using the other LED before recording the contralateral eye.

The sinusoidal stimulus recordings were performed similarly to the local flash recordings, but i) a longer (30 s) ISI was used to save the acquired images on the hard drive and ii) the camera was set to run at 200 fps to fulfill the Nyquist-Shannon sampling theorem (f_1 = 100 Hz, see below). In addition, the stimulus LED was set to mid-intensity during the ISI to not to dark-adapt the receptors. All three sinusoidal stimuli were 10 s long. In the sinusoidal sweep stimuli, the frequency changed logarithmicly over time, (`scipy.signal.chirp`), following the expression

$$f(t) = f_0 \left(\frac{f_1}{f_0} \right)^{t/t_1} \tag{4.1}$$

Here, f_0 and f_1 are the frequencies at $t = 0$ and $t = t_1$, t_1 is the stimulus length, and t is any arbitrary time point between 0 and t_1. In this study, $t_1 = 10$ s, $f_0 = 0.5$ Hz and $f_1 = 100$ Hz. The square wave sweep was two level (one bit) quantized variation of this sinusoidal sweep stimulus. Finally, the constant-frequency step stimuli consisted of 100 ms positive and negative contrast increments and decrements. It was created from a constant sinusoidal signal that was three level quantized.

The template matching based cross-correlation motion analysis and its details are presented in chapter 3.2.4. The local recordings however have an additional step that is worth pointing out: The DPP's position at the beginning of each repeat was defined as zero. This zeroing hides the DPP displacement that can occur during the ISI period, for example by the micromanipulators' drift or by the eye muscle. The imaging period was short (200 ms), and therefore, the DPP-recordings contained little or no motion caused by sources unrelated to the photoreceptor contractions, as these sources work over longer time periods.

4.2.4 Subsequent ERG-recordings

After recording the DPP microsaccades, the eye's physiological state was assessed by electroretinogram (ERG) recordings that measure the activation of many photoreceptors and visual interneurons.

In the ERG recording setup, the fly rested on a metallic central pole inside a metallic cubicle acting as a Faraday cage. A green (546 nm) or ultraviolet (365 nm) LED (OptoLED, Cairn Research, UK) provided light stimuli. The LED heads were connected to their power supply (Dual OptoLED Power Supply, Cairn Research, UK) through a custom made multiplexing unit. The power supply was controlled over the BNC interface. The LED holders contained

a convex lens and by adjusting the LED-to-lens distance, the LED light was focussed into an optic waveguide. The waveguide entered into the recording cubicle, a Cardan-arm system controlled the positioning of its light end. The Cardan arm system was adjusted so that the light always pointed directly at the recorded eye.

A single-electrode amplifier (SEC-10LX, npi Electronic, Germany) was used with ringer-filled glass electrodes to record ERG responses. The ringer solution contained 120 mM NaCl, 5 mM KCl, 10 mM TES ($C_6H_{15}NO_6S$), 1.5 mM $CaCl_2$, 4 mM $MgCl_2$ and 30 mM sucrose (Juusola et al., 2016). The ERG measurement computer had a data acquisition system for analogue-to-digital input (PCI-6713 with BNC-2090, National Instruments, USA) and digital-to-analogue output (PCI-MIO-16E-4, National Instruments, USA; with custom BNC-block). The acquisition was controlled by the *Biosyst* software (Juusola & Hardie, 2001) running in the MATLAB computing environment (MATLAB 7.0.4, Mathworks, USA) on the Windows platform (Windows 2000 Professional, Microsoft, USA). The amplifier signal was low-pass filtered to 500 Hz before it was sampled at 1 kHz.

The recording electrodes were fabricated similar to the beamline ERG-electrodes presented in chapter 2. In brief, fire polished borosilicate glass tubes (OD = 1 mm, ID = 0.5 mm, length = 75 mm) with an inner filament were inserted into a laser micropipette puller (P-2000, Sutter Instruments, USA) to produce short-tip low-resistance microelectrodes. The electrodes were back-filled with a fly ringer solution and then inserted to polycarbonate electrode holders with chlorinated silver wire. The electrode holders were then connected into female BNC connectors attached to the amplifier headstage.

The fly was transported from the GHS-DPP setup to the ERG-recording setup located in the same room and attached to top of the central pole. The fly was viewed with a stereo microscope (Nikon SM2645 with C-W30X/7 oculars, Nikon, Japan) under a cold light source (Photonic PL 1000, Photonic Optics, Austria). It was rotated so that either its left or right eye faced towards the measurement electrode. Then, the reference and the recording electrodes were brought in touch with the fly torso and eye, respectively, using

their micromanipulators. Next, the amplifier was turned on to provide auditory feedback, informing when the electrodes were connected and the electric circuit closed. Finally, the microscope light source was turned off, and ERG responses to flash stimuli were confirmed.

In the recording protocol, first the UV LED was flashed for 1 s once, and then a mean response to 25 flashes of the UV LED was recorded. The mean response recordings allowed detecting changes in the weakly responding mutants (for example, Rh4-$norpA^{36}$ rescue), in which the ERG-sizes approached the input card's quantisation level. Immediately after this, the green LED was inserted, and I recorded the mean response to 25 green flashes and then a response to one green flash. Next, the microscope lights were turned back on, the electrodes backed off, the fly was rotated, the electrodes were brought back in, the microscope lights were turned off, and the measurement protocol was repeated on the contralateral eye. In some flies, the green and UV stimulation order was reversed, but it did not have an observable effect on the ERGs.

4.3 Statistical methods

Statistical hypothesis testing was used to test whether the response amplitudes (DPP-microsaccades and ERG recordings) between any two fly groups had statistically different means from each other. The tests were performed using the *scipy* (v1.73) and *statsmodels* (v0.13.1) Python libraries.

First, a normality test (`scipy.stats.normaltest`) was used to test whether a group followed a normal distribution with α = 0.05 significance level. If both groups we normally distributed, two-sided Welch's t-test (`scipy.stats.ttest_ind`) was used. Welch's t-test was selected because it is more robust under unequal variances and sample sizes than the widely used Student's t-test (West, 2021). If one or both groups significantly deviated from a normal distribution, the Mann-Whitney U-test

(`scipy.stats.mannwhitneyu`) was used instead. Finally, the p-values were Holm-Šidák adjusted (`statsmodels.stats.multitest.multipletests`) to control the family-wise error rate that is the probability of making type I errors (false positives). This adjustment for multiple comparisons was performed independently for each statistics table.

4.4 Results

4.4.1 Each rhabdomere contributes to microsaccades

To test **Hypothesis 1** and investigate how the different R1-R8 receptors contribute towards the microsaccades, I recorded DPP-microsaccades in wild-type and rhodopsin-rescued blind flies to 200 ms UV and green flashes. I also recorded the eyes' ERG-responses to correlate their electrical activity with the DPP-microsaccades and confirm that flies were not contaminated.

First, I tested wild-type flies, *ninaE*^{8} and Rh3-6-*norpA*^{36} rescue flies (R7-R8 flies) with unfunctional R1-R6 receptors (**Figure 4.1A**). The DPP-microsaccades were larger in wild-type than in R7-R8 flies (**Figure 4.1B**), indicating that the R1-R6 receptors contributed more towards the DPP-microsaccades than the R7-R8 alone. Furthermore, the ERG-responses were consistent with the flies' spectral sensitivities and movement responses (**Figure 4.1B**) and demonstrated a correlation between the DPP-microsaccades and the photoreceptors' electrical activation. Notably, none of the R7-R8 files showed the ERG on- or off-transients because the transients are caused by the lamina interneuron activity (Belusic, 2011; Coombe, 1986) and the R7-R8 bypass the lamina synapsing directly to the medulla (Cutforth & Gaul, 1997).

To quantify the DPP-MS contributions of the R1-R6 and the R7 and R8 receptors, I next tested rhodopsin-specific *norpA*^{36} rescue flies using the UV, green and no-flash stimuli

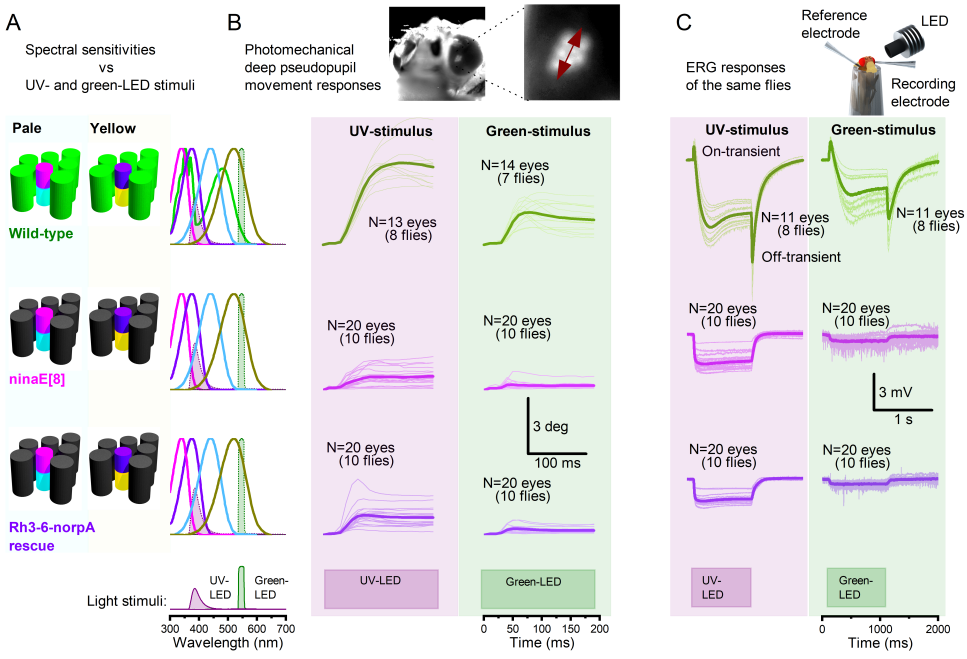

Figure 4.1: The R1-R6 receptors contribute more than the R7-R8. A) Normalised spectral sensitivity profiles in the wild-type, *ninaE*^{8} and Rh3-6-*norpA*^{36} rescue overlap with the used UV and green light stimuli. **B)** The flies' DPP movement responses to UV and green stimuli show that having no functional R1-R6 receptors leads to smaller DPP-microsaccades. **C)** The lack of on- and off-transients in the *ninaE*^{8} and Rh3-6-*norpA*^{36} rescue flies confirm that their outer R1-R6 receptors are unfunctional.

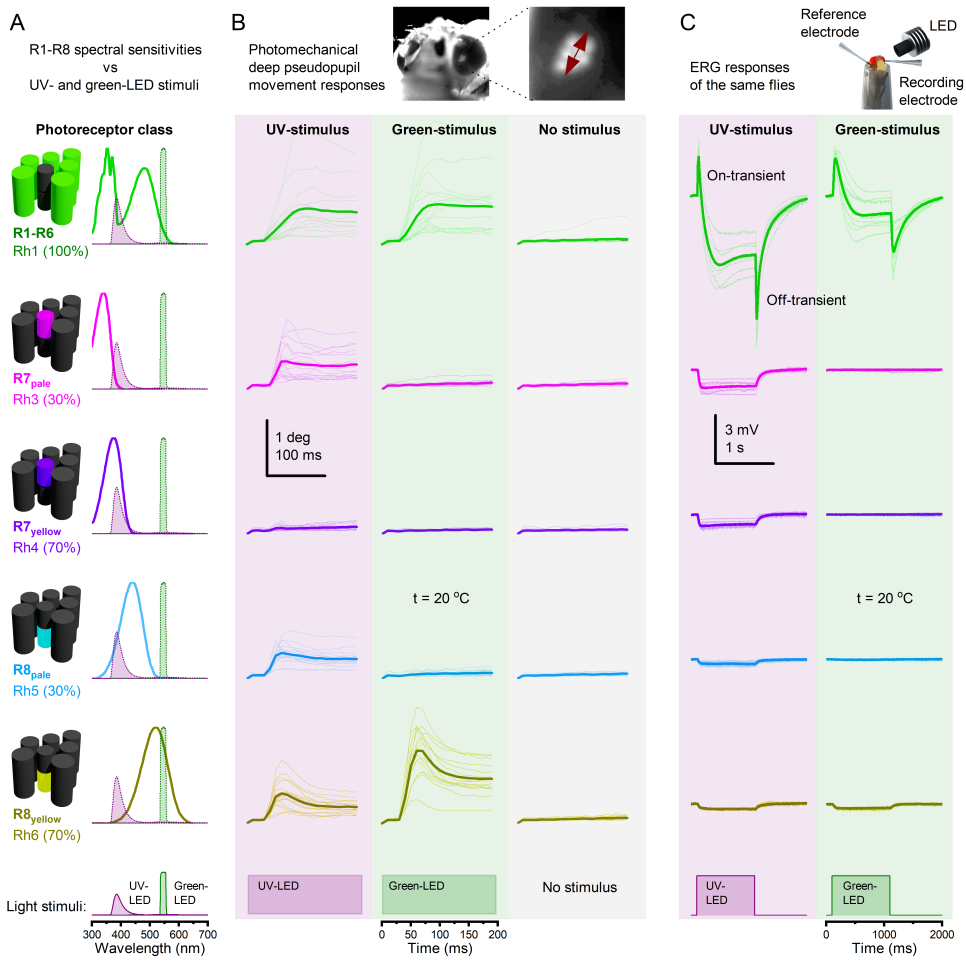

Figure 4.2: Rh-norpA rescues reveal the R1-R8 receptors' contributions in DPP-microsaccades. **A)** Spectral sensitivities in the tested *norpA*^{36} rescues and stimulus LEDs' spectral profiles. Here, the 30/70 ratios reflect the stochastic distribution of the pale (containing Rh3 and Rh5) and yellow (containing Rh4 and Rh6) receptors. **B)** The flies' DPP-microsaccades to UV flashes (left), green (middle) and no stimulus (right) quite closely follow their spectral sensitivities. Only the Rh4-*norpA*^{36} rescue shows smaller responses to UV flashes than expected. **C)** The subsequent ERG-recordings correlate the movement responses to the photoreceptor's electrical activation and confirm the flies' spectral sensitivities (no contamination).

(**Figure 4.2A**). In these flies, the DPP-microsaccades generally followed the flies' spectral sensitivity profiles and the stimulus's wavelength (**Figure 4.2B**), suggesting that all the R1-R6 and the R7-R8 rhabdomeres contribute towards the microsaccades. However, the Rh4-*norpA*^{36} rescue deviated from this rule showing only minute DPP-MS responses to the UV flashes (**Figure 4.2C**) that may result from the flies' carotenoid-deprived diet (Table 2.1), which makes the $R7_{yellow}$ a blue receptor (Hardie, 1985). However, the UV flashes evoked notable ERG-responses suggesting that the $R7_{yellow}$ were activated by the UV light (**Figure 4.2C**). Finally, interestingly, the Rh6-*norpA*^{36} rescue flies showed larger responses to the green stimulus than the Rh1-*norpA*^{36} rescue , but not to the UV stimulus. This result can be explained by the rhodopsin-6's higher sensitivity to the green LED used, or alternatively, by its higher phototransduction gain as it is located behind and screened by the $R7_{yellow}$ (Hardie, 1985).

All-around comparisons and statistics are presented in **Appendix 1**.

These results have been summarised in (**Figure 4.3**), showing a statistical comparison to the wild-type. The results show that all the tested R1-R8 rhabdomere configurations generate photomechanical photoreceptor microsaccades, supporting **Hypothesis 1**. In addition, the results indicate that the R1-R6 rhabdomeres contribute in general more towards the microsaccades than the R7-R8 rhabdomeres but this also depends on the stimulus's wavelength composition.

4.4.2 Preparation technique does not affect the microsaccades

To test **Hypothesis 2** and see whether my previous experiments were preparation-technique biased, I recorded DPP-microsaccades and ERG-responses to UV and green light flashes in wild-type and R1-R6 defect-flies (*ninaE*^{8} and Rh3-6-*norpA*^{36} rescue) using the pipette tip and the copper hook preparation techniques (**Figure 4.4A**).

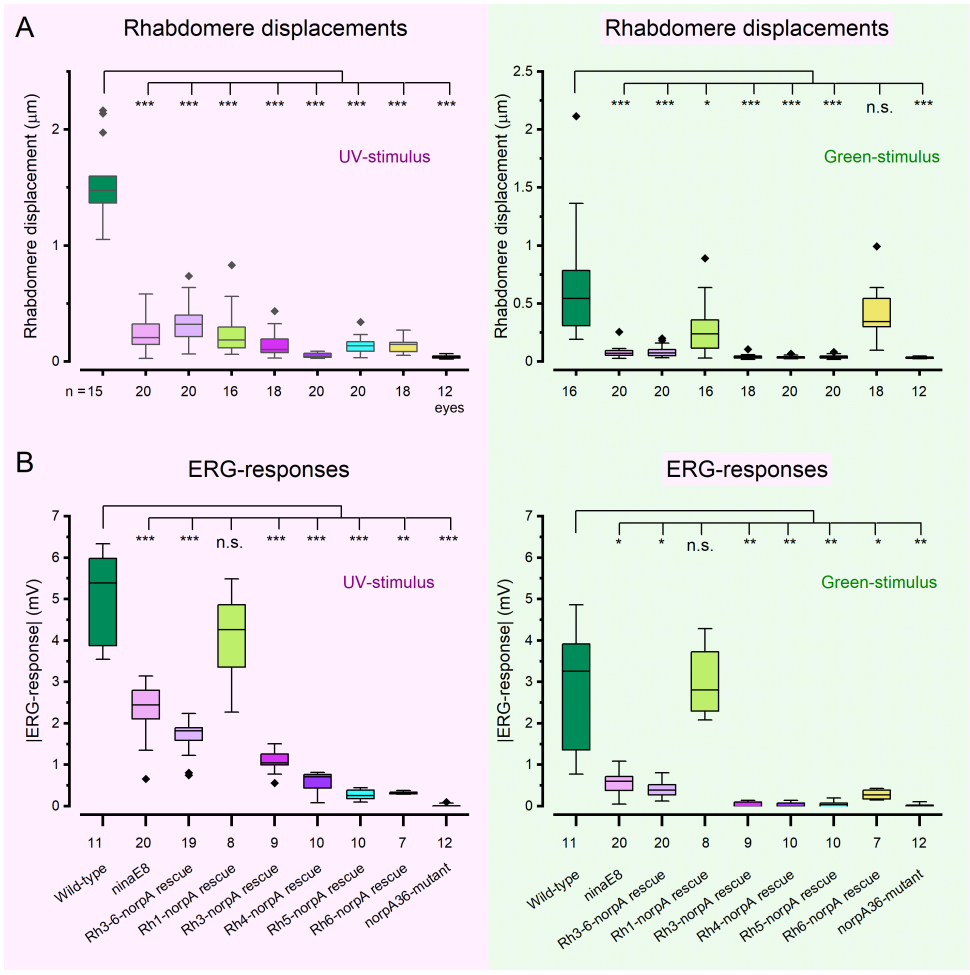

Figure 4.3: Statistical analysis of the Rh-rescues' DPP-microsaccades. **A)** DPP-microsaccades' displacement sizes to the UV (left) and green (right) flashes show that wild-type flies (all receptors functional) usually respond the strongest. Interestingly, Rh6-$norpA^{36}$ rescue (70% R8's functional) responds to the green flash comparable to the wild-type. **B)** ERG-response sizes to the UV (left) and green (right) flashes show that the R1-R6 functional flies (wild-type and Rh1-$norpA^{36}$ rescue) respond the strongest.

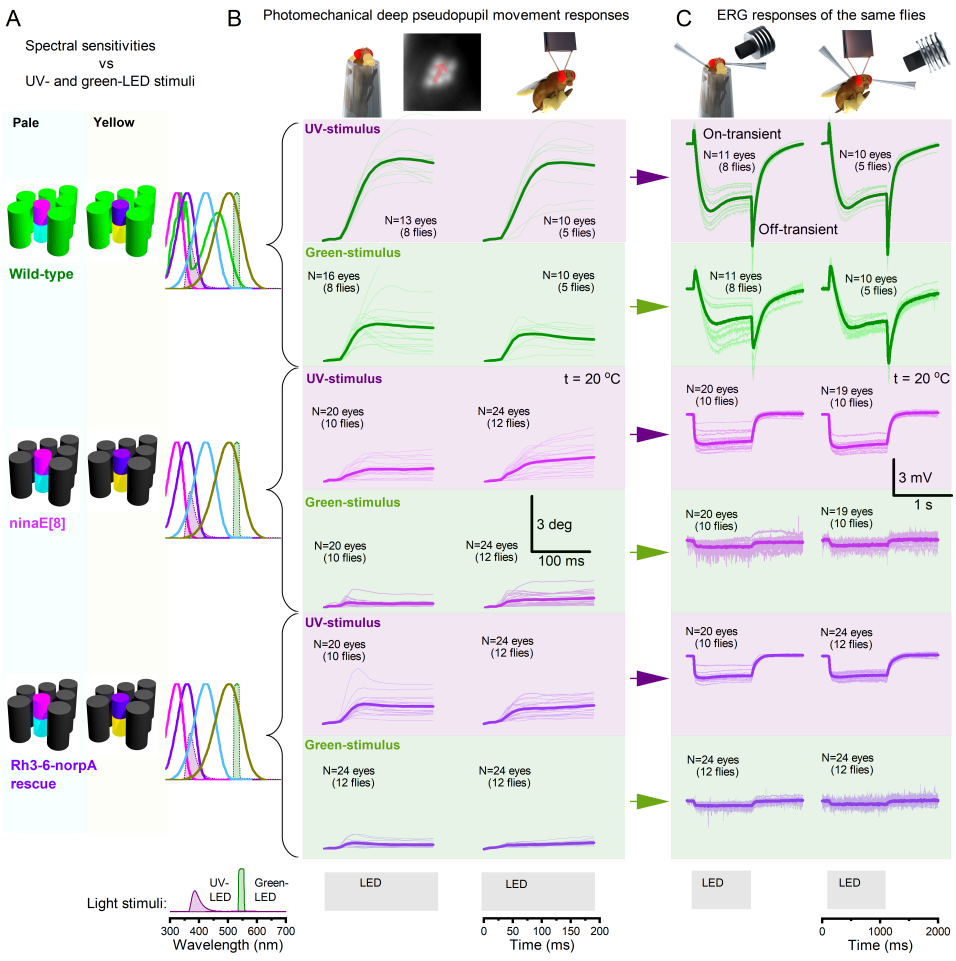

Figure 4.4: The tested preparation techniques provide similar DPP-MS- and ERG-responses. A) Spectral sensitivity profiles in the tested flies and used stimuli. **B)** DPP-microsaccades appear qualitatively similar in the pipette tip and copper-hook tethered groups. **C)** The ERG-responses appear remarkably similar in both groups.

First, in the case of the DPP-microsaccades, the pipette tip and the copper hooked flies had generally similar response shapes and sizes (**Figure 4.4B**), suggesting that the preparation techniques were interchangeable. However, the statistical analysis shows the DPP-microsaccades were significantly larger in the tethered *ninaE*^{8} flies (**Figure 4.5A**), suggesting that the R7-R8 contractions are enhanced in the tethered flies. However, this result remains inconclusive because the control Rh3-6-*norpA*^{36} rescue flies show no increased responses in the tethered conditions.

Second, the ERG-responses were nearly identical for the pipette tip and copper-hook tethering techniques (**Figure 4.5C**), and the response sizes did not statistically differ between any of the tested groups (**Figure 4.5B**). These results show that in the pipette tip and copper-hook tethered flies, the photoreceptors and the lamina interneurons are similarly activated by the flash stimuli.

Overall, these results demonstrate that the pipette tip and the copper-hook tethered flies have similar DPP-microsaccades and ERG-responses, contradicting **Hypothesis 2**. Thus, the pipette tip DPP- and ERG-recordings were probably not biased by the pipette tip's restrictive effect on the fly. Moreover, the potential head squeezing damage, which can occur when pushing a fly through the pipette tip, was not affecting my results.

4.4.3 Microsaccades can follow fast changing temporal stimuli

To test **Hypothesis 3** and investigate the effect of stimulation with sinusoidal frequency sweeps, I recorded DPP-microsaccades in light-adapted wild-type eyes to three different sinusoidal point-stimuli, having either changing or constant temporal frequency (**Figure 4.6**).

First, the DPP-MS responses to sinusoidal sweep stimulus with continuously changing temporal frequency (from 0.5 Hz to 100 Hz during 10 seconds) show that the microsaccades

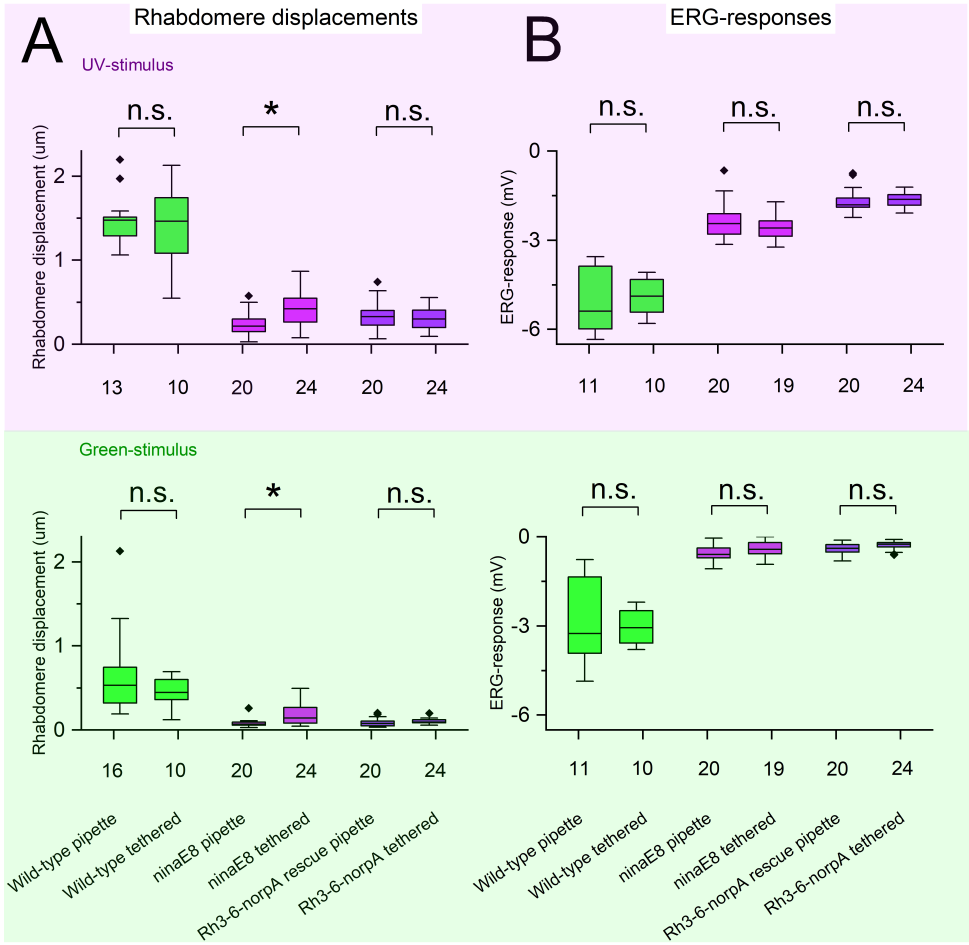

Figure 4.5: The preparation technique affects the DPP-microsaccades only in *ninaE*^{8} **A)** DPP-microsaccades in the pipette tip and copper-hook tethered flies to the UV (top), and green stimuli (bottom) show that in *ninaE*^{8} , the microsaccades were significantly larger. The numbers below the horizontal axis indicate the number of recorded eyes. From left to right, for the UV-responses p-values = 0.70,0.0032,0.63, and for the green p = 0.18, 0.0020, 0.17.
B) The ERG responses did not significantly differ between any of the tested groups. From left to right, for the UV-responses p-values = 0.70, 0.12, 0.65 and for the green p = 0.64, 0.33, 0.22.

can follow temporal changes up to 30 Hz with 13 Hz cut-off frequency (**Figure 4.6A**). Here, the DPP-microsaccades became progressively smaller as the stimulus' temporal frequency increased. The fast microsaccades appear to superimpose on a much slower DPP drift, which is nearly linear in time between 1 s and 7 s (corresponding to frequencies 1 Hz and 30 Hz). Interestingly, after the DPP-microsaccades reach their minimum gain (30 Hz), the drift reverses, and starts to move the DPP towards the recording's starting position. This is also visible in the fly specific responses (gray traces), which appear slightly more chaotic. The nature and origin of this drift is further explored in the discussion.

Second, the square wave frequency sweep shows a similar overall response shape and frequency gain as the sinusoidal sweep (**Figure 4.6B**). Here, however, the stimulus's instantaneous on- and off-edges create fast sharp-spike-like DPP movement responses, displacing the receptors further away, indicating that the sudden contrast changes cause larger receptor contractions than the gradual changes. The square sweep recordings show nearly identical DPP drifting to the sinusoidal sweep, with the reversal approximately at the DPP-microsaccades' minimum gain frequency.

Third, the 100 ms step stimulus shows how positive and negative contrast changes, respectively, lead to the fast- and slow-movement phases (**Figure 4.6C**). Here, the largest response was created by the -1 to 0 contrast steps, but also the steps from 0 to +1 and 0 to -1 led to observable microsaccades, strongly indicating the microsaccades do not require the perceptual darkness period to precede a light stimulus. With the 100 ms step stimulus, the mean step response shows no drift similar to the sweep responses. The fly specific responses (gray traces) however have seemingly random, out-of-order drifts away and towards the DPP's starting position.

These results show that the grating stimuli evoke photomechanical photoreceptor microsaccades (Hardie & Franze, 2012; Juusola et al., 2017) similar to but smaller than the flash stimulus, supporting **Hypothesis 3**. These findings mean that the photoreceptor microsaccades occur in natural light conditions and are relevant to natural vision (outside

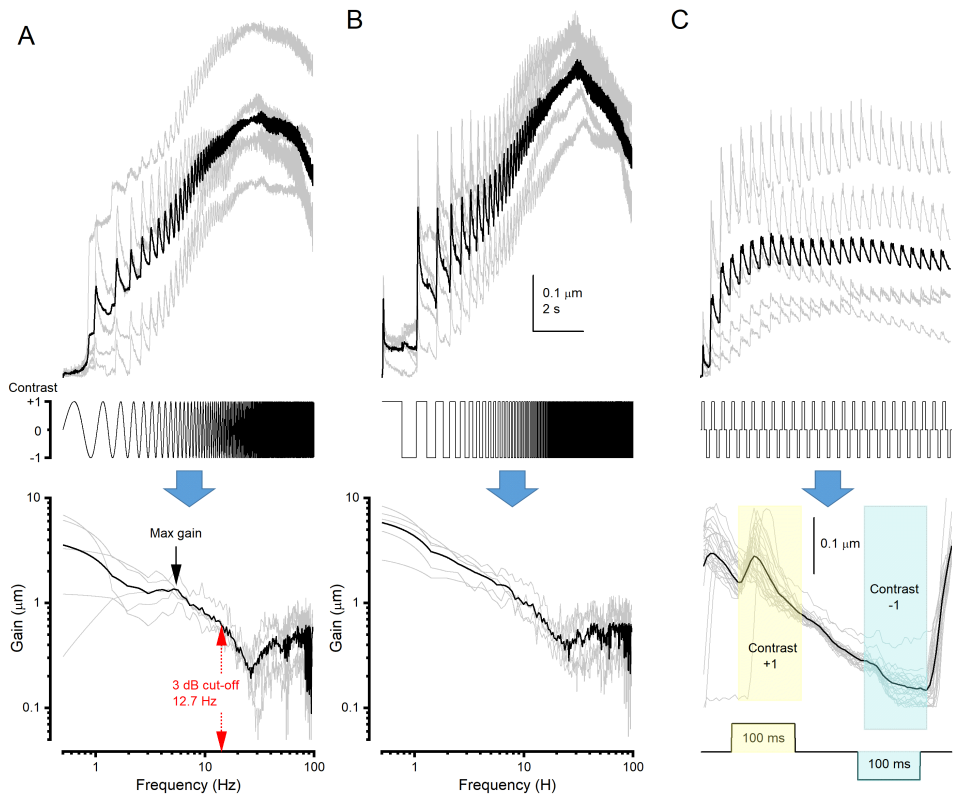

Figure 4.6: Microsaccades can follow fast changing temporal stimuli. **A)** Sinusoidal frequency sweep stimulation (middle) shows that the photoreceptor microsaccades (top) can follow frequencies up to 30 Hz with 13 Hz (3 dB) cut-off frequency based on the calculated gain function (bottom). **B)** The DPP-microsaccades caused by the square wave sweep show spike-like movement responses to positive contrast changes. **C)** The 100 ms constant-frequency step DPP-microsaccades show how the contrast increments and decrements cause the DPP-microsaccade fast- and slow-phases.

the laboratory settings).

4.5 Discussion

4.5.1 Rhabdomeres' contributions towards the microsaccades

The experiments with wild-type and rhodopsin-specific blind fly rescues showed that all the tested R1-R8 configurations (all R1-R8 functional; only R1-R6 functional; only R7-R8 functional; only R7 subset functional; only R8 subset functional) led to considerable-sized photoreceptor microsaccades. These results revealled that all rhabdomeres contribute towards the microsaccades. However, in the Rh4-$norpA^{36}$ rescue (with only $R7_{yellow}$ functional), the responses to UV were smaller than expected (based on the R7yellow numbers and spectral sensitivity). One possible explanation is the flies' carotenoid deprived diet (Table 2.1). The Rh4 alone is mostly blue sensitive (430 nm) but its sensitivity in the $R7_{yellow}$ rhabdomere sensitivity is shaped by an UV-sensitizing pigment and a blue-absorbing carotenoid screening pigment (Hardie, 1985). However, the flies' showed reasonable sized (1 mV) ERG-responses to UV light, suggesting they were activated by the UV light. Another explanation may be that the Rh4-$norpA^{36}$ rescue flies could have unknown differences in their physiology or anatomy (for example, changed mechanical properties in retinal tissue). These question were not explored in this study but can be addressed in future research.

Although rhabdomeres vary in size, the outer R1-R6 have 1.0 µm average radius whereas the inner R7-R8 have 0.5 µm (Juusola et al., 2017). In addition, the R1-R6 receptors outnumber the R7-R8 in a 3-to-1 ratio. These facts support my finding that the R1-R6 contribute more towards the microsaccades (**Figure 4.2**). Still, conversely, because of the rhodopsins' spectral sensitivity functions and the $R8_{yellow}$ being screened by the $R7_{yellow}$ (Hardie, 1985), the green

stimulus evoked larger DPP-microsaccades in Rh6-*norpA*^{36} rescue flies with functional R8 subset than in the R1-R6 functional Rh1-*norpA*^{36} rescue flies (**Figure 4.2**). Therefore, to unambiguously quantify the receptor's contributions in the microsaccades, it is better to measure DPP-microsaccades' spectral sensitivity over the entire visible spectrum. And, to account for possible nonlinearities between the receptors' activation and microsaccades, these should be measured over several orders of light intensity.

Finally, I showed that all rhabdomeres inside an ommatidium move as a unit, even when activating only a subset of the receptors. This finding is interesting as the amount of optical crosstalk between the rhabdomeres should depend on the relative distances of the rhabdomeres (Wijngaard & Stavenga, 1975). However, I did not test the contribution of individual R1-R6 receptors (for example, R2 or R4 alone). In the neural superposition eye, this could be tested by stimulating the selected rhabdomeres using a specialised telescope system (Franceschini, 1975).

4.5.2 Microsaccades in immobilised flies

My DPP- and ERG-recordings using the wild-type and the R1-R6 unfunctional flies (*ninaE*^{8} and Rh3-6-*norpA*^{36} rescue) showed that the pipette tip and the copper-hook immobilisation techniques were generally interchangeable (**Figure 4.4**). This result indicates that the DPP-microsaccades in the pipette tip prepared flies were not biased, for example, by the pipette's restrictive effect on the fly. However, the copper-hooked flies had their legs waxed to avoid camera interference, and the results could have been different if the legs were mobile. Similarly, it cannot be ruled out that the DPP-microsaccades can be different in freely behaving flies. In the future, the GHS-DPP recordings could be combined with flight simulator experiments (Juusola et al., 2017; Kemppainen, Scales, et al., 2021) to test if the visual stimulus in behaving flies somehow reshapes the microsaccades.

4.5.3 Microsaccades' temporal characteristics

The sinusoidal stimuli experiments showed that the microsaccades could follow relatively high-frequency temporal stimuli even when the receptors were light-adapted (**Figure 4.6**). Thus, the cut-off frequency limit of the microsaccades is likely governed by the phototransduction kinematics and its PIP_2 cleaving cycle (Hardie & Franze, 2012) or by the retina tissue's mechanical properties.

In the frequency sweep responses (**Figure 4.6A and B**), the DPP-microsaccades appeared to superimpose on a slower drift of the DPP (creep-up and creep-down behaviours). This drift moved the DPP almost linearly (in time) away from the DPP's starting position as the stimulus frequency increased, until the DPP-microsaccades' minimum gain (30 Hz) was reached, after which the DPP started to drift towards the DPP's starting position. As the recording time period (10 s) is much longer than in the flash experiments (200 ms), the eye muscle evoked retinal shift seems reasonable candidate in addition to the photomechanical photoreceptor contractions. The eye muscle evoked saccades are modulated by light (Burtt & Patterson, 1970), and their tension may follow the change in frequency (reflexive or voluntary in origin) However, because the drifts occur in-sync in all of the recordings, the drift is unlikely caused by spontaneous eye muscle activity. The response shape overall can be quite well modelled using the four parameter photoreceptor model (Song et al., 2012) and spring-dampener system (Kemppainen, Scales, et al., 2021). The model reproduces the drift, although not perfectly, suggesting that the drift originates from the photoreceptors. Further experiments with changes stimulus length and waveform can be used to explore this DPP drift further.

The sinusoidal stimulation results indicate that the photoreceptor microsaccades occur both in laboratory settings (to flash stimuli) and in natural conditions. However, although natural scenes are mathematically composed of simple sinusoidal gratings (**Equation 1.1**), this does not mean that characterising DPP-microsaccades to all simple sinusoidal gratings

could predict the responses in natural scenes. For example, it has been demonstrated that using the Gaussian white noise stimulus underestimates the photoreceptors' information transfer rates because the receptors' refractory photon sampling tunes differently to different stimuli (input statistics) (Juusola et al., 2017). Therefore, to better investigate the microsaccades' role in the wild, future studies could use more naturalistic stimuli and take the above-discussed immobilisation method into account.

5 General discussion

The photomechanical photoreceptor contractions are a recently found phenomenon (Hardie & Franze, 2012). *In vivo*, they move the receptors with respect to the lenses (sideways and axially), enhancing the fly's vision beyond the stationary limits set by the interommatidial angle (Juusola et al., 2017). These movements were recorded using i) atomic-force microscopy on excised retinae, ii) high-speed optical imaging on dissociated cells and iii) cornea neutralisation *in vivo* (Hardie & Franze, 2012; Juusola et al., 2017). In a nutshell, this was the overall knowledge about the photoreceptor microsaccades when my investigation started.

In my thesis, I used high-speed synchrotron X-ray phase-contrast and goniometric high-speed deep pseudopupil (GHS-DPP) imaging techniques to study photomechanical photoreceptor contractions in live fruit flies (*Drosophila*). While the X-ray phase-contrast and the deep pseudopupil microscopy techniques are not new, they had not been previously used to study the photoreceptor contractions. Our X-ray phase-contrast imaging experiments let us see inside the fly head, showing how the contractions moved the receptors (back-to-front) along their side profile. On the other hand, my GHS-DPP microscopy experiments revealed the magnified rhabdomere tips (DPP) head-on, showing how the receptor contractions displaced the tips across the left and right eyes. With these techniques, I characterised the photoreceptor microsaccades, for the first time, in 3-dimensions.

This study produced important new knowledge about the photoreceptor microsaccades. My results showed that the microsaccades are mirror-symmetric and well organised across the eyes, suggesting that the microsaccades evolved to serve the fly's behavioural needs (optic

flow, stereo vision) as guided by developmentally set rhabdomere orientations. All R1-R8 rhabdomeres contribute towards the microsaccades, moving as a unit even when only a subset of them are light-activated. Furthermore, the microsaccades can follow frequencies up to 30 Hz, reacting to contrast changes well within 30 ms. These results support the idea (Juusola et al., 2017) that the photoreceptor microsaccades are behaviourally important and improve survival in nature. In addition, outside this thesis, both behavioural and theoretical assays provided strong evidence that *Drosophila* see the world in stereo (Kemppainen, Scales, et al., 2021). Theoretically, neural depth perception could be achieved by cross-correlating phasic disparity signals created by the mirror-symmetric photoreceptor microsaccades of the two eyes (Kemppainen, Scales, et al., 2021). This *dynamic* stereo vision algorithm enables depth perception for eyes with only few (>=3) photoreceptors having binocularly overlapping receptive fields.

By self-adjusting their receptive fields (relative to the outside world), photoreceptor microsaccades provide (muscles-less) active vision in the *Drosophila* compound eyes. I was surprised by how repeatable and robust the microsaccades were. They did, however, vary considerably from flash to flash and between flies. The flash-to-flash variation can be caused by the synaptic (lamina interneuron) or eye muscle-induced modulation, whilst the animal-to-animal variation may reflect preparation damage or eye size differences. Since the microsaccades are caused by the PIP_2 cleavage in phototransduction (Hardie & Franze, 2012), the brain can likely learn to predict the receptors' receptive fields. If the modulation is also predictable, the flash-to-flash variation may be useful for the fly, leading to slightly varied scans each time, which combat spatiotemporal aliasing.

The microsaccades were quantified precisely: we had a sub-degree resolution in rotation, stimulus trigger accuracy likely around microseconds, and notably, 100 Hz temporal imaging resolution and 1 μm (DPP) or 100 nm (X-rays) spatial resolution. Together with fly genetics, the experiments built a solid base for future studies.

Retinal micromovements of eye muscle origin were not directly observed in this study likely

because of the time scale differences (the recordings were 200 ms or 300 ms long, with the exception of the 10 s sinusoidal stimuli). Hence, the eye muscle activity manifested itself indirectly, as a shift of the DPP that occurred during the 10 s inter-stimulus-interval (ISI). In the local DPP recordings, this shift meant that the DPP's starting location in all of the tested fly strains (including the blind flies) was seemingly and randomly offset at the beginning of each repeat. However, because it was the photoreceptor microsaccades that were investigated here, the DPP's starting position at each repeat's beginning was defined as zero. How the eye muscle saccades interplay with the photoreceptor microsaccades (and *vice versa*), is an interesting topic for future studies.

Many interesting aspects of the photoreceptor microsaccades are still to be investigated. For example, because the microvillar membrane has dichroic properties (Hardie, 1985), the light polarisation state may affect the microsaccades. Similarly, the light wavelength and its distribution in natural scenes may play a role in how the microsaccades are tuned to the fly's behavioural needs. As discussed in chapter 3, the gravitation field may affect the microsaccades, either directly by exerting forces on the photoreceptors or indirectly by modulating the eye muscle's tension for example.

Based on the contrast change (Juusola et al., 2017) and frequency (**Chapter 4**), the microsaccades' sizes range from large to small. In addition, the microsaccades are localised in the vicinity of the contracting rhabdomeres (Kemppainen, Scales, et al., 2021). Therefore in natural environments, these factors likely lead to complex rhabdomere movement patterns. The receptors across the eyes move at different phases and with changing amplitudes, causing vastly parallel and complex microscanning. Comparing to the man-made microscanning devices, therefore, instead of moving the detector pixels (the sensor) as whole, for example by piezo manipulators, the photoreceptor microsaccades move individual fully pixels independently (although the adjacent and neighbouring ommatidia's movements likely correlate). On some aspects, this parallel microscanning may be superior to the synchronized microscanning techniques performed by the eye muscles or piezo manipulators. To study and induce parallel (or natural) microsaccades, a naturalistic

rotating drum patterns can be used in conjunction for example with X-ray imaging.

Overall, this study produced important new data about the 3-dimensional microsaccades. The potential applications of this work range from man-made image sensors to stereo vision algorithms, autonomous drones, consumer electronics and improved medical implants such as bionic eyes.

References

Abou Tayoun, A. N., Li, X., Chu, B., Hardie, R. C., Juusola, M., & Dolph, P. J. (2011). The drosophila sk channel (dsk) contributes to photoreceptor performance by mediating sensitivity control at the first visual network. *Journal of Neuroscience*, *31*(39), 13897–13910.

Agi, E., Langen, M., Altschuler, S. J., Wu, L. F., Zimmermann, T., & Hiesinger, P. R. (2014). The evolution and development of neural superposition. *Journal of neurogenetics*, *28*(3-4), 216–232.

Als-Nielsen, J., & McMorrow, D. (2011). *Elements of modern x-ray physics*. John Wiley & Sons.

Arias, M. M., Douglass, J. K., Wehling, M. F., & Stavenga, D. G. (2021). Automated charting of the visual space of insect compound eyes. *arXiv preprint arXiv:2106.05077*.

Baruchel, J., Bleuet, P., Bravin, A., Coan, P., Lima, E., Madsen, A., Ludwig, W., Pernot, P., & Susini, J. (2008). Advances in synchrotron hard x-ray based imaging. *Comptes Rendus Physique*, *9*(5-6), 624–641.

Beersma, D., Stavenga, D., & Kuiper, J. (1977). Retinal lattice, visual field and binocularities in flies. *Journal of comparative physiology*, *119*(3), 207–220.

Belusic, G. (2011). Erg in drosophila. *Electroretinograms*. IntechOpen.

Betz, O., Rack, A., Schmitt, C., Ershov, A., Dieterich, A., Körner, L., Haas, D., & Baumbach, T. (2008). High-speed x-ray cineradiography for analyzing complex kinematics in living insects.

Borst, A. (2009). Drosophila's view on insect vision. *Current biology*, *19*(1), R36–R47.

Bradski, G., & Kaehler, A. (2000). Opencv. *Dr. Dobb's journal of software tools*, *3*.

Buchner, E., Buchner, S., Burg, M. G., Hofbauer, A., Pak, W. L., & Pollack, I. (1993). Histamine is a major mechanosensory neurotransmitter candidate in drosophila melanogaster. *Cell and tissue research*, *273*(1), 119–125.

Burtt, E., & Patterson, J. (1970). Internal muscle in the eye of an insect. *Nature*, *228*(5267), 183–184.

Catton, W. T. (1999). The effect of target orientation on the visual acuity and the spatial frequency response of the locust eye. *Journal of insect physiology*, *45*(2), 191–200.

Cellini, B., & Mongeau, J.-M. (2020). Active vision shapes and coordinates flight motor responses in flies. *Proceedings of the National Academy of Sciences*, *117*(37), 23085–23095.

Coombe, P. (1986). The large monopolar cells l1 and l2 are responsible for erg transients in drosophila. *Journal of Comparative Physiology A*, *159*(5), 655–665.

Cooper, G. P., & Kimeldorf, D. J. (1967). Responses of single neurons in the olfactory bulbs of rabbits, dogs, and cats to x-rays. *Experientia*, *23*(2), 137–138.

Cruz, T. L., Pérez, S. M., & Chiappe, M. E. (2021). Fast tuning of posture control by visual feedback underlies gaze stabilization in walking drosophila. *Current Biology*.

Currea, J. P., Smith, J. L., & Theobald, J. C. (2018). Small fruit flies sacrifice temporal acuity to maintain contrast sensitivity. *Vision research*, *149*, 1–8.

Cutforth, T., & Gaul, U. (1997). The genetics of visual system development in drosophila: Specification, connectivity and asymmetry. *Current opinion in neurobiology*, *7*(1), 48–54.

Dahmen, H. (1991). Eye specialisation in waterstriders: An adaptation to life in a flat world. *Journal of Comparative Physiology A*, *169*(5), 623–632.

Dau, A., Friederich, U., Dongre, S., Li, X., Bollepalli, M. K., Hardie, R. C., & Juusola, M. (2016). Evidence for dynamic network regulation of drosophila photoreceptor function from mutants lacking the neurotransmitter histamine. *Frontiers in neural circuits*, *10*, 19.

Delgado, R., Delgado, M. G., Bastin-Héline, L., Glavic, A., O'Day, P. M., & Bacigalupo, J. (2019). Light-induced opening of the trp channel in isolated membrane patches excised

from photosensitive microvilli from drosophila photoreceptors. *Neuroscience*, *396*, 66–72.

Douglass, J. K., & Wehling, M. F. (2016). Rapid mapping of compound eye visual sampling parameters with facets, a highly automated wide-field goniometer. *Journal of Comparative Physiology A*, *202*(12), 839–851.

Duffin, J., & Hayter, C. R. (2000). Baring the sole: The rise and fall of the shoe-fitting fluoroscope. *Isis*, *91*(2), 260–282.

Emery, P., So, W. V., Kaneko, M., Hall, J. C., & Rosbash, M. (1998). Cry, a drosophila clock and light-regulated cryptochrome, is a major contributor to circadian rhythm resetting and photosensitivity. *Cell*, *95*(5), 669–679.

Fortin, J., & Chevrette, P. C. (1996). Realization of a fast microscanning device for infrared focal plane arrays. *Infrared Imaging Systems: Design, Analysis, Modeling, and Testing VII*, *2743*, 185–196.

Franceschini, N. (1972). Pupil and pseudopupil in the compound eye of drosophila. *Information processing in the visual systems of anthropods* (pp. 75–82). Springer.

Franceschini, N. (1975). Sampling of the visual environment by the compound eye of the fly: Fundamentals and applications. *Photoreceptor optics*, 98–125.

Friedenberg, A. (1997). Microscan in infrared staring systems. *Optical Engineering*, *36*(6), 1745–1749.

Geurten, B. R., Jähde, P., Corthals, K., & Göpfert, M. C. (2014). Saccadic body turns in walking drosophila. *Frontiers in behavioral neuroscience*, *8*, 365.

Hardie, R. C. (1985). Functional organization of the fly retina. *Progress in sensory physiology* (pp. 1–79). Springer.

Hardie, R. C., & Franze, K. (2012). Photomechanical responses in drosophila photoreceptors. *Science*, *338*(6104), 260–263.

Hardie, R. C., & Juusola, M. (2015). Phototransduction in drosophila. *Current opinion in neurobiology*, *34*, 37–45.

Hardie, R. C., & Raghu, P. (2001). Visual transduction in drosophila. *Nature*, *413*(6852), 186–193.

Hardie, R. C., Raghu, P., Moore, S., Juusola, M., Baines, R. A., & Sweeney, S. T. (2001). Calcium influx via trp channels is required to maintain pip2 levels in drosophila photoreceptors. *Neuron*, *30*(1), 149–159.

Helfrich-Förster, C., Edwards, T., Yasuyama, K., Wisotzki, B., Schneuwly, S., Stanewsky, R., Meinertzhagen, I. A., & Hofbauer, A. (2002). The extraretinal eyelet of drosophila: Development, ultrastructure, and putative circadian function. *Journal of Neuroscience*, *22*(21), 9255–9266.

Hengstenberg, R. (1972). Eye movements in the housefly musca domestica. *Information processing in the visual systems of anthropods* (pp. 93–96). Springer.

Homann, H. (1924). Zum problem der ocellenfunktion bei den insekten. *Zeitschrift für vergleichende Physiologie*, *1*(3-4), 541–578.

Horridge, G. A. (2003). Visual resolution of gratings by the compound eye of the bee apis mellifera. *Journal of experimental biology*, *206*(13), 2105–2110.

Hu, K. G., Reichert, H., & Stark, W. S. (1978). Electrophysiological characterization ofdrosophila ocelli. *Journal of comparative physiology*, *126*(1), 15–24.

Hu, K. G., & Stark, W. S. (1980). The roles of drosophila ocelli and compound eyes in phototaxis. *Journal of comparative physiology*, *135*(1), 85–95.

Huang, J., Liu, C.-H., Hughes, S. A., Postma, M., Schwiening, C. J., & Hardie, R. C. (2010). Activation of trp channels by protons and phosphoinositide depletion in drosophila photoreceptors. *Current Biology*, *20*(3), 189–197.

Huang, Y., Xie, J., & Wang, T. (2015). A fluorescence-based genetic screen to study retinal degeneration in drosophila. *PLoS One*, *10*(12), e0144925.

Hunter, J. D. (2007). Matplotlib: A 2d graphics environment. *Computing in science & engineering*, *9*(03), 90–95.

Juusola, M., Kouvalainen, E., Järvilehto, M., & Weckström, M. (1994). Contrast gain, signal-to-noise ratio, and linearity in light-adapted blowfly photoreceptors. *The Journal of general physiology*, *104*(3), 593–621.

Juusola, M., Dau, A., Song, Z., Solanki, N., Rien, D., Jaciuch, D., Dongre, S. A., Blanchard, F., de Polavieja, G. G., Hardie, R. C., et al. (2017). Microsaccadic sampling of moving image information provides drosophila hyperacute vision. *Elife*, *6*, e26117.

Juusola, M., Dau, A., Zheng, L., & Rien, D. (2016). Electrophysiological method for recording intracellular voltage responses of drosophila photoreceptors and interneurons to light stimuli in vivo. *Journal of visualized experiments: JoVE*, (112).

Juusola, M., & Hardie, R. C. (2001). Light adaptation in drosophila photoreceptors: I. response dynamics and signaling efficiency at 25 c. *The Journal of general physiology*, *117*(1), 3–25.

Kemppainen, J. (2020a). Gonio analysis. https://github.com/jkemppainen/gonio-analysis

Kemppainen, J. (2020b). Gonio imsoft. https://github.com/jkemppainen/gonio-imsoft

Kemppainen, J., Mansour, N., Takalo, J., & Juusola, M. (2021). High-speed imaging of light-induced photoreceptor microsaccades in compound eyes. *bioRxiv*.

Kemppainen, J., Scales, B., Haghighi, K. R., Takalo, J., Mansour, N., McManus, J., Leko, G., Saari, P., Hurcomb, J., Antohi, A., Suuronen, J.-P., Blanchard, F., Hardie, R. C., Song, Z., Hampton, M., Eckermann, M., Westermeier, F., Frohn, J., Hoekstra, H., … Juusola, M. (2021). Binocular mirror-symmetric microsaccadic sampling of hyperacute 3d-vision. *bioRxiv*. https://doi.org/10.1101/2021.05.03.442473

Kim, A. J., Fenk, L. M., Lyu, C., & Maimon, G. (2017). Quantitative predictions orchestrate visual signaling in drosophila. *Cell*, *168*(1-2), 280–294.

Kim, H. S., Kim, C. W., & Hong, S.-M. (2002). Compact mwir zoom camera with 20: 1 zoom range and automatic athermalization. *Optical Engineering*, *41*(7), 1661–1667.

Krapp, H. G. (2009). Ocelli. *Current Biology*, *19*(11), R435–R437.

Krapp, H. G., & Gabbiani, F. (2005). Spatial distribution of inputs and local receptive field properties of a wide-field, looming sensitive neuron. *Journal of neurophysiology*, *93*(4), 2240–2253.

Kurada, P., & O'Tousa, J. E. (1995). Retinal degeneration caused by dominant rhodopsin mutations in drosophila. *Neuron*, *14*(3), 571–579.

Land, M. F. (1997). Visual acuity in insects. *Annual review of entomology*, *42*(1), 147–177.

Langen, M., Agi, E., Altschuler, D. J., Wu, L. F., Altschuler, S. J., & Hiesinger, P. R. (2015). The developmental rules of neural superposition in drosophila. *Cell*, *162*(1), 120–133.

Leftwich, R. F. (1976). Single-detector infrared scanners. *Modern Utilization of Infrared Technology I*, *62*, 217–223.

Lengeler, B. (2001). Coherence in x-ray physics. *Naturwissenschaften*, *88*(6), 249–260.

Li, X., Abou Tayoun, A., Song, Z., Dau, A., Rien, D., Jaciuch, D., Dongre, S., Blanchard, F., Nikolaev, A., Zheng, L., et al. (2019). Ca2+-activated k+ channels reduce network excitability, improving adaptability and energetics for transmitting and perceiving sensory information. *Journal of Neuroscience*, *39*(36), 7132–7154.

Lipetz, L. E. (1955a). Electrophysiology of the x-ray phosphene. *Radiation Research*, *2*(4), 306–329.

Lipetz, L. E. (1955b). The x ray and radium phosphenes. *The British journal of ophthalmology*, *39*(10), 577.

Liu, C., & Montell, C. (2015). Forcing open trp channels: Mechanical gating as a unifying activation mechanism. *Biochemical and biophysical research communications*, *460*(1), 22–25.

Mann, K., Gallen, C. L., & Clandinin, T. R. (2017). Whole-brain calcium imaging reveals an intrinsic functional network in drosophila. *Current Biology*, *27*(15), 2389–2396.

Mishra, M., & Knust, E. (2012). Analysis of the drosophila compound eye with light and electron microscopy. *Retinal Degeneration*, 161–182.

Mokso, R., Cloetens, P., Maire, E., Ludwig, W., & Buffière, J.-Y. (2007). Nanoscale zoom tomography with hard x rays using kirkpatrick-baez optics. *Applied physics letters*, *90*(14), 144104.

Mokso, R., Schwyn, D. A., Walker, S. M., Doube, M., Wicklein, M., Müller, T., Stampanoni, M., Taylor, G. K., & Krapp, H. G. (2015). Four-dimensional in vivo x-ray microscopy with projection-guided gating. *Scientific Reports*, *5*, 8727.

Mongeau, J.-M., & Frye, M. A. (2017). Drosophila spatiotemporally integrates visual signals to control saccades. *Current Biology*, *27*(19), 2901–2914.

Montell, C. (1999). Visual transduction in drosophila. *Annual review of cell and developmental biology*, *15*(1), 231–268.

Montell, C. (2005). Trp channels in drosophila photoreceptor cells. *The Journal of physiology*, *567*(1), 45–51.

Montell, C. (2012). Drosophila visual transduction. *Trends in neurosciences*, *35*(6), 356–363.

Muijres, F. T., Elzinga, M. J., Iwasaki, N. A., & Dickinson, M. H. (2015). Body saccades of drosophila consist of stereotyped banked turns. *The Journal of experimental biology*, *218*(6), 864–875.

Nelson, M. E., & MacIver, M. A. (2006). Sensory acquisition in active sensing systems. *Journal of Comparative Physiology A*, *192*(6), 573–586.

Nériec, N., & Desplan, C. (2016). From the eye to the brain: Development of the drosophila visual system. *Current topics in developmental biology*, *116*, 247–271.

Ni, J. D., Baik, L. S., Holmes, T. C., & Montell, C. (2017). A rhodopsin in the brain functions in circadian photoentrainment in drosophila. *Nature*, *545*(7654), 340–344.

Nikolaev, A., Zheng, L., Wardill, T. J., O'Kane, C. J., De Polavieja, G. G., & Juusola, M. (2009). Network adaptation improves temporal representation of naturalistic stimuli in drosophila eye: Ii mechanisms. *PloS one*, *4*(1), e4306.

Nityananda, V., Tarawneh, G., Henriksen, S., Umeton, D., Simmons, A., & Read, J. C. (2018). A novel form of stereo vision in the praying mantis. *Current Biology*, *28*(4), 588–593.

Niven, J., Vähäsöyrinki, M., & Juusola, M. (2003). Shaker k+-channels are predicted to reduce the metabolic cost of neural information in drosophila photoreceptors. *Proceedings of the Royal Society of London. Series B: Biological Sciences*, *270*(suppl_1), S58–S61.

Osorio, D. (2007). Spam and the evolution of the fly's eye. *Bioessays*, *29*(2), 111–115.

Otero-Millan, J., Troncoso, X. G., Macknik, S. L., Serrano-Pedraza, I., & Martinez-Conde, S. (2008). Saccades and microsaccades during visual fixation, exploration, and search: Foundations for a common saccadic generator. *Journal of vision*, *8*(14), 21–21.

Petrowitz, R., Dahmen, H., Egelhaaf, M., & Krapp, H. G. (2000). Arrangement of optical axes and spatial resolution in the compound eye of the female blowfly calliphora. *Journal of Comparative Physiology A*, *186*(7-8), 737–746.

Pollack, I., & Hofbauer, A. (1991). Histamine-like immunoreactivity in the visual system and brain of drosophila melanogaster. *Cell and tissue research*, *266*(2), 391–398.

Read, J. C. (2021). Binocular vision and stereopsis across the animal kingdom. *Annual Review of Vision Science*, *7*, 389–415.

Rieger, D., Stanewsky, R., & Helfrich-Förster, C. (2003). Cryptochrome, compound eyes, hofbauer-buchner eyelets, and ocelli play different roles in the entrainment and masking pathway of the locomotor activity rhythm in the fruit fly drosophila melanogaster. *Journal of biological rhythms*, *18*(5), 377–391.

Rossel, S. (1983). Binocular stereopsis in an insect. *Nature*, *302*(5911), 821–822.

Schön, D., Xiao, J., Golnak, R., Tesch, M. F., Winter, B., Velasco-Velez, J.-J., & Aziz, E. F. (2017). Introducing ionic-current detection for x-ray absorption spectroscopy in liquid cells. *The journal of physical chemistry letters*, *8*(9), 2087–2092.

Schroeder, C. E., Wilson, D. A., Radman, T., Scharfman, H., & Lakatos, P. (2010). Dynamics of active sensing and perceptual selection. *Current opinion in neurobiology*, *20*(2), 172–176.

Seelig, J. D., Chiappe, M. E., Lott, G. K., Dutta, A., Osborne, J. E., Reiser, M. B., & Jayaraman, V. (2010). Two-photon calcium imaging from head-fixed drosophila during optomotor walking behavior. *Nature methods*, *7*(7), 535–540.

Seidl, R., & Kaiser, W. (1981). Visual field size, binocular domain and the ommatidial array of the compound eyes in worker honey bees. *Journal of comparative physiology*, *143*(1), 17–26.

Senthilan, P. R., Grebler, R., Reinhard, N., Rieger, D., & Helfrich-Förster, C. (2019). Role of rhodopsins as circadian photoreceptors in the drosophila melanogaster. *Biology*, *8*(1), 6.

Sherman-Gold, R. (1993). *The axon guide for electrophysiology & biophysics laboratory techniques* (1st ed.). Axon Instruments.

Smolka, J., & Hemmi, J. M. (2009). Topography of vision and behaviour. *Journal of Experimental Biology*, *212*(21), 3522–3532.

Socha, J. J., Förster, T. D., & Greenlee, K. J. (2010). Issues of convection in insect respiration: Insights from synchrotron x-ray imaging and beyond. *Respiratory Physiology & Neurobiology*, *173*, S65–S73.

Sokabe, T., Bradshaw, H. B., Tominaga, M., Leishman, E., & Montell, C. (2021). Light-induction of endocannabinoids and activation of drosophila trpc channels. *bioRxiv*.

Song, Z., Coca, D., Billings, S., Postma, M., Hardie, R. C., & Juusola, M. (2009). Biophysical modeling of a drosophila photoreceptor. *International Conference on Neural Information Processing*, 57–71.

Song, Z., & Juusola, M. (2014). Refractory sampling links efficiency and costs of sensory encoding to stimulus statistics. *Journal of Neuroscience*, *34*(21), 7216–7237.

Song, Z., Postma, M., Billings, S. A., Coca, D., Hardie, R. C., & Juusola, M. (2012). Stochastic, adaptive sampling of information by microvilli in fly photoreceptors. *Current Biology*, *22*(15), 1371–1380.

Song, Z., Zhou, Y., & Juusola, M. (2016). Random photon absorption model elucidates how early gain control in fly photoreceptors arises from quantal sampling. *Frontiers in computational neuroscience*, *10*, 61.

Spencer, M. (1982). *Fundamentals of light microscopy* (Vol. 6). Cambridge University Press.

Srinivasan, M., & Lehrer, M. (1988). Spatial acuity of honeybee vision and its spectral properties. *Journal of Comparative Physiology A*, *162*(2), 159–172.

Stark, W. S., Ivanyshyn, A. M., & Hu, K. G. (1976). Spectral sensitivities and photopigments in adaptation of fly visual receptors. *Naturwissenschaften*, *63*(11), 513–518.

Tepass, U., & Harris, K. P. (2007). Adherens junctions in drosophila retinal morphogenesis. *Trends in cell biology*, *17*(1), 26–35.

Veleri, S., Rieger, D., Helfrich-Förster, C., & Stanewsky, R. (2007). Hofbauer-buchner eyelet affects circadian photosensitivity and coordinates tim and per expression in drosophila clock neurons. *Journal of biological rhythms*, *22*(1), 29–42.

Viollet, S. (2014). Vibrating makes for better seeing: From the fly's micro-eye movements to hyperacute visual sensors. *Frontiers in bioengineering and biotechnology*, *2*, 9.

Wachowiak, M. (2011). All in a sniff: Olfaction as a model for active sensing. *Neuron*, *71*(6), 962–973.

Wang, T., Wang, X., Xie, Q., & Montell, C. (2008). The socs box protein stops is required for phototransduction through its effects on phospholipase c. *Neuron*, *57*(1), 56–68.

Wardill, T. J., List, O., Li, X., Dongre, S., McCulloch, M., Ting, C.-Y., O'Kane, C. J., Tang, S., Lee, C.-H., Hardie, R. C., & Juusola, M. (2012). Multiple spectral inputs improve motion discrimination in the drosophila visual system. *Science*, *336*(6083), 925–931. https://doi.org/10.1126/science.1215317

Washburn, T., & O'Tousa, J. E. (1989). Molecular defects in drosophila rhodopsin mutants. *Journal of Biological Chemistry*, *264*(26), 15464–15466.

Wehrhahn, C. (1984). Ocellar vision and orientation in flies. *Proceedings of the Royal society of London. Series B. Biological sciences*, *222*(1228), 409–411.

Wernet, M. F., Mazzoni, E. O., Celik, A., Duncan, D. M., Duncan, I., & Desplan, C. (2006). Stochastic spineless expression creates the retinal mosaic for colour vision. *Nature*, *440*(7081), 174–180.

West, R. M. (2021). Best practice in statistics: Use the welch t-test when testing the difference between two groups. *Annals of Clinical Biochemistry*, 0004563221992088.

Wijngaard, W., & Stavenga, D. (1975). On optical crosstalk between fly rhabdomeres. *Biological cybernetics*, *18*(2), 61–67.

Willmott, P. (2019). *An introduction to synchrotron radiation: Techniques and applications*. John Wiley & Sons.

Yasuyama, K., & Meinertzhagen, I. (1999). Extraretinal photoreceptors at the compound eye's posterior margin in drosophila melanogaster. *Journal of Comparative Neurology*, *412*(2), 193–202.

Zelhof, A. C., Hardy, R. W., Becker, A., & Zuker, C. S. (2006). Transforming the architecture of compound eyes. *Nature*, *443*(7112), 696–699.

Zelhof, A. C., Koundakjian, E., Scully, A. L., Hardy, R. W., & Pounds, L. (2003). Mutation of the photoreceptor specific homeodomain gene pph13 results in defects in phototransduction and rhabdomere morphogenesis.

Zheng, L., de Polavieja, G. G., Wolfram, V., Asyali, M. H., Hardie, R. C., & Juusola, M. (2006). Feedback network controls photoreceptor output at the layer of first visual synapses in drosophila. *The Journal of general physiology, 127*(5), 495–510.

Zhu, Y. (2013). The drosophila visual system: From neural circuits to behavior. *Cell adhesion & migration, 7*(4), 333–344.

Appendix 1

Statistical tests on DPP-microsaccades and ERG-responses for the fly groups tested in chapter 4 (Local DPP-microsaccade recordings, **Figure 4.3**).

Table A1. DPP-microsaccades to UV flashes

Group A	Group B	N_A	N_B	Mean difference A-B (µm)	Test	p-value (Holm-Sidak)	
wild-type	ninae8	15	20	1.294	t-test	3.764E-10	***
wild-type	Rh3-6-norpA rescue	15	20	1.21	t-test	9.261E-10	***
wild-type	Rh1-norpA rescue	15	16	1.289	Mann–Whitney	6.023E-05	***
wild-type	Rh3-norpA rescue	15	18	1.388	t-test	3.786E-10	***
wild-type	Rh4-norpA rescue	15	20	1.487	t-test	1.309E-09	***
wild-type	Rh5-norpA rescue	15	20	1.399	Mann–Whitney	1.75E-05	***
wild-type	Rh6-norpA rescue	15	18	1.401	t-test	1.575E-09	***
wild-type	norpA36-mutant	15	12	1.499	t-test	1.228E-09	***
ninae8	Rh3-6-norpA rescue	20	20	-0.08473	t-test	0.4783	ns
ninae8	Rh1-norpA rescue	20	16	-0.005689	Mann–Whitney	0.9884	ns
ninae8	Rh3-norpA rescue	20	18	0.09324	t-test	0.3837	ns
ninae8	Rh4-norpA rescue	20	20	0.1923	t-test	0.0004994	***
ninae8	Rh5-norpA rescue	20	20	0.1049	Mann–Whitney	0.1486	ns
ninae8	Rh6-norpA rescue	20	18	0.1064	t-test	0.1134	ns
ninae8	norpA36-mutant	20	12	0.2044	t-test	0.0002845	***
Rh3-6-norpA rescue	Rh1-norpA rescue	20	16	0.07904	Mann–Whitney	0.4028	ns
Rh3-6-norpA rescue	Rh3-norpA rescue	20	18	0.178	t-test	0.006958	**
Rh3-6-norpA rescue	Rh4-norpA rescue	20	20	0.2771	t-test	1.027E-05	***
Rh3-6-norpA rescue	Rh5-norpA rescue	20	20	0.1896	Mann–Whitney	0.0003795	***
Rh3-6-norpA rescue	Rh6-norpA rescue	20	18	0.1911	t-test	0.0009398	***
Rh3-6-norpA rescue	norpA36-mutant	20	12	0.2892	t-test	5.726E-06	***
Rh1-norpA rescue	Rh3-norpA rescue	16	18	0.09893	Mann–Whitney	0.4783	ns
Rh1-norpA rescue	Rh4-norpA rescue	16	20	0.198	Mann–Whitney	0.0001661	***
Rh1-norpA rescue	Rh5-norpA rescue	16	20	0.1106	Mann–Whitney	0.4028	ns
Rh1-norpA rescue	Rh6-norpA rescue	16	18	0.1121	Mann–Whitney	0.4028	ns
Rh1-norpA rescue	norpA36-mutant	16	12	0.2101	Mann–Whitney	0.0003125	***
Rh3-norpA rescue	Rh4-norpA rescue	18	20	0.09909	t-test	0.0298	*
Rh3-norpA rescue	Rh5-norpA rescue	18	20	0.01162	Mann–Whitney	0.9884	ns

Rh3-norpA rescue	Rh6-norpA rescue	18	18	0.01313	t-test	0.9884	ns
Rh3-norpA rescue	norpA36-mutant	18	12	0.1112	t-test	0.01212	*
Rh4-norpA rescue	Rh5-norpA rescue	20	20	-0.08746	Mann–Whitney	0.0004081	***
Rh4-norpA rescue	Rh6-norpA rescue	20	18	-0.08596	t-test	0.0002015	***
Rh4-norpA rescue	norpA36-mutant	20	12	0.0121	t-test	0.4028	ns
Rh5-norpA rescue	Rh6-norpA rescue	20	18	0.001505	Mann–Whitney	0.9884	ns
Rh5-norpA rescue	norpA36-mutant	20	12	0.09956	Mann–Whitney	0.0007226	***
Rh6-norpA rescue	norpA36-mutant	18	12	0.09805	t-test	3.932E-05	***

Table A2. DPP-microsaccades to green flashes

Group A	Group B	N_A	N_B	Mean difference A-B (µm)	Test	p-value (Holm-Sidak)	
wild-type	ninae8	16	20	0.5928	Mann–Whitney	1.354E-05	***
wild-type	Rh3-6-norpA rescue	16	20	0.5882	Mann–Whitney	1.354E-05	***
wild-type	Rh1-norpA rescue	16	16	0.3935	Mann–Whitney	0.03048	*
wild-type	Rh3-norpA rescue	16	18	0.6311	Mann–Whitney	1.991E-05	***
wild-type	Rh4-norpA rescue	16	20	0.6381	Mann–Whitney	1.259E-05	***
wild-type	Rh5-norpA rescue	16	20	0.6325	Mann–Whitney	1.259E-05	***
wild-type	Rh6-norpA rescue	16	18	0.2634	Mann–Whitney	0.5502	ns
wild-type	norpA36-mutant	16	12	0.642	Mann–Whitney	0.000204	***
ninae8	Rh3-6-norpA rescue	20	20	-0.004586	Mann–Whitney	0.9669	ns
ninae8	Rh1-norpA rescue	20	16	-0.1994	Mann–Whitney	0.001349	**
ninae8	Rh3-norpA rescue	20	18	0.03828	Mann–Whitney	0.002407	**
ninae8	Rh4-norpA rescue	20	20	0.04527	Mann–Whitney	8.748E-05	***
ninae8	Rh5-norpA rescue	20	20	0.03965	Mann–Whitney	0.001002	**
ninae8	Rh6-norpA rescue	20	18	-0.3295	Mann–Whitney	1.145E-05	***
ninae8	norpA36-mutant	20	12	0.04913	Mann–Whitney	0.0004572	***
Rh3-6-norpA rescue	Rh1-norpA rescue	20	16	-0.1948	Mann–Whitney	0.004619	**
Rh3-6-norpA rescue	Rh3-norpA rescue	20	18	0.04287	Mann–Whitney	0.008935	**
Rh3-6-norpA rescue	Rh4-norpA rescue	20	20	0.04986	Mann–Whitney	0.0002501	***
Rh3-6-norpA rescue	Rh5-norpA rescue	20	20	0.04424	Mann–Whitney	0.003563	**
Rh3-6-norpA rescue	Rh6-norpA rescue	20	18	-0.3249	Mann–Whitney	1.494E-05	***
Rh3-6-norpA rescue	norpA36-mutant	20	12	0.05371	t-test	0.001349	**
Rh1-norpA rescue	Rh3-norpA rescue	16	18	0.2377	Mann–Whitney	0.0002282	***
Rh1-norpA rescue	Rh4-norpA rescue	16	20	0.2446	Mann–Whitney	8.065E-05	***
Rh1-norpA rescue	Rh5-norpA rescue	16	20	0.239	Mann–Whitney	0.0001179	***
Rh1-norpA rescue	Rh6-norpA rescue	16	18	-0.1301	Mann–Whitney	0.3667	ns

Rh1-norpA rescue	norpA36-mutant	16	12	0.2485	Mann–Whitney	0.0005855	***
Rh3-norpA rescue	Rh4-norpA rescue	18	20	0.006993	Mann–Whitney	0.5723	ns
Rh3-norpA rescue	Rh5-norpA rescue	18	20	0.001372	Mann–Whitney	0.9669	ns
Rh3-norpA rescue	Rh6-norpA rescue	18	18	-0.3677	Mann–Whitney	1.259E-05	***
Rh3-norpA rescue	norpA36-mutant	18	12	0.01085	Mann–Whitney	0.3638	ns
Rh4-norpA rescue	Rh5-norpA rescue	20	20	-0.005622	Mann–Whitney	0.6268	ns
Rh4-norpA rescue	Rh6-norpA rescue	20	18	-0.3747	Mann–Whitney	5.543E-06	***
Rh4-norpA rescue	norpA36-mutant	20	12	0.003853	Mann–Whitney	0.7128	ns
Rh5-norpA rescue	Rh6-norpA rescue	20	18	-0.3691	Mann–Whitney	5.543E-06	***
Rh5-norpA rescue	norpA36-mutant	20	12	0.009475	Mann–Whitney	0.3667	ns
Rh6-norpA rescue	norpA36-mutant	18	12	0.3786	Mann–Whitney	0.0001229	***

Table A3. ERG-responses to UV flashes

Group A	**Group B**	**N_A**	**N_B**	**Mean difference A-B (mV)**	**Test**	**p-value (Holm-Sidak)**	
wild-type	ninae8	11	20	-2.686	Mann–Whitney	0.0001601	***
wild-type	Rh3-6-norpA rescue	11	20	-3.336	Mann–Whitney	0.0001601	***
wild-type	Rh1-norpA rescue	11	8	-0.9439	t-test	0.1398	ns
wild-type	Rh3-norpA rescue	11	9	-3.975	t-test	1.455E-06	***
wild-type	Rh4-norpA rescue	11	10	-4.46	t-test	5.802E-07	***
wild-type	Rh5-norpA rescue	11	10	-4.759	t-test	7.155E-07	***
wild-type	Rh6-norpA rescue	11	7	-4.711	Mann–Whitney	0.000771	***
wild-type	norpA36-mutant	11	12	-5.037	t-test	5.408E-07	***
ninae8	Rh3-6-norpA rescue	20	20	-0.6499	Mann–Whitney	0.001624	**
ninae8	Rh1-norpA rescue	20	8	1.742	Mann–Whitney	0.001785	**
ninae8	Rh3-norpA rescue	20	9	-1.289	Mann–Whitney	0.001624	**
ninae8	Rh4-norpA rescue	20	10	-1.775	Mann–Whitney	0.0006235	***
ninae8	Rh5-norpA rescue	20	10	-2.073	Mann–Whitney	0.0002762	***
ninae8	Rh6-norpA rescue	20	7	-2.026	Mann–Whitney	6.982E-05	***
ninae8	norpA36-mutant	20	12	-2.351	Mann–Whitney	9.225E-05	***
Rh3-6-norpA rescue	Rh1-norpA rescue	20	8	2.392	Mann–Whitney	2.059E-05	***
Rh3-6-norpA rescue	Rh3-norpA rescue	20	9	-0.6389	Mann–Whitney	0.005324	**
Rh3-6-norpA rescue	Rh4-norpA rescue	20	10	-1.125	Mann–Whitney	0.000547	***
Rh3-6-norpA rescue	Rh5-norpA rescue	20	10	-1.423	Mann–Whitney	0.0002762	***
Rh3-6-norpA rescue	Rh6-norpA rescue	20	7	-1.376	Mann–Whitney	6.982E-05	***
Rh3-6-norpA rescue	norpA36-mutant	20	12	-1.701	Mann–Whitney	9.225E-05	***
Rh1-norpA rescue	Rh3-norpA rescue	8	9	-3.031	t-test	0.000771	***

Rh1-norpA rescue	Rh4-norpA rescue	8	10	-3.516	t-test	0.0004151	***
Rh1-norpA rescue	Rh5-norpA rescue	8	10	-3.815	t-test	0.0003505	***
Rh1-norpA rescue	Rh6-norpA rescue	8	7	-3.767	Mann–Whitney	0.002174	**
Rh1-norpA rescue	norpA36-mutant	8	12	-4.093	t-test	0.0002762	***
Rh3-norpA rescue	Rh4-norpA rescue	9	10	-0.4857	t-test	0.005559	**
Rh3-norpA rescue	Rh5-norpA rescue	9	10	-0.7842	t-test	0.0002578	***
Rh3-norpA rescue	Rh6-norpA rescue	9	7	-0.7367	Mann–Whitney	0.001624	**
Rh3-norpA rescue	norpA36-mutant	9	12	-1.062	t-test	6.982E-05	***
Rh4-norpA rescue	Rh5-norpA rescue	10	10	-0.2985	t-test	0.02117	*
Rh4-norpA rescue	Rh6-norpA rescue	10	7	-0.251	Mann–Whitney	0.1238	ns
Rh4-norpA rescue	norpA36-mutant	10	12	-0.5763	t-test	0.0006559	***
Rh5-norpA rescue	Rh6-norpA rescue	10	7	0.04752	Mann–Whitney	0.3148	ns
Rh5-norpA rescue	norpA36-mutant	10	12	-0.2778	t-test	0.0002762	***
Rh6-norpA rescue	norpA36-mutant	7	12	-0.3253	Mann–Whitney	0.0006235	***

Table A4. ERG-responses to green flashes

Group A	Group B	N_A	N_B	Mean difference A-B (mV)	Test	p-value (Holm-Sidak)	
wild-type	ninae8	11	20	-2.16	t-test	0.007562	**
wild-type	Rh3-6-norpA rescue	11	20	-2.319	t-test	0.004903	**
wild-type	Rh1-norpA rescue	11	8	0.2824	t-test	0.9383	ns
wild-type	Rh3-norpA rescue	11	9	-2.698	t-test	0.002055	**
wild-type	Rh4-norpA rescue	11	10	-2.729	t-test	0.002055	**
wild-type	Rh5-norpA rescue	11	10	-2.692	t-test	0.002055	**
wild-type	Rh6-norpA rescue	11	7	-2.445	Mann–Whitney	0.001319	**
wild-type	norpA36-mutant	11	12	-2.727	t-test	0.002055	**
ninae8	Rh3-6-norpA rescue	20	20	-0.1591	t-test	0.2628	ns
ninae8	Rh1-norpA rescue	20	8	2.443	t-test	0.001316	**
ninae8	Rh3-norpA rescue	20	9	-0.5377	t-test	3.218E-07	***
ninae8	Rh4-norpA rescue	20	10	-0.5689	t-test	1.329E-07	***
ninae8	Rh5-norpA rescue	20	10	-0.5312	t-test	3.71E-07	***
ninae8	Rh6-norpA rescue	20	7	-0.2845	Mann–Whitney	0.1267	ns
ninae8	norpA36-mutant	20	12	-0.5672	t-test	1.598E-07	***
Rh3-6-norpA rescue	Rh1-norpA rescue	20	8	2.602	t-test	0.001038	**
Rh3-6-norpA rescue	Rh3-norpA rescue	20	9	-0.3786	t-test	8.788E-07	***
Rh3-6-norpA rescue	Rh4-norpA rescue	20	10	-0.4098	t-test	5.566E-07	***
Rh3-6-norpA rescue	Rh5-norpA rescue	20	10	-0.3721	t-test	1.172E-06	***
Rh3-6-norpA rescue	Rh6-norpA rescue	20	7	-0.1253	Mann–Whitney	0.7945	ns

Rh3-6-norpA rescue	norpA36-mutant	20	12	-0.4081	t-test	9.72E-08	***
Rh1-norpA rescue	Rh3-norpA rescue	8	9	-2.98	t-test	0.0005387	***
Rh1-norpA rescue	Rh4-norpA rescue	8	10	-3.012	t-test	0.000509	***
Rh1-norpA rescue	Rh5-norpA rescue	8	10	-2.974	t-test	0.0005387	***
Rh1-norpA rescue	Rh6-norpA rescue	8	7	-2.727	Mann–Whitney	0.004342	**
Rh1-norpA rescue	norpA36-mutant	8	12	-3.01	t-test	0.0005387	***
Rh3-norpA rescue	Rh4-norpA rescue	9	10	-0.03122	t-test	0.9248	ns
Rh3-norpA rescue	Rh5-norpA rescue	9	10	0.006476	t-test	0.9824	ns
Rh3-norpA rescue	Rh6-norpA rescue	9	7	0.2532	Mann–Whitney	0.002619	**
Rh3-norpA rescue	norpA36-mutant	9	12	-0.0295	t-test	0.9248	ns
Rh4-norpA rescue	Rh5-norpA rescue	10	10	0.03769	t-test	0.9248	ns
Rh4-norpA rescue	Rh6-norpA rescue	10	7	0.2844	Mann–Whitney	0.002055	**
Rh4-norpA rescue	norpA36-mutant	10	12	0.001719	t-test	0.9824	ns
Rh5-norpA rescue	Rh6-norpA rescue	10	7	0.2467	Mann–Whitney	0.00789	**
Rh5-norpA rescue	norpA36-mutant	10	12	-0.03597	t-test	0.8906	ns
Rh6-norpA rescue	norpA36-mutant	7	12	-0.2827	Mann–Whitney	0.0009522	***